Few-Body Systems in Lattice Effective Field Theory

Dissertation
zur
Erlangung des Doktorgrades (Dr. rer. nat.)
der
Mathematisch-Naturwissenschaftlichen Fakultät
der
Rheinischen Friedrich-Wilhelms-Universität Bonn

von
Nico Klein
aus
Frankenthal (Pfalz)

Bonn, November 2018

Dieser Forschungsbericht wurde als Dissertation von der Mathematisch-Naturwissenschaftlichen Fakultät der Universität Bonn angenommen und ist auf dem Hochschulschriftenserver der ULB Bonn http://hss.ulb.uni-bonn.de/diss_online elektronisch publiziert.

1. Gutachter:	Prof. Dr. Ulf-G. Meißner
2. Gutachter:	Prof. Dr. Thomas Luu
Tag der Promotion:	11.01.2019
Erscheinungsjahr:	2019

Abstract

Nuclear lattice effective field theory is a novel approach in nuclear physics combining classical effective field theory with lattice methods and newly available computational resources. It is particularly successful for few- and many-body systems, where one calculates ground state and scattering state properties using *ab initio* techniques. Thanks to the discretization of space and time, one can use Monte Carlo methods to evaluate physical observables and additionally, one may use discretization improvement programs as well for the reduction of lattice spacing artifacts. In contrast to lattice quantum chromodynamics, the lattice spacing does have a physical meaning, namely the cutoff which is inherent to any effective theory. Hence, it is necessary to understand the discretization effects. Such a study has been a missing part of nuclear lattice effective field theory as most calculations have been performed at a fixed lattice spacing of $a = 1.97$ fm. I will have a thorough look at it and examine the problem from different perspectives in the following. Due to computational limitations we restrict ourselves to few-body systems, where we have a lot of data from Nijmegen partial wave analysis for nucleon-nucleon scattering, very precise knowledge on the bound state of triton and helium-4 and also various correlation theorems. The Tjon line is such a correlation theorem between triton and helium-4 binding energies which states that the two-nucleon interaction results in a correlated prediction of triton and helium binding energies while a three-nucleon interaction that fixes the triton binding energy automatically reproduces the right helium-4 binding energy.

The first project looks at the deuteron binding energy and low-energy scattering observables, namely the S wave scattering length and effective range in dependence on the lattice spacing for various regularization schemes. We employ lattice spacings up to $a = 0.5$ fm and we show that the neutron-proton system with and without pion exchange becomes stable if the regularization scheme is chosen rightly and the lattice spacing is small enough.

Secondly, I perform an analysis of $2N$, $3N$ and $4N$ systems for three different lattice spacings at leading, next-to-leading and next-to-next-to-leading order. I show that the continuum correlation between $3N$ and $4N$ systems is reproduced once the lattice spacing is chosen fine enough.

Lastly, I examine the few-body boson system in one dimension. Such a system does have an exact solution and hence, lattice artifacts can be observed in a very transparent way. I show that we can absorb lattice spacing artifacts systematically by adding additional operators due to a consistent power counting scheme. Finally, we can do robust continuum extrapolations. We examine systems up to and including five bosons and the remaining errors scale linearly, as the third and fourth power of the lattice spacing at leading, next-to-leading and next-to-next-to-leading order.

During the time of my thesis, the following articles have been published:

1. N. Klein, D. Lee, W. Liu and U.-G. Meißner, "Regularization Methods for Nuclear Lattice Effective Field Theory," Phys. Lett. B **747** (2015) 511.

2. S. Elhatisari, N. Li, A. Rokash, J. M. Alarcón, D. Du, N. Klein, B.-N. Lu, U.-G. Meißner, E. Epelbaum, H. Krebs, T. A. Lähde, D. Lee and G. Rupak, "Nuclear binding near a quantum phase transition," Phys. Rev. Lett. **1**17 (2016) no.13, 132501.

3. J. M. Alarcón, D. Du, N. Klein, T. A. Lähde, D. Lee, N. Li, B.-N. Lu, T. Luu and U.-G. Meißner, "Neutron-proton scattering at next-to-next-to-leading order in Nuclear Lattice Effective Field Theory," Eur. Phys. J. A **53** (2017) no.5, 83.

4. N. Klein, S. Elhatisari, T. A. Lähde, D. Lee and U.-G. Meißner, "The Tjon Band in Nuclear Lattice Effective Field Theory," Eur. Phys. J. A **54** (2018) no.7, 121.

5. N. Klein, D. Lee and U.-G. Meißner, "Lattice Improvement in Lattice Effective Field Theory," arXiv:1807.04234 [hep-lat].

Article 1, 4 and 5 are the basis for this thesis.

Contents

CHAPTER 1

Introduction and Motivation

1.1 The standard model of particle physics and quantum chromodynamics

The standard model of particle physics consists of the fundamental particles and the fundamental forces. The particles are quarks on the one hand and leptons on the other hand. The quarks consist of (u)p, (d)own, (s)trange, (c)harm, (b)ottom and (t)op quarks and they interact via gluons. Besides, the leptons consist of electron, muon and tau as well as electron neutrino, muon neutrino and tau neutrino. Leptons and quarks interact via the photon (electromagnetic force), the $W^{\pm}$-, Z-boson (weak force), or the Higgs boson. From a gauge theory perspective, the standard model can be described as a

$$\mathrm{SU}(3)_C \times \mathrm{SU}(2)_L \times \mathrm{U}(1)_Y \tag{1.1}$$

gauge theory, where $\mathrm{SU}(3)_C$ is the color gauge invariance in the strong sector, and $\mathrm{SU}(2)_L \times \mathrm{U}(1)_Y$ is the gauge group of the electroweak sector, which unifies the weak force [$\mathrm{SU}(2)_L$], and the electromagnetic force [$\mathrm{U}(1)_Y$] via the Higgs mechanism. In this thesis we do concentrate on quantum chromodynamics (QCD), the theory describing the strong force and being the $\mathrm{SU}(3)_C$ part of Eq. (1.1).

The QCD Lagrangian reads

$$\mathcal{L}_{\mathrm{QCD}} = \sum_{A=1}^{3} \sum_{f=1}^{6} \sum_{\alpha,\alpha'=1}^{4} \bar{q}_{\alpha,f,A} \left(\gamma^{\mu}_{\alpha,\alpha'} i D_{\mu} - m_f \delta_{\alpha,\alpha'} \right) q_{\alpha',f,A} + \mathcal{L}_{\mathrm{gluon}}, \tag{1.2}$$

where f is the flavor index for the six spin-half quarks, α is the Dirac spinor index, and A is the color index. The above written Lagrangian is globally invariant under SU(3) color gauge transformations. The theory is made locally invariant under gauge transformations by the introduction of gauge fields A^a_{μ} and the covariant derivative,

$$\partial_{\mu} \rightarrow D_{\mu} = \partial_{\mu} - ig \frac{\lambda_a}{2} A^a_{\mu}, \tag{1.3}$$

where λ_a are the SU(3) Gell-Mann matrices. The kinetic gluon term is

$$\mathcal{L}_{\mathrm{gluon}} = -\frac{1}{4} G^a_{\mu\nu} G^{\mu\nu}_a, \tag{1.4}$$

with the gluon field strength tensor $G^a_{\mu\nu} = \partial_{\mu} A^a_{\nu} - \partial_{\nu} A^a_{\mu} + g f^{abc} A^b_{\mu} A^c_{\nu}$. f^{abc} are the SU(3) structure constants. By comparison with abelian gauge theories like quantum electrodynamics, the non-abelian

structure leads to phenomena like gluon self-interaction, quark confinement and asymptotic freedom. The strong coupling constant is defined by $\alpha_S = g^2/(4\pi)$. In contrast to quantum electrodynamics, where the coupling constant runs weakly and is small, $\alpha_{\mathrm{EM}} \approx 1/137$, the coupling constant α_S runs strongly depending on the momentum scale of the system. Its theoretical and experimental values are shown in Fig. 1.1.

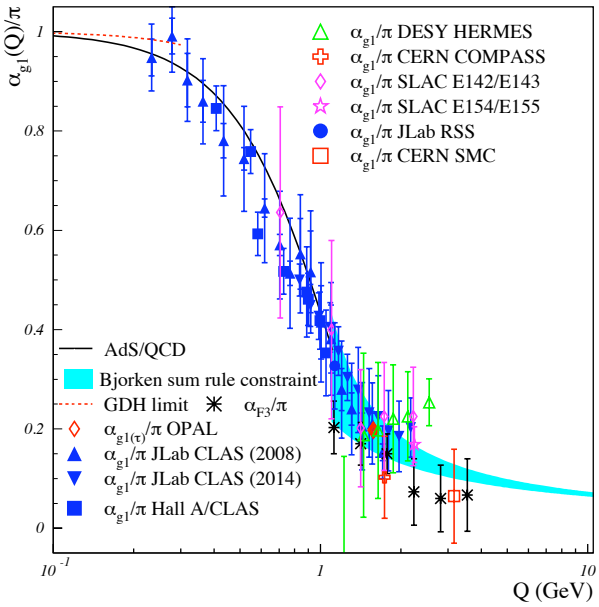

Figure 1.1: Running coupling constant for the strong force α_S. Figure taken from [1].

Although QCD can be solved perturbatively for $Q > 1$ GeV due to asymptotic freedom, this is not the case in the low-energy region, where $\alpha_S \approx 1$. This strong coupling is responsible for quark confinement and makes it necessary to use non-perturbative methods like lattice QCD or to use an effective field theory approach. Both methods are explained in the subsequent sections.

While lattice QCD and effective theory are highly successful in the two- and partly three- and four-body sector, one has to use different methods for the description of many-body physics. The reason is that an extension of the corresponding Faddeev-Yakubovsky equations become impractical to solve. There are various many-body methods whereas we just name a few in the following. Firstly we have coupled cluster theory or shell/no-core shell models, which use phenomenological Lagrangians as input. Secondly, there are Green's function Monte Carlo methods which combine variational methods with Monte Carlo methods for the evaluation of integrals. This method is rather successful and details will be given below.

In this thesis we will use a third approach, namely the nuclear lattice effective field theory (NLEFT), where the interactions are determined from *ab initio* $2N$ and $3N$ interactions based on chiral effective theory. Moreover, the space is discretized, such that a natural cutoff Λ arises by the lattice spacing a, $\Lambda = \pi/a$ and exact methods as well as statistical methods known from Lattice QCD are used for the evaluation of binding energies, phase shifts, etc. for two-, few- and many-body problems.

1.2 Lattice QCD

Lattice QCD is a non-perturbative method for solving QCD in the low-energy region. Generally, one calculates correlation functions in a discretized space-time using Monte Carlo methods. In the following

we give a very short introduction with a focus on the questions which will arise throughout this thesis. A thorough introduction can be found in [2].

Starting point is the partition function,

$$Z = \int \mathcal{D}A\mathcal{D}\Psi\mathcal{D}\bar{\Psi}\, \exp\left\{-S_F\left[\Psi,\bar{\Psi},A\right] - S_G[A]\right\}, \tag{1.5}$$

where A is the gauge field, and Ψ the fermion field. S_F and S_G are the fermion and gauge actions. Any correlation function of two operators $\hat{O}_1, \hat{O}_2$ can be calculated by taking its average,

$$\left\langle \hat{O}_2(t)\hat{O}_1(0)\right\rangle = \frac{1}{Z}\int \mathcal{D}A_\mu\mathcal{D}\Psi\mathcal{D}\bar{\Psi}\, \hat{O}_2\left[\Psi,\bar{\Psi},A\right]\hat{O}_1\left[\Psi,\bar{\Psi},A\right]\exp\left\{-S_F\left[\Psi,\bar{\Psi},A\right] - S_G\left[A\right]\right\}. \tag{1.6}$$

where the imaginary time $t = i\tau$ has been introduced already for the Euclidean rotation. While the Eqs. (1.5) and (1.6) are only formal expression, the respective discretized version is solvable numerically. Therefore, we put the system in a box of size $Na \times Na \times Na \times N_T a_T$, where a is the spatial lattice spacing and a_T the temporal lattice spacing. N, N_T are the number of nodes in spatial and temporal directions. For the discretization, one defines all fields and operators on the lattice points and substitutes continuous derivatives by finite differences. Then one uses Monte Carlo methods to calculate any observables from their respective correlation function. In such an approach, we have three main sources of artifacts. Firstly, one has to do infinite time extrapolations for observables, where one mostly expects an exponential decay and which gives a certain uncertainty. Secondly, the volume L^3 may cause an error if it is not large enough. Thirdly, the lattice spacing a itself produces a lattice artifact which makes an extrapolation to the continuum necessary or to improve the disctretization scheme. In a very simple lattice QCD calculation the lattice spacing error is linear, but one can use a different discretization scheme or include more operators in order to push this error to higher order. Symanzik's improvement program gives a clear strategy to do this [3, 4]. Note that additionally, the quark mass plays an important role for the efficiency of the algorithm, as one may be forced to do calculations at larger quark/ pion mass M_π and to finally extrapolate to the physical point. Nowadays, lattice calculations use parameters in the range of $a \sim 0.05 - 0.15$ fm, $L \sim 2 - 4$ fm and $M_\pi \sim 134 - 450$ MeV. Lattice QCD is mainly successful in the description of two-meson or two-baryon physics and in the near future, it may work in the three-body sector as well [5–8].

1.3 Effective Theory

Effective theory played a role in particle physics already long before the discovery of quarks and the full formulation of the standard model. For example, Fermi's theory of the beta decay [9], $n \to pe^-\bar{\nu}_e$, where a neutron decays into a proton, an electron and a neutrino can be understood as an effective theory of the standard model. In a modern language, the process is mediated by a W-boson with a mass of $m_W = 80$ GeV as shown in Fig. 1.2. As long as we remain in the low-energy regime in which $q^2 \ll m_W^2$, the propagator can be replaced by a contact interaction that is equivalent to Fermi's contact interaction.

In the low-energy limit of quantum chromodynamics a similar approach can be employed. Due to the strong coupling resulting in quark confinement, the quarks always form colorless objects, namely hadrons and it is impossible to observe single quarks or gluons. This means that quarks and gluons are not a suitable set of degrees of freedom, so we could formulate our theory with a new set of degrees of freedom. Naturally, hadrons are such a suitable set of degrees of freedom as they are observable at the low-energy scale.

For the construction of the new Lagrangian, only the symmetries of QCD must be preserved, which

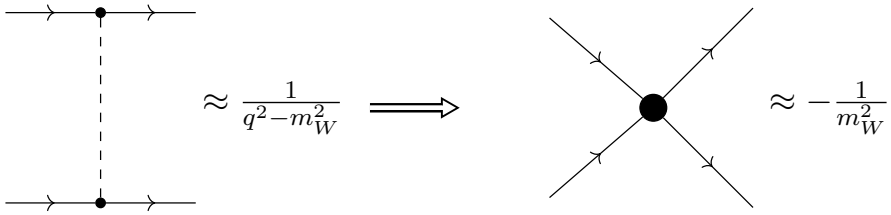

Figure 1.2: Fermi's beta decay. Left: Exact picture. Right: Effective picture for $q^2 \ll m_W^2$.

leads to the emergence of infinitely many terms and a non-renormalizable theory in general. Once all terms are included, one reproduces the underlying theory exactly, as stated by Weinberg [10],

> "if one writes down the most general possible Lagrangian, including all terms consistent with assumed symmetry principles, and then calculates matrix elements with this Lagrangian to any given order of perturbation theory, the result will simply be the most general possible S-matrix consistent with analyticity, perturbative unitarity, cluster decomposition and the assumed symmetry principles. "

Fortunately, not all terms are equally important and a power counting scheme is introduced to classify the importance of the terms. Consequently, one has to deal only with a finite number of terms at each order and the theory is exact up to higher-order terms which are truncated. Such a power counting expands in $O(Q/\Lambda)$, where Q is a small expansion parameter with respect to the breakdown scale of the theory, Λ. Once a counting scheme is set up, it can be used to classify quantum corrections in the form of Feynman loops as well and now it is possible to solve the theory completely up to an accuracy of $O(Q/\Lambda)$ in an energy region below Λ. To be specific, we start from the Lagrangian written in Eq. (1.2). On the one hand, the masses of the u-, d-, and s-quark are given by 2.2 MeV, 4.7 MeV and 96 MeV, and they are called light quarks. On the other hand, the masses of the c-, b- and t-quark are given by 1.28 GeV, 4.18 GeV and 173.1 GeV, and they are called heavy quarks. As we stay in the low-energy limit, we can neglect the heavy quarks and integrate them out of the theory. Then Eq. (1.2) reduces to the light quark sector with $f = 1, 2, 3$. By assuming the light quark masses to vanish in the so-called chiral limit, a new $\mathrm{SU}(3)_L \times \mathrm{SU}(3)_R$ symmetry emerges in the flavor sector, whose ground state symmetry is spontaneously broken to $\mathrm{SU}(3)_V$. Over and above neglecting the heavy quark sector, one could integrate out the s-quark as well, and we have a $\mathrm{SU}(2)_L \times \mathrm{SU}(2)_R / \mathrm{SU}(2)_V$ symmetry where pions are the respective Goldstone bosons of the theory. With these symmetry groups in mind, one builds up the whole Lagrangian. In the meson sector, this work started in the 1980s mainly by Gasser and Leutwyler in the framework of chiral perturbation theory (ChPT) [11, 12]. The first extension to the two-nucleon sector was done by [13, 14]. In the following two decades this framework has been extended to the baryon-meson sector in the non-relativistic approach of heavy-baryon ChPT (HBChPT) [15, 16] and the relativistic approach of extended on-mass shell (EOMS) renormalization scheme [17, 18]. An extended review on chiral perturbation theory in the meson- and one-nucleon sector is given by [19, 20]. While the meson sector must be formulated relativistically due to the lightness of its constituents, the meson-baryon sector can be formulated in both ways, and the nucleon-nucleon sector is formulated non-relativistically.

In the formulation of the nucleon-nucleon action an important question concerning the scales appears. Generally, the scale is set by the breakdown scale of ChPT, $\Lambda_{\mathrm{ChPT}} \sim 4\pi F_0 \sim 1.2$ GeV with the pion decay constant $F_0 = 92.1$ MeV. However, in most of the reactions vector meson resonances play a role although they are not included explicitly. This results in a decrease of validity below the ρ resonance, $M_\rho \sim 770$ MeV. In the nucleon sector we do not use dimensional regularization or power-divergence subtraction schemes for the absorption of possible ultraviolet divergences, but we use a momentum cutoff

for the regularization of nucleon-nucleon potentials. As the cutoff should reflect the validity range of the theory, one should use a more conservative approach and the breakdown scale is mainly chosen as $\Lambda \sim 500$ MeV [21, 22].

While the upper scale is set by $\Lambda \sim 500$ MeV we could also look at the opposite limit. In the former picture of meson-mediated interaction the nucleon-nucleon interaction is mediated by pion exchange similar to the already mentioned Fermi's beta decay with the W boson as exchange particle. If we remain below the pion scale of $M_\pi \sim 140$ MeV in momentum or do only consider objects larger than $1/M_\pi \sim 1.5$ fm, the effective theory can be reduced to the pionless theory simplifying the problem dramatically. Within such an approach it is possible to calculate very-low energy observables like the deuteron binding energy of -2.224 MeV or the ${}^1S_0$ scattering length of the nucleon-nucleon scattering, -23.8 fm. A review on pionless EFT can be found in [23]. It has been used to calculate bound states, scattering properties, etc. in the two-body sector using the well-known T-matrix formalism or Faddeev-Yakubovsky and Skorniakov Ter-Martirosian equations in the three- and four-body systems. It is also possible to confirm the Tjon line [24], which is a predicted correlation between ^{3}H and ^{4}He.

1.4 From nucleons to nuclei

Due to the rise of computational power and the development of efficient algorithms, we are now able to perform *ab initio* calculations not only for two- or three-body systems in nuclear physics, but also for many-body systems like medium-mass nuclei. Alpha-conjugate nuclei are of particular interest. They are formed of alpha-particles, which consist of two neutrons and two protons. Due to the Pauli principle alpha particles form a very compact object, a cluster, and alpha-like nuclei like ^{4}He, ^{8}Be, ^{12}C, ^{16}O, ^{20}Ne, etc. are a very good starting point for many-body calculations. We can even make a link to nuclear astrophysics, where one wants to understand the reactions in stars. For example, alpha-alpha scattering plays an important role in nucleosynthesis or in supernovae. Other examples are the Hoyle state or the production of oxygen via a carbon-helium reaction. Then the Hoyle state [25, 26] is an excited state of ^{12}C, which must have a very precise energy gap to the ground state, such that the triple alpha process really creates enough carbon. The excited carbon state ^{12}C* is created by a ^{8}Be and ^{4}He reaction, whereas the ^{8}Be itself is a product of alpha-alpha scattering. The Hoyle state partially decays electromagnetically into its ground state,

$$^{12}\mathrm{C}^* \rightarrow {}^{12}\mathrm{C} + \gamma. \tag{1.7}$$

The corresponding electromagnetic decay rate is very sensitive to the excited energy gap and it was Hoyle who predicted it to be around 7.65 MeV. In Ref. [27] the Hoyle state was detected at 7.653 ± 0.008 MeV. This anthrophic constraint makes this state an ideal candidate for testing nuclear theory and even the fine tuning of physical constants like the quark masses. Any *ab initio* many-body method should reproduce such fundamental processes. An overview on clustering effects in nuclei is given by [28].

1.5 Quantum Monte Carlo methods - status and open challenges

Generally, there are two approaches in Quantum Monte Carlo calculations, a continuum and a lattice approach, which are used for the estimation of physical properties of nuclei.

In continuum Monte Carlo theory, the first approach is a variational method called variational Monte Carlo (VMC) for the calculation of ground states, E_0. The basic idea is to minimize the energy E_V of the

trial wave function $|\Psi_T\rangle$,

$$E_V = \frac{\langle\Psi_T| H |\Psi_T\rangle}{\langle\Psi_T | \Psi_T\rangle} \geq E_0. \tag{1.8}$$

H is the Hamiltonian of the systems. It is crucial to find a trial wave function as close as possible to the exact ground state wave function. Therefore, it is suitable to make a separation ansatz,

$$|\Psi_T\rangle = \mathcal{F} |\Phi\rangle, \tag{1.9}$$

where $\mathcal{F}$ reflects the short-range physics while $|\Phi\rangle$ is optimized for the long-range part. The short-range part consists of pair functions fulfilling a modified Schrödinger-equation that includes the exact Schrödinger equation as well as variational modifications. The long-range part just reflects the antisymmetry of the wave function. One of the severe problems is the exponential scaling of required computer time with the number of particles making it hard to use in the many-body sector. Nowadays, VMC is used to create good trial wave functions $|\Psi_T\rangle$ for a time-evolution which leads to the ground state at infinite time. This method is called Green's function Monte Carlo, where the ground state wave function is defined as

$$|\Psi_0\rangle = \lim_{\tau\to\infty} \exp\left[-(H - E_0)\,\tau\right] |\Psi_T\rangle. \tag{1.10}$$

E_0 is introduced for normalization reasons of the wave function and it can be identified with the ground state energy. It is not possible to calculate the equation for infinite times, and one therefore evaluates the equation for several time steps. After N time steps the wave function reads

$$|\Psi_0\,(R)_N\rangle = \prod_{1\ldots N} \left\langle \vec{R}_N \right| \exp\left[-(H - E_0)\,\tau\right] \left|\vec{R}_{N-1}\right\rangle \ldots \left\langle \vec{R}_1 \right| \exp\left[-(H - E_0)\,\tau\right] \left|\vec{R}_0\right\rangle |\Psi_T\rangle. \tag{1.11}$$

$\vec{R}_i$ are the possible paths and they can be calculated using Monte Carlo methods. Nevertheless, the scaling is again very bad, and it is difficult to scale this up to many-particle calculations. This scheme can be modified by the introduction of auxiliary fields which change the two-particle interaction to a one-particle interaction via Hubbard-Stratonovitch transformation. Green's function Monte Carlo was used to calculate light and medium-mass nuclei mainly up to oxygen-16 [29, 30] and for the calculation of the Hoyle state, where the theoretical prediction is 10.4(5) MeV, which is far off from the experimental value of 7.65 MeV [31].

Another approach is NLEFT, which discretizes space (and time) and uses the chiral Lagrangian as the underlying theory making ab initio calculations possible. Generally, one confines the physical system in a discrete box of size L^3 with spatial lattice length $L = N_L a$ with N_L nodes and lattice spacing a. Finally, one solves the Schrödinger equation

$$H |\Psi\rangle = E |\Psi\rangle, \tag{1.12}$$

using the Lanczos algorithm for sparse matrices. This approach scales at least with $L^{3(N_p-1)}$, where N_p is the number of particles and even stronger if the particles have inner spin-isospin structure. Hence it is limited to very few particles. For more particles, the time direction is discretized as well and Monte Carlo methods are used again to calculate the corresponding generating functional,

$$Z_A(t) = \langle\Psi_A| \exp(-Ht) |\Psi_A\rangle, \tag{1.13}$$

where $|\Psi_A\rangle$ is a prepared initial state. While any arbitrary initial state with non-zero overlap with the ground state would be applicable, it might be advisable to use states reflecting the expected symmetry of the ground state for improved convergence. A famous example is the Wigner SU(4) symmetry which is

almost fulfilled in nucleons. Then the energy at a given time step t is defined as

$$E_A(t) = -\frac{\partial \log Z_A(t)}{\partial t}, \tag{1.14}$$

and the ground state energy is calculated by an infinite time extrapolation

$$E_0 = \lim_{t\to\infty} E_A(t). \tag{1.15}$$

Details on NLEFT and its practical implementation will be given in Chap. 3.

This method was first used at leading order (LO) in the two-body sector [32] and rapidly extended to next-to-leading order (NLO) and next-to-next-to-leading order (N2LO) and the three-body sector as well as many-particle calculations. For details see [33] and references therein. The Hoyle state was calculated *ab initio* with a very high accuracy. In addition, it was shown that the quark masses can vary by only 2 before the carbon production collapses and life as we know it becomes impossible [34, 35]. Another process was the first *ab initio* calculation of alpha-alpha scattering using the adiabatic projection method [36].

In spite of the quite impressive results in NLEFT, one has to look for possible issues of the theory with great detail to estimate the systematic errors and - if possible - find a way to reduce them. One of the main systematic errors is caused by the lattice discretization. Although such a discretization also exists in lattice QCD, the situation in NLEFT is different as the lattice spacing is linked to a cutoff, which should not exceed the physical breakdown scale of the theory. The standard lattice spacing for most of the calculations so far is $a = 1.97$ fm, which is approximately $\Lambda \approx 314$ MeV. The proton radius is ≈ 0.85 fm [37] equivalent to ≈ 730 MeV and the general cutoff of the theory is $\Lambda \approx 500$ MeV equivalent to 1.24 fm. This means that one should investigate physical observables, regularization schemes, etc. at least in the range from 1 fm to 2 fm for systematic errors and see whether or not they depend on the cutoff/ lattice spacing in this area. From a lattice QCD and/ or continuum EFT point of view it would be interesting as well to see whether one could decouple the lattice spacing from the cutoff, i.e. a fixed cutoff regulator for the effective potentials can be used thereby the lattice spacing can be sent to zero, such that its limit depends only on computational limits but not on physical ones [38].

Additionally, in the case of effective many-body calculations it was always necessary to introduce a four-body force to absorb lattice spacing errors. It has been argued that this artifact vanishes once the lattice spacing is small enough but it was never really tested. As a result, the Tjon line cannot be reproduced in the framework of NLEFT for coarse lattices while it is reproduced in continuum effective field theory.

As the nuclear effective theory includes a lot of additional operators in the sense of an effective theory, one could also include additional operators in the sense of Symanzik's improvement program [3, 4]. From a lattice theory point of view it is quite interesting to see whether we can set up a clear counting scheme that absorbs lattice spacing artifacts order-by-order and what is the applicability range of such a scheme.

This thesis is organized as the following.

Chap. 2 reviews effective field theory for few- and many-nucleon systems and the theory of scattering.

The aforementioned theory is transferred on the lattice in Chap. 3. We will explain the discretization procedure and give an introduction into solution methods – exact methods as well as Monte Carlo methods.

In Chap. 4 we have a look at the leading-order NN system with focus on the deuteron bound state and the S wave effective range expansion. The evolution of low-energy coupling constants as well as leading-order observables with respect to the lattice spacing are shown and arguments for a special

regularization of the one-pion exchange potential are given.

In Chap. 5 we make the transition from a NN system to the light nuclei triton and helium-4 where we focus on the correlation between both binding energies and show that we can reproduce the Tjon line once the spacing is chosen small enough.

Chap. 6 is dedicated to general properties of lattice effective field theory. Few-body bosonic systems in one dimension are investigated in the framework of Symanzik's improvement program, which systematically cancels lattice artifacts order-by-order making it possible to do better continuum extrapolations and produce results closer to the continuum already at large lattice spacings.

Finally, the thesis is summarized in Chap. 7 by giving an outlook on further questions and challenges in NLEFT.

CHAPTER 2

Theory

2.1 The effective theory of few-nucleon systems

In this section we construct the most general Lagrangian of the same symmetry properties as the underlying theory, QCD, focusing on the nucleon-nucleon interaction. We summarize the Lagrangian for nucleons and pions up to N2LO in the power counting framework. Afterward we will use this Lagrangian to construct all nucleon-nucleon interactions up to N2LO [39]. In the following we restrict ourselves to the SU(2) case, where only u- and d-quarks exist while all other quarks are integrated out. Then the symmetry of QCD in the chiral limit is

$$\mathrm{SU(2)_L} \times \mathrm{SU(2)_R} \times \mathrm{U(1)_V}, \tag{2.1}$$

where the subscript denotes left-handed and right-handed transformations in the SU(2) sector while only vector transformations are allowed in the U(1) sector. The Lagrangian should be invariant under such a symmetry even though the ground state of the theory should be invariant only under $\mathrm{SU(2)_V} \times \mathrm{U(1)_V}$ due to spontaneous symmetry breaking. Note that any continuous symmetry transformation leaving the Lagrangian invariant is linked to a conserved current. While a classical analysis results in a conserved current also for axial transformations in the U(1) sector, quantum corrections cancel the conservation and give rise to anomalies [40–42].

Before turning to the nucleon-nucleon interaction, we review the general ideas of ChPT in the meson sector. A possible realization is the so-called non-linear realization, where the pion fields $\vec{\pi}$ are organized in an exponential expression,

$$U = \exp\left(\frac{i\vec{\pi}\cdot\vec{\tau}}{F_0}\right). \tag{2.2}$$

Here, $\vec{\tau}$ are the isospin Pauli matrices and U has the transformation behaviour under chiral symmetry,

$$U \to RUL^\dagger, \tag{2.3}$$

where R and L are SU(2) matrices. The chiral symmetry breaking quark masses are implemented as well, and we treat their respective chiral symmetry transformation as if it is a spurion field building block,

$$M = \begin{pmatrix} m_u & 0 \\ 0 & m_d \end{pmatrix}, \qquad M \to RML^\dagger. \tag{2.4}$$

The leading-order Lagrangian in the pion sector reads

$$L_\pi^{(0)} = \frac{F_0^2}{4}\mathrm{Tr}\left(D_\mu U D^\mu U^\dagger\right) + \frac{F_0^2 B_0}{2}\mathrm{Tr}\left(MU^\dagger + M^\dagger U\right), \tag{2.5}$$

whereas B_0 is proportional to the quark condensate $\langle\bar{q}q\rangle$. The covariant derivative is constructed such that the Lagrangian is locally invariant. However, neglecting external currents, it is given by $D_\mu = \partial_\mu$ in the meson sector. By expanding Eq. (2.5) and assuming the isospin limit $m_u = m_d = \hat{m}$, we can identify the pion mass term,

$$M_\pi^2 = 2B_0\hat{m}. \tag{2.6}$$

In the pion-nucleon sector, the relativistic Lagrangian at LO reads

$$L^{(0)} = \Psi^\dagger\left(i\not{D} - m_0 + \frac{g_A}{2}\gamma^\mu\gamma_5 u_\mu\right)\Psi, \tag{2.7}$$

with m_0 the nucleon mass in the chiral limit, g_A the pion-nucleon coupling constant also in the chiral limit and the covariant derivatives without external currents,

$$D_\mu = \partial_\mu + \frac{1}{2}\left(u^\dagger\partial_\mu u + u\partial_\mu u^\dagger\right), \tag{2.8}$$

with $u^2 = U$ and u_μ the so-called chiral vielbein $u_\mu = i(u^\dagger\partial_\mu u - u\partial_\mu u^\dagger)$. The nucleons are summarized in $\Psi = (p, n)^T$. Beside the leading-order Lagrangian, one needs the next-to-leading-order one as well, and in its relativistic formulation it reads [43],

$$L^{(1)} = c_1\mathrm{Tr}\left(\chi_+\right)\Psi^\dagger\Psi + \frac{c_3}{2}\mathrm{Tr}\left(u^\mu u_\mu\right)\left(\Psi^\dagger\Psi\right) - \frac{c_4}{4}\Psi^\dagger\gamma^\mu\gamma^\nu\left[u_\mu, u_\nu\right]\Psi + \dots\ . \tag{2.9}$$

χ_+ contains the quark masses and it reads $\chi_+^\dagger = u^\dagger\chi u^\dagger + u\chi^\dagger u$ with $\chi = 2B_0 M$. The low-energy coupling constants c_1, c_3 and c_4 can be determined from pion-nucleon scattering observables like phase shifts or cross sections [44, 45]. Nowadays, the best method to pin down the LECs is the dispersive approach using Roy-Steiner equations [46]. Note that there are seven independent terms, but we only show the terms necessary in our analyses.

Including quantum corrections in the form of Feynman loop diagrams in baryon ChPT would lead to an inconsistent power counting scheme. This can be solved by the HBChPT approach or the EOMS renormalization scheme. As the nucleon-nucleon interaction is highly non-relativistic, one can use the former one. This is done by splitting the nucleon spinor into a heavy component and a light component. Finally, one can use only the light component in the Lagrangian. Details on this method and its application to pion-nucleon Lagrangians can be found in [15, 47].

Starting point for the nucleon-nucleon interaction is Weinberg's Lagrangian in its chiral expansion for nucleon fields Ψ and pion fields $\vec{\pi}$ at LO, NLO and N2LO. Subsequently, we give the Lagrangian in its non-relativistic form, as we concentrate on the nucleon-nucleon interaction,

$$\begin{aligned}\mathcal{L}^{(0)} =& \frac{1}{2}\partial_\mu\vec{\pi}\partial^\mu\vec{\pi} - \frac{1}{2}M_\pi^2\vec{\pi}^2 + \Psi^\dagger\left\{i\partial_0 + \vec{\sigma}\left[\frac{g_A}{\sqrt{2}F_\pi}\left(\vec{\sigma}\cdot\vec{\nabla}\right)\left(\vec{\tau}\cdot\vec{\pi}\right)\right] - \frac{1}{F_\pi^2}\vec{\tau}\cdot\left(\vec{\pi}\times\dot{\vec{\pi}}\right)\right\}\Psi \\ & - \frac{1}{2}C_S\left(\Psi^\dagger\Psi\right)\left(\Psi^\dagger\Psi\right) - \frac{1}{2}C_T\left(\Psi^\dagger\vec{\sigma}\Psi\right)\cdot\left(\Psi^\dagger\vec{\sigma}\Psi\right) - \frac{1}{2}C_U\left(\Psi^\dagger\vec{\tau}\Psi\right)\cdot\left(\Psi^\dagger\vec{\tau}\Psi\right) \\ & - \frac{1}{2}C_V\left(\Psi^\dagger\vec{\sigma}\,\vec{\tau}\Psi\right)\cdot\cdot\left(\Psi^\dagger\vec{\sigma}\,\vec{\tau}\Psi\right) + \dots\ ,\end{aligned} \tag{2.10}$$

$$\mathcal{L}^{(1)} = \Psi^\dagger \left[4c_1 M_\pi^2 - \frac{2c_1}{F_\pi^2} M_\pi^2 \vec{\pi}^2 + \frac{c_2}{F_\pi^2} \dot{\vec{\pi}} 2 + \frac{c_3}{F_\pi^2} \partial_\mu \vec{\pi} \cdot \partial^\mu \vec{\pi} - \frac{c_4}{2F_\pi^2} \epsilon_{ijk} \epsilon_{abc} \sigma_i \tau_a \left(\nabla_j \pi_b \right) \left(\nabla_k \pi_c \right) \right] \Psi$$
$$- \frac{D}{4F_\pi} \left(\Psi^\dagger \Psi \right) \left(\Psi^\dagger \vec{\sigma} \vec{\tau} \Psi \right) \cdot \vec{\nabla} \vec{\pi} - \frac{E}{2} \left(\Psi \Psi^\dagger \right) \left(\Psi \vec{\tau} \Psi^\dagger \right) \cdot \left(\Psi \vec{\tau} \Psi^\dagger \right) + \dots , \tag{2.11}$$

$$\mathcal{L}^{(2)} = \Psi^\dagger \left(\frac{\vec{\nabla}^2}{2m} \Psi \right) + \dots . \tag{2.12}$$

$\vec{\sigma}$ are the Pauli matrices in the spin space, g_A is the pion-nucleon coupling constant and m, M_π are the nucleon and pion masses in the isospin limit. The superscript denotes the counting in the Weinberg power counting scheme.

For the counting of any interaction we have to incorporate the vertices, propagators and loops in the right way. Weinberg's power counting formula reads

$$\nu = -4 + 2N + 2L + \sum_i V_i \Delta_i, \quad \Delta_i = d_i + \frac{1}{2} n_i - 2. \tag{2.13}$$

ν represents the power of (Q/Λ) whereas N is the number of nucleons and L is the number of pion loops. Additionally, the number of vertices of type i are given by V_i. Δ_i can be calculated from the number of nucleon operators n_i and the number of pion masses/ derivatives, d_i. Δ_i is always equal or larger than zero and there is only a finite number of diagrams at each order ν. This enables Weinberg's statement on effective theories, which can be solved order-by-order with a finite number of potential terms. LO calculations take into account all diagrams with $\nu = 0$, while NLO and N2LO calculations use all diagrams up to $\nu = 2$ and $\nu = 4$. Note that we have only included NLO corrections to pion-nucleon interaction in Eq. (2.11). Short-range corrections were included later by various groups, e.g. [48–51]. The free part of the nucleon Lagrangian is of order 2, which is just an artifact of the non-relativistic approach and it will be included at leading order [14]. Then the free leading-order nucleon Lagrangian reads

$$\mathcal{L}_N^{\text{free}} = \Psi^\dagger \left(i\partial_0 + \frac{\vec{\nabla}^2}{2m} \right) \Psi \tag{2.14}$$

From Eq. (2.10) we derive the pion propagator,

$$S_\pi = \frac{1}{\vec{q}^{\,2} + M_\pi^2 + i\epsilon}, \tag{2.15}$$

and Eq. (2.14) gives the non-relativistic nucleon propagator,

$$S_N = \frac{1}{E_0 - \frac{\vec{q}^{\,2}}{2m} + i\epsilon}. \tag{2.16}$$

With this in mind we can construct all respective potential terms up to N2LO as shown in Fig. 2.1. In Fig. 2.1 all possible terms are shown but not all terms contribute necessarily to the potential at given order. For example, the next-to-leading-order contributions to the three-body force vanish as they do not produce any new topology or cancel each other. Details can be found in [52]. Using unitary transformations [51], the leading order potential reads

$$V^{(0)} = -\frac{g_A^2}{4F_\pi^2} \frac{\vec{\sigma}_1 \cdot \vec{q} \vec{\sigma}_2 \cdot \vec{q}}{\vec{q}^{\,2} + M_\pi^2} \vec{\tau}_1 \cdot \vec{\tau}_2 + C_S + C_T \vec{\sigma}_1 \cdot \vec{\sigma}_2 + C_U \vec{\tau}_1 \cdot \vec{\tau}_2 + C_V \vec{\sigma}_1 \cdot \vec{\sigma}_2 \vec{\tau}_1 \cdot \vec{\tau}_2. \tag{2.17}$$

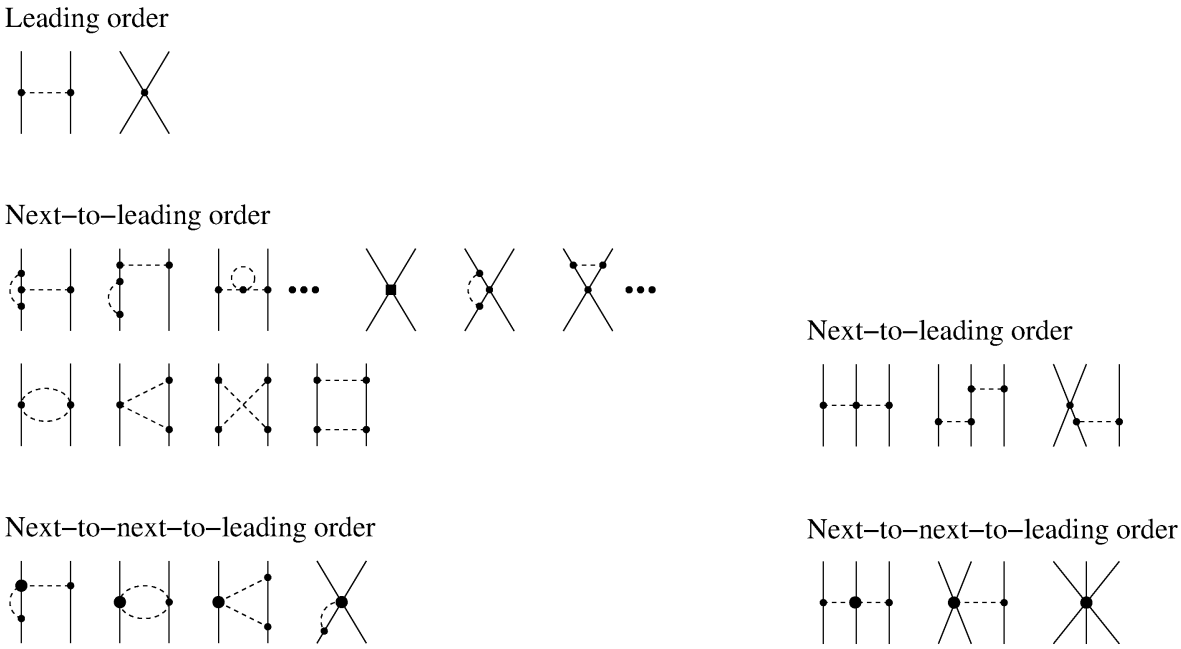

Figure 2.1: Chiral expansion of two-and three-body forces up to N2LO. Solid dots, filled circles and squares denote vertices with $\Delta_i = 0, 1$ and 2 according to Eq. (2.13). Figure taken from [52].

Here, $\vec{q}$ is the momentum transfer $\vec{q} = \vec{p} - \vec{p}\,'$ with the relative incoming and outgoing momenta, $\vec{p}^{\,(\prime)} = (\vec{p}_1^{\,(\prime)} - \vec{p}_2^{\,(\prime)})/2$. The index 1, 2 stands for the respective particle. Due to the antisymmetry condition of fermions, one can reduce the number of terms in Eq. (2.17) to two. Popular choices are the terms proportional to C_S and C_T, or C_S and C_U. At NLO, we have a loop contribution from the two-pion exchange potential (TPEP),

$$\begin{aligned} V_{\text{TPEP}}^{(1)} = &-\frac{\vec{\tau}_1 \cdot \vec{\tau}_2}{384\pi^2 F_\pi^4} L(q) \left[M_\pi^2 \left(5g_A^4 - 4g_A^2 - 1\right) + \vec{q}^{\,2} \left(24g_A^4 - 10g_A^2 - 1\right) + \frac{48 g_A^4 M_\pi^4}{4M_\pi^2 + \vec{q}^{\,2}} \right] \\ &- \frac{3g_A^4}{64\pi^2 F_\pi^4} L(q) \left(\vec{\sigma}_1 \cdot \vec{q} \vec{\sigma}_2 \cdot \vec{q} - \vec{\sigma}_1 \cdot \vec{\sigma}_2 \vec{q}^{\,2}\right), \end{aligned} \tag{2.18}$$

where $q = |\vec{q}\,|$ and $L(q)$ is a loop function which normally depends on a momentum cutoff $\tilde{\Lambda}$. Alternatively, if combined with dimensional regularization, one can use the following infinite cutoff expression,

$$\begin{aligned} L(q) &= \lim_{\tilde{\Lambda}\to\infty} \theta\left(\tilde{\Lambda} - 2M_\pi\right) \frac{\omega}{2q} \log \frac{\tilde{\Lambda}^2\omega^2 + q^2 s^2 + 2\tilde{\Lambda}\omega s}{4M_\pi^2\left(\tilde{\Lambda} + q^2\right)} \\ &= \frac{\sqrt{4M_\pi^2 + q^2}}{2q} \log \frac{\sqrt{4M_\pi^2 + q^2} + q}{\sqrt{4M_\pi^2 + q^2} - q} = \frac{\sqrt{4M_\pi^2 + q^2}}{q} \log \frac{\sqrt{4M_\pi^2 + q^2} + q}{2M_\pi}, \end{aligned} \tag{2.19}$$

with $\omega = \sqrt{4M_\pi^2 + q^2}$ and $s = \sqrt{\tilde{\Lambda} - 4M_\pi^2}$.

Beside the TPEP, short-range interactions appear and there are 14 terms which fulfill the symmetry

conditions,

$$\begin{aligned} V_{\text{contact}}^{(1)} =& C_1\vec{q}^{\,2} + C_2\vec{k}^{\,2} + \left(C_3\vec{q}^{\,2} + C_4\vec{k}^{\,2}\right)\vec{\sigma}_1\cdot\vec{\sigma}_2 + \left(C_5\vec{q}^{\,2} + C_6\vec{k}^{\,2}\right)\vec{\tau}_1\cdot\vec{\tau}_2 \\ &+ \left(C_7\vec{q}^{\,2} + C_8\vec{k}^{\,2}\right)\vec{\sigma}_1\cdot\vec{\sigma}_2\vec{\tau}_1\cdot\vec{\tau}_2 + iC_9\frac{1}{2}\left(\vec{\sigma}_1+\vec{\sigma}_2\right)\cdot\vec{q}\times\vec{k} \\ &+ iC_{10}\frac{1}{2}\left(\vec{\sigma}_1+\vec{\sigma}_2\right)\cdot\vec{q}\times\vec{k}\vec{\tau}_1\cdot\vec{\tau}_2 + C_{11}\vec{q}\cdot\vec{\sigma}_1\vec{q}\cdot\vec{\sigma}_2 + C_{12}\vec{q}\cdot\vec{\sigma}_1\vec{q}\cdot\vec{\sigma}_2\vec{\tau}_1\cdot\vec{\tau}_2 \\ &+ C_{13}\vec{k}\cdot\vec{\sigma}_1\vec{k}\cdot\vec{\sigma}_2 + C_{14}\vec{k}\cdot\vec{\sigma}_1\vec{k}\cdot\vec{\sigma}_2\vec{\tau}_1\cdot\vec{\tau}_2. \end{aligned} \tag{2.20}$$

Eq. (2.20) consists of 14 terms with correspondingly 14 LECs and depend not only on the transfer momentum $\vec{q}$ but also on the average momentum $\vec{k} = (\vec{p}\,' + \vec{p})/2$. However, one can use again antisymmetrization arguments to reduce the number of terms. Finally there are only seven independent terms. For example, [53] uses terms corresponding to C_1, C_2, C_3, C_4, C_9, C_{11} and C_{13}.

At N2LO we do not have any new two-body contact operators, but there is still a subleading part of the TPEP,

$$\begin{aligned} V_{\text{TPEP}}^{(2)} =& -\frac{3g_A^2}{16\pi F_\pi^4}\left(2M_\pi^2+\vec{q}^{\,2}\right)A(q)\left[2M_\pi^2(2c_1-c_3)-c_3\vec{q}^{\,2}\right] \\ &- \frac{g_A c_4\vec{\tau}_1\cdot\vec{\tau}_2}{32\pi F_\pi^4}\left(4M_\pi^2+\vec{q}\right)A(q)\left(\vec{\sigma}_1\cdot\vec{q}\vec{\sigma}_2\cdot\vec{q}-\vec{q}^{\,2}\vec{\sigma}_1\cdot\vec{\sigma}_2\right), \end{aligned} \tag{2.21}$$

where $A(q)$ is defined as

$$A(q) = \lim_{\tilde{\Lambda}\to\infty}\theta\left(\tilde{\Lambda}-2M_\pi\right)\frac{1}{2q}\arctan\frac{q\left(\tilde{\Lambda}-2M_\pi\right)}{q^2+2\tilde{\Lambda}M_\pi} = \frac{1}{2\pi}\arctan\frac{q}{2M_\pi}, \tag{2.22}$$

and dimensional regularization is employed. Furthermore, $3N$ forces start to appear and they read

$$\begin{aligned} V_{3N}^{(2)} =& \frac{g_A^2}{8F_\pi^4}\frac{\left(\vec{\sigma}_1\cdot\vec{q}_1\right)\left(\vec{\sigma}_3\cdot\vec{q}_3\right)}{\left(\vec{q}_1^{\,2}+M_\pi^2\right)\left(\vec{q}_3^{\,2}+M_\pi^2\right)}\left\{\left(\vec{\tau}_1\cdot\vec{\tau}_3\right)\left(-4c_1M_\pi^2+2c_3\vec{q}_1\cdot\vec{q}_3\right)\right. \\ &\left.+ c_4\left[\left(\vec{\tau}_1\times\vec{\tau}_3\right)\cdot\vec{\tau}_2\right]\left[\left(\vec{q}_1\times\vec{q}_3\right)\cdot\vec{\sigma}_2\right]\right\} - \frac{g_A D}{8F_\pi^2}\frac{\vec{\sigma}_3\cdot\vec{q}_3}{\vec{q}_3^{\,2}+M_p i^2}\left(\vec{\tau}_1\cdot\vec{\tau}_3\right)\left(\vec{\sigma}_1\cdot\vec{q}_3\right)+\frac{1}{2}E\left(\vec{\tau}_2\cdot\vec{\tau}_3\right) \\ &+ \text{all permutations}. \end{aligned} \tag{2.23}$$

Nowadays, there exist calculations in the two-body sector up to and including fifth order [22] while the three-nuclear force stops at N4LO [45, 54]. In the framework of the chiral counting, one might contemplate four-body forces as well, but they only start at N4LO and will be beyond the accuracy of any calculation we are considering.

2.2 Scattering Theory

2.2.1 Basic concepts of scattering theory

First of all, we give a basic introduction into scattering theory which follows [55, 56]. Starting point of non-relativistic quantum mechanics is the corresponding Schrödinger equation, which has the subsequent

form in the center-of-mass frame,

$$\left[-\frac{1}{2\mu}\Delta + V\left(\vec{r}\right)\right]\Psi\left(\vec{r}\right) = E\Psi\left(\vec{r}\right). \tag{2.24}$$

μ is the reduced mass, $V(\vec{r})$ is the interaction potential and E is the eigenenergy for the eigenfunction $\Psi(\vec{r})$. The dispersion relation between scattering energy and scattering momentum reads $E = \vec{q}^{\,2}/(2\mu)$. In the standard approach, one assumes an incoming wave function Ψ_{in} in z-direction while the outgoing wave function Ψ_{out} is a scattered spherical wave function. In the long-range limit, the potential vanishes or its absolute value has to fall off faster than the centrifugal potential, namely r^{-2} with $r = |\vec{r}|$. Then the asymptotic wave function can be described by the superposition,

$$\Psi\left(\vec{r}\right) \overset{r\to\infty}{\longrightarrow} \exp\left(iqz\right) + f\left(\theta,\phi\right)\frac{\exp\left(iqr\right)}{r}. \tag{2.25}$$

$f(\theta,\phi)$ is the scattering amplitude depending only on the angles θ and ϕ. Due to the particular choice of the incoming wave function, the momentum $\vec{q}$ is given by $\vec{q} = (0,0,q)$ which simplifies the calculations and particularly the partial wave decomposition. But it is also possible to investigate the more general case, where $\Psi(\vec{r})$ must be replaced by $\Psi(\vec{q},\vec{r})$. Although it is theoretically possible to solve Eq. (2.24) and impose the asymptotic boundary conditions of Eq. (2.25), one can also rewrite the first equation using Green's function. The free Green's function is given by

$$G\left(\vec{r},\vec{r}\,'\right) = -\frac{\mu}{2\pi}\frac{\exp\left(iq|\vec{r}-\vec{r}\,'|\right)}{|\vec{r}-\vec{r}\,'|}, \tag{2.26}$$

and fulfills the following equation

$$\left[\frac{1}{2\mu}\Delta + E + i\epsilon\right]G\left(\vec{r}-\vec{r}\,'\right) = \delta\left(\vec{r}-\vec{r}\,'\right). \tag{2.27}$$

Using the Green's function one transforms the differential equation in Eq. (2.24) into an integral equation for the wave function, the so-called Lippmann-Schwinger equation,

$$\Psi\left(\vec{r}\right) = \exp\left(iqz\right) + \int \mathrm{d}\vec{r}\,' G\left(\vec{r},\vec{r}\,'\right)V\left(\vec{r}\,'\right)\Psi\left(\vec{r}\,'\right). \tag{2.28}$$

While in the latter equation one still uses the explicit wave function, one can also rewrite the problem in terms of operators only. Therefore, we define the general T-matrix

$$T_{\beta\alpha}(E',E) = \left\langle \Psi_0\left(E',\beta\right)\middle| V_{\text{int}} \middle|\Psi\left(E,\alpha\right)\right\rangle, \tag{2.29}$$

where α,β are quantum numbers of the system, V_{int} the interaction potential and $\Psi_0(E',\beta)$ is a solution of the free system with energy E' and quantum number β. Furthermore, Ψ is a solution of the Lippmann-Schwinger equation according to Eq. (2.28) with energy E and quantum number α. Using the definition of the Green's function, we write the equivalent Lippmann-Schwinger equation for the T-matrix,

$$T(E) = V_{\text{int}} + V_{\text{int}}G(E)T(E), \tag{2.30}$$

whereas $T(E)$ is the on-shell version of Eq. (2.29) and $G(E)$ the on-shell version of the Green's function in momentum space with $E = E'$.

Most generally, a scattering state is described by the propagation of the incoming state through the interaction represented by the S-matrix,

$$\Psi_{\text{out}}(E) = S\Psi_{\text{in}}(E). \tag{2.31}$$

Alternatively, the S-matrix is given as the overlap of two free state solutions,

$$\left\langle \Psi_0\big(E_\beta,\beta\big)\right| S \left|\Psi_0\big(E_\alpha,\alpha\big)\right\rangle, \tag{2.32}$$

already indicating that one can still use free state solutions as basis states and think about a superposition of such states for the scattering solution. As the scattering matrix should be the unit matrix in the case of vanishing scattering potential, it is convenient to split the matrix into two terms,

$$\left\langle \Psi_0\big(E_\beta,\beta\big)\right| S \left|\Psi_0\big(E_\alpha,\alpha\big)\right\rangle = \underbrace{\left\langle \Psi_0\big(E_\beta,\beta\big)\middle|\Psi_0\big(E_\alpha,\alpha\big)\right\rangle}_{=\delta_{\alpha,\beta}} - 2\pi i\delta\big(E_\alpha - E_\beta\big)T_{\beta\alpha}\big(E_\alpha,E_\beta\big). \tag{2.33}$$

The first term is related to the amplitude, where the particle passes the interaction region without scattering whereas the second term includes all scattering information.

In the case of radially symmetric potentials, one can decompose the problem into solutions according to the spherical harmonics. Spherical harmonics are a system of eigenfunctions, which are defined on the sphere and which correspond to eigenfunctions of the angular momentum operator,

$$\hat{L}^2 Y_{l,l_z}(\theta,\phi) = l(l+1)Y_{l,l_z}(\theta,\phi), \tag{2.34}$$

$$\hat{L}_z Y_{l,l_z}(\theta,\phi) = l_z Y_{l,l_z}(\theta,\phi), \tag{2.35}$$

with the orbital angular momentum quantum number $l = 0, 1, 2, \ldots$ and the magnetic momentum quantum number $l_z = -l, -l+1, \ldots, l$. Such a system generates an infinite basis of eigenfunctions and any solution of the Schrödinger equation can be identified with the good quantum numbers l, l_z. Details on the properties and construction of the spherical harmonics Y_{l,l_z} are found in App. A. On the one hand, the decomposition into partial waves already facilitates the problem as the degrees of freedom are reduced to the radial one. On the other hand, it also introduces a reasonable hierarchy of partial waves as the lowest-lying partial waves are the most important ones for scattering processes while higher order partial waves hardly contribute to the full scattering wave. The reason is that the angular momentum contribution to the kinetic part $l(l+1)/(2\mu r^2)$ rises with higher angular momentum and serves as a barrier between the incoming particle and the interaction region such that any interaction is more and more suppressed with larger l.

To be specific, the wave function is divided into a radial part and a spherical part by the ansatz

$$\Psi(\vec{r}) = \sum_l \frac{u_l(r)}{r} P_l(\cos\theta), \tag{2.36}$$

where the system is chosen such that only the spherical harmonics with $m = 0$ contribute whereas $P_l(\cos\theta)$ are the Legendre polynomials. Furthermore, u_l is the solution of the radial part,

$$\left[-\frac{1}{2\mu}\Delta_r + \frac{l(l+1)}{2\mu r^2} + V(r)\right] u_l(r) = E u_l(r). \tag{2.37}$$

The free system with $V(r) = 0$ has two independent solutions, which consist of the Bessel functions of

the first and second kind, $j_l(qr)$ and $n_l(qr)$,

$$u_l^s(qr) = (qr) j_l(qr), \tag{2.38}$$
$$u_l^c(qr) = (qr) n_l(qr). \tag{2.39}$$

As the solutions are $\propto \sin(qr - l\pi/2)$ and $\propto -\cos(qr - l\pi/2)$ for large (qr), the real solution can be approximated by a superposition of the two free solutions, leading to

$$u_l(r) \xrightarrow{r\to\infty} A \sin\left(qr - l\frac{\pi}{2}\right) - B\cos\left(qr - l\frac{\pi}{2}\right) \xrightarrow{r\to\infty} \sin\left(qr - l\frac{\pi}{2} + \delta_l\right). \tag{2.40}$$

δ_l is the phase shift and it can be read off from the coefficients A, B immediately by

$$\tan\delta_l = \frac{B}{A}. \tag{2.41}$$

Alternatively, one expands the incoming partial wave of Eq. (2.25), rearranges the solution and uses Eq. (2.41) to get the form

$$u_l(r) \to \frac{2l+1}{2q} i^{2l+1} \left[\exp(-iqr) - (-1)^l \exp(2i\delta_l)\exp(+iqr)\right]. \tag{2.42}$$

Due to the orthogonality of the spherical harmonics, one can not only separate the contributions of the wave function according to their angular momentum, but also the Lippmann-Schwinger equation as well as the scattering matrix S_l themselves. For example, the S-matrix for angular momentum l reads

$$S_l = \exp\left(2i\delta_l\right). \tag{2.43}$$

Then the full scattering matrix S is given by the sum $S = \sum_l S_l$. In the former Eqs. (2.38) to (2.40) we see that momentum q and position r always appear as a pair (qr) and one could think about the very low-energy limit of the equations. The Wronskian method uses the asymptotic wave function of Eq. (2.40) with and without interaction at zero momentum approximation and gives the following equation,

$$q^{2l+1}\cot(\delta_l) = -\frac{1}{a_s} + \frac{r_e}{2}q^2 + O(q^4), \tag{2.44}$$

with a_s the scattering length and r_e the effective range. The term on the left can be analytically expanded around zero-momentum as the phase shift is $\delta_l \propto q^{2l+1}$ for $q \to 0$. It can be shown that the scattering length is the zero of the asymptotic wave function in the zero-energy limit. In the case of repulsive or only weakly attractive potentials, the scattering length and the effective range are indeed approximately in the range of the potential. The effective range expansion can be linked to the scattering matrix,

$$S_l = \exp(2i\delta_l) = 1 + 2iq^{2l+1}\frac{1}{q^{2l+1}\cot\left(\delta_l\right) - iq^{2l+1}}, \tag{2.45}$$

and the projected scattering amplitude

$$f_l = \frac{(2l+1)q^{2l}}{q^{2l+1}\cot_l\left(\delta\right) - iq^{2l+1}}, \tag{2.46}$$

whereas f_l is given by $f(\theta) = \sum_l f_l P_l(\cos\theta)$. Bound states appear as poles in the scattering amplitude

of Eq. (2.46) and due to the effective range expansion, the leading-order approximation of the binding energy in terms of the scattering length is given by

$$E_B = \frac{1}{2\mu a_s^2}. \tag{2.47}$$

Though the effective range expansion is very well established only for S waves, we have shown the general form for arbitrary angular momentum in three dimension and it can be further generalized for arbitrary dimension as well. Details on the method can be found in [57] and references therein.

2.2.2 Extension to systems with internal degrees of freedom and coupled channels

As we use nucleons as degrees of freedom, the partial waves must be characterized by their spin and isospin content as well. This is why Eq. (2.36) does not hold generally for angular momentum larger than zero, and one has to sum over all magnetic quantum numbers as well. Consequently, the partial waves are described by orbital angular momentum, its magnetic quantum number and the internal degrees of freedom spin and isospin, which are summarized in the spin-isospin vector χ_i,

$$\Psi(\vec{r}) = \sum_i \Psi_i(\vec{r}) = \sum_l \sum_{l_z=-l}^{l} \sum_i \frac{u_{i,l,l_z}(r)}{r} Y_{l,l_z}(\theta,\phi)\chi_i. \tag{2.48}$$

Now the radial projected Schrödinger equation reads

$$\left[-\frac{1}{2\mu}\Delta_r + \frac{l(l+1)}{2\mu r^2}\right] u_{i,l,l_z}(r) + \sum_{i',l',l'_z} V(i,l,l_z;,i',l',l'_z) u_{i',l',l'_z}(r) = E u_{i,l,l_z}(r). \tag{2.49}$$

Here, $V(i,l,l_z;i',l',l'_z)$ is the projected potential

$$V(i,l,l_z;i',l',l'_z) = \left\langle Y_{l,l_z}(\theta,\phi)\chi_i \middle| V \middle| Y_{l'l'_z}(\theta,\phi)\chi_{i'} \right\rangle. \tag{2.50}$$

The new radial Schrödinger equation generally couples different partial wave channels. In the case of nucleon-nucleon scattering, we have partial waves with the same total angular momentum j but different orbital angular momentum l, which couple for $l = j \pm 1$. Examples are ${}^3S_1 - {}^3D_1$, ${}^3P_2 - {}^3F_2$ and ${}^3D_3 - {}^3G_3$.

After expanding the wave function with specific internal degree of freedom i,

$$\Psi_i(\vec{r}) = \sum_l \sum_{l_z} \frac{u_{i,l,l_z}(r)}{r} Y_{l,l_z}(\theta,\phi), \tag{2.51}$$

the wave function can be rewritten in terms of the S-matrix,

$$\begin{aligned}\Psi_{i'}(\vec{r}) =& \delta_{i,i'} \exp(iq_i z) \\ &+ \frac{\exp(iq_i r)}{r} \sum_{l',l'_z} Y_{l',l'_z}(\theta,\phi)\, i \sum_l i^{l-l'} \sqrt{\frac{\pi(2l+1)}{q_i q_{i'}}} \left(\delta_{i,i'}\delta_{l,l'}\delta_{0,l'_z} - S_{i,l,0;i',l',l'_z}\right).\end{aligned} \tag{2.52}$$

Even though the parametrization in the single channel case is straightforward, there are generally two possibilities in the coupled channel case, the Blatt and Biedenharn parametrization [58, 59] as well as the

Stapp parametrization [60]. Using the Stapp parametrization, the S-matrix is given by

$$S = \begin{bmatrix} \exp\left(i\delta_{j-1}\right) & 0 \\ 0 & \exp\left(i\delta_{j+1}\right) \end{bmatrix} \begin{bmatrix} \cos\left(2\epsilon_j\right) & i\sin\left(2\epsilon_j\right) \\ -i\sin\left(2\epsilon_j\right) & \cos\left(2\epsilon_j\right) \end{bmatrix} \begin{bmatrix} \exp\left(i\delta_{j-1}\right) & 0 \\ 0 & \exp\left(i\delta_{j+1}\right) \end{bmatrix}, \tag{2.53}$$

where ϵ_j is the mixing angle between both channels. Again, the S-matrix can be used to propagate the incoming wave function Ψ_{in},

$$\Psi_{\text{in}} = -\frac{\exp\left[-i\left(qr - j\frac{\pi}{2}\right)\right]}{2iqr} \begin{bmatrix} \exp\left(-i\frac{\pi}{2}\right) & 0 \\ 0 & \exp\left(i\frac{\pi}{2}\right) \end{bmatrix} \begin{bmatrix} C \\ D \end{bmatrix}, \tag{2.54}$$

via Eq. (2.31) to the outgoing function Ψ_{out},

$$\begin{aligned} \Psi_{\text{out}} = S\Psi_{\text{in}} = &-\frac{\exp\left[-i\left(qr - j\frac{\pi}{2}\right)\right]}{2iqr} \\ &\times \begin{bmatrix} C\exp\left(i\frac{\pi}{2} + 2i\delta_{j-1}\right)\cos\left(2\epsilon_j\right) + iD\exp\left(i\frac{\pi}{2} + \delta_{j-1} + \delta_{j+1}\right)\sin\left(2\epsilon_j\right) \\ D\exp\left(-i\frac{\pi}{2} + 2i\delta_{j-1}\right)\cos\left(2\epsilon_j\right) + iC\exp\left(-i\frac{\pi}{2} + \delta_{j-1} + \delta_{j+1}\right)\sin\left(2\epsilon_j\right) \end{bmatrix}. \end{aligned} \tag{2.55}$$

A more detailed derivation can be found in [61]. After having defined the incoming and outgoing wave functions, one should follow the procedure in the uncoupled case, where one redefines the full wave in terms of a standing wave. Further details for the concrete calculation of phase shifts and mixing angles are given in Subsec. 3.4.2.

2.2.3 Scattering theory for Coulomb forces

Beside the strong interaction between particles, we also have the electromagnetic interaction, which must be treated separately. The beforementioned considerations concerning the solution of the free system only hold for an effective potential $\propto 1/r^2$ due to angular momentum and all other interactions must fall off with $1/r^a$ with $a \geq 2$. Including the Coulomb force results in a different effective potential and leads to a new radial Schrödinger equation,

$$\left[-\Delta_\rho + \frac{l(l+1)}{\rho^2} + \frac{2\eta}{\rho}\right] u_l(\rho) = u_l(\rho). \tag{2.56}$$

with $\rho = qr$ and $\eta = \mu\alpha_{\text{EM}}/q$. For such a system, we have again two solutions, a regular one,

$$F_l(\eta,\rho) = 2^l \exp\left(\frac{-\pi}{2}\eta\right) \frac{|\Gamma(l+1+i\eta)|}{(2l+1)!} \exp(-i\rho)\,\rho^{l+1} F(l+1-i\eta, 2l+2; 2i\rho), \tag{2.57}$$

and an irregular one,

$$G_l(\eta,\rho) = iF_l(\eta,\rho) + \exp\left(\frac{\pi}{2}\eta\right) \frac{|\Gamma(l+1+i\eta)|}{\Gamma(l+1+i\eta)} \exp\left[-i\left(\rho - l\frac{\pi}{2}\right)\right] (2i\rho)^{l+1} U(l+1-i\eta, 2l+2; 2i\rho). \tag{2.58}$$

F and U are hypergeometric functions and explicit forms are given in App. A. These solutions are more general than the Bessel functions, and it can be shown that their asymptotic behavior is the same as the

one for Bessel functions in the case of vanishing Coulomb interaction,

$$F_l(\eta,\rho) \xrightarrow{\rho\gg 1} \sin\left(\rho - \eta\log(2\rho) - l\frac{\pi}{2} + \sigma_l\right) \xrightarrow{\eta\to 0} \sin\left(\rho - l\frac{\pi}{2}\right), \tag{2.59}$$

$$G_l(\eta,\rho) \xrightarrow{\rho\gg 1} \cos\left(\rho - \eta\log(2\rho) - l\frac{\pi}{2} + \sigma_l\right) \xrightarrow{\eta\to 0} \cos\left(\rho - l\frac{\pi}{2}\right). \tag{2.60}$$

Here, $\sigma_l = \arg[\Gamma(l+1+i\eta)]$ is the Coulomb phase. Now, we already see that the asymptotic solutions with vanishing Coulomb interaction are the same as in Eqs. (2.38) and (2.39) (up to a sign). Hence, one can use exactly the same strategies as already explained in the case without Coulomb interaction.

2.3 Correlations in Few-Body physics

Correlations between few-body systems of different number of particles are an important test for the predictability of modern theory of nuclear interaction. A famous but rather technical example is the N-boson system in one dimension with attractive two-body δ-interaction $V_{ij} = C_0\delta(x_i - x_j)$, where x_i, x_j are the positions of the boson i, j, while C_0 determines the strength of the two-body interaction. This model can be solved exactly for any number of particle [62] and e.g. the general binding energy for N bosons with mass m reads

$$E_B^{N\mathrm{b}} = -\frac{m}{24}C_0^2 N(N^2-1). \tag{2.61}$$

In the case of three dimensions, such a model is not exactly solvable anymore and one has to rely on numerical calculations. Instead of the Lippmann-Schwinger equations, one has to use Faddeev equations in the three-body sector or Faddeev-Yakubovsky equations in the four-body sector [63–65]. In the case of pionless EFT, there exists the special case of Skorniakov-Ter-Martirosian equations [66] and a formulation including dimeron fields [67]. Going beyond four particles becomes very difficult for an explicit calculation and one should generally deliberate other methods.

In the three-body sector, the phenomena of universal Efimov physics appear in three dimensions. While the exact physical system (e.g. cold atoms, nuclear physics, etc.) does not play a role, Efimov physics only relies on an infinite (or at least large) scattering length in the two-body system. Then it can be shown that an infinite number of three-body bound states exists which accumulate at zero binding energy and which makes a three-body force necessary to determine the three-body physics uniquely. A closely related correlation is the Philips line [23, 68, 69], which is a linear correlation between the spin-doublet neutron-deuteron scattering length $a_{nd}^{1/2}$ and the triton binding energy $E_{^3\mathrm{H}}$ for various two-body interactions fitted to the same two-body scattering observables. At the same time, various calculations act slightly differently on the three-body physics and they must be fixed by the three-body force.

In this thesis, we focus on the Tjon line or Tjon band. Tjon calculated the correlation between three-body and four-body systems using a two-body interaction consisting of an attractive and a repulsive Yukawa-type term [24]. The coefficients were fitted to reproduce S wave properties while the Fadeev-Yakubovsky three- and four-body equations were examined. Depending on the solution, various pairs of three- and four-body bound states were found which are all along a line as seen in Fig. 2.2 and which results in a conjecture that four-body forces are not necessary [70].

Indeed, this calculation was done using only a phenomenological Lagrangian and the question is whether it still holds for chiral EFT and a modern formulation of nuclear interaction. In the framework of chiral potentials the Tjon line was confirmed for several data points in [70, 71] using the Faddeev-Yakubovsky approach. The Faddeev-Yakubovsky approach with pionless EFT potentials gives an error

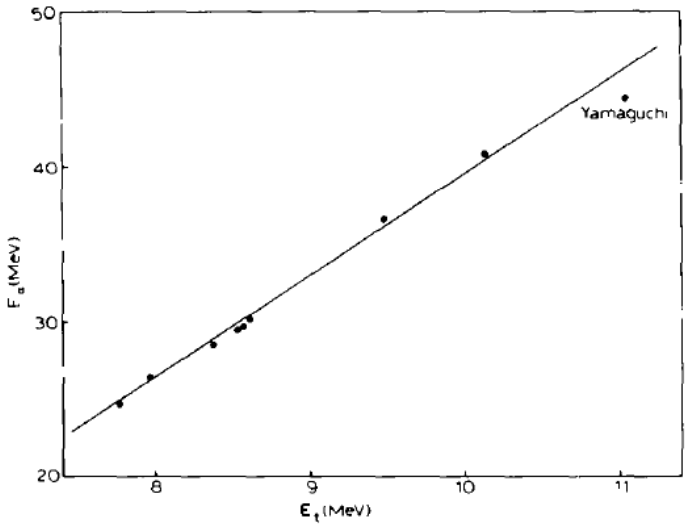

Figure 2.2: The original Tjon line. The dots are various predictions for different local potentials. Reprinted from [24] with permission from Elsevier.

estimation for the Tjon line, transforming it into a band, where all chiral calculations should lie within [72]. Other calculations were done by [73] and the results of the various analyses are summarized in Fig. 2.3. Generally, all of them are reproducing the Tjon line, but depending on the method, they also give a width or only give results for a specific pair of the triton and the helium-4 binding energy.

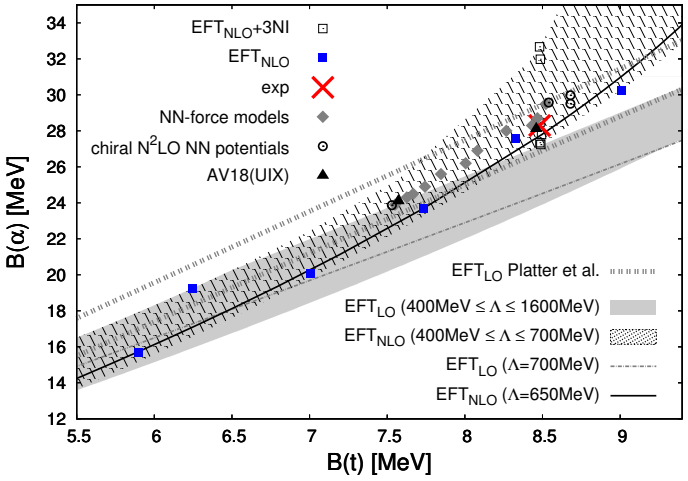

Figure 2.3: Various estimations of the ^{3}H-^{4}He binding energy correlation. The squares are pionless EFT results at NLO with and without 3NF calculated in [73]. The chiral potentials were calculated in [71]. The EFT calculations use resonance group methods and are reported in [73] whereas the original Tjon band by Platter *et. al.* was calculated in [72]. The plot is taken from [73].

CHAPTER 3

Nuclear Lattice Effective Field Theory

In NLEFT, the degrees of freedom are nucleons and pions rather than quarks and gluons as in lattice QCD. Hence, we have to discretize the previous Hamiltonians in all spatial dimensions. If one uses Monte Carlo methods and the infinite time extrapolation, then one also has to discretize it in its temporal dimension. In the following we explain how to put the system in a discrete box of finite volume and how we could use finite volume effects to extract physical information in the infinite volume. Moreover, we explain the Monte Carlo methods and discuss limits of this method like the sign problem.

3.1 Effective theory on the lattice

As already mentioned, we have to discretize all operators so that they are defined on the lattice and the explicit form of discretization for any operator will be given explicitly in the subsequent chapters. Here we want to examine some specific problems, namely the smearing of nucleon-nucleon contact interactions and the discretization of the one-pion-exchange potential, which puts the link between lattice spacing, discretization and the validity of effective field theory in a focus. We start with the smearing of the contact interactions. From an effective field theory point of view we can construct only momentum-independent zero-range interactions at leading order. However, such a contribution leads to a clustering instability and a strongly overbound ^{4}He state. These effects are reduced by a Gaussian smearing in momentum space [32]. For example the simplest contact interaction for a two-body system without spin is smeared as

$$V_{\text{int}} = \sum_{\vec{n}} : a^\dagger(\vec{n})\, a(\vec{n})\, a^\dagger(\vec{n})\, a(\vec{n}) : \longrightarrow \sum_{\vec{n},\vec{n}'} f\left(\vec{n}-\vec{n}'\right) : a^\dagger(\vec{n})\, a(\vec{n})\, a^\dagger\left(\vec{n}'\right) a\left(\vec{n}'\right) :, \tag{3.1}$$

where : : means normal ordering of the creation and annihilation operators. The smearing function $f(\vec{n}-\vec{n}')$ is defined as

$$f\left(\vec{n}-\vec{n}'\right) = \frac{1}{L^3 f_0} \sum_{\vec{q}} \exp\left(-b\frac{\vec{q}^{\,2n}}{2}\right) \exp\left[i\vec{q}\cdot\left(\vec{n}-\vec{n}'\right)\right], \tag{3.2}$$

with normalization constant f_0,

$$f_0 = \frac{1}{L^3} \sum_{\vec{q}} \exp\left(-b\frac{\vec{q}^{\,2n}}{2}\right). \tag{3.3}$$

b is a smearing parameter and n is chosen such that the smearing starts contributing at $O(q^{2n})$, which is the truncation order of the effective theory. A similar smearing takes place in QCD where it is used to reduce fluctuations and to improve the signal of correlation functions [2]. Furthermore, it is used in continuum effective field theory to render ultraviolet divergences finite [22, 53, 74]. The smearing of the contact interaction via local regulators increases the description of some partial waves, but it may decrease the prediciton in other channels. The reason is that the antisymmetry argument for the reduction of possible interaction terms does not hold anymore and as such one must use the local regularization carefully [75]. E.g., the contact interaction in Eq. (2.17) does not act on P waves due to the antisymmetry of P waves but a smeared contact interaction according to Eq. (3.1) contributes to the P waves. Hence, the smearing operators should be implemented such that it only projects on S waves.

Beside the contact interaction, we have also long-range interactions at leading order. Before the modern formulation of an effective field theory, one already assumed the one-pion exchange as a central part of the theory going back to Yukawa [76]. Obviously, a cutoff is necessary due to the singular structure at the origin which was difficult to explain before the full understanding of effective field theories. An early work on the one-pion exchange, the cutoff dependence and deuteron observables can be found in [77]. We consider the one-pion-exchange potential in its continuum form,

$$V_{\mathrm{OPEP}}(\vec{q}) = -\frac{g_A^2}{4F_\pi^2}\frac{\vec{\sigma}_1\cdot\vec{q}\vec{\sigma}_2\cdot\vec{q}}{\vec{q}^2+M_\pi^2}\vec{\tau}_1\cdot\vec{\tau}_2. \tag{3.4}$$

For example, projected on the ${}^1S_0$ channel in position space, the potential reads

$$V_{\mathrm{OPEP}}^{{}^1S_0}(r) = \frac{M_\pi^2}{12\pi}\frac{g_A^2}{4F_\pi^2}(-3)\left[\frac{\exp(-M_\pi r)}{r} - \frac{4\pi}{3}\delta(\vec{r})\right]. \tag{3.5}$$

Here, $r = |\vec{r}|$ is the radial distance between the two particles. Obviously, such a potential is divergent at the origin making a regulator necessary. Moreover, the short-range physics should be completely described by short-range terms and their respective low-energy coupling constants constructed according to the rules of EFT. A standard smearing in momentum space would produce oscillations in the potential for very large momenta. These oscillations can be avoided by more complicated momentum space smearing functions [78] or by using position space regulators. Such a regulator is

$$f_{\mathrm{long-range}}(r) = \left[1-\exp\left(-\frac{r^2}{R^2}\right)\right]^n, \tag{3.6}$$

where R is a coordinate-cutoff parameter reflecting the distinction between short- and long-range physics. The exponent n should be chosen such that the singularity vanishes and the fits are robust. In Fig. 3.1 we show a continuum-regularized potential for $R = 0.8, \ldots, 1.2$ fm and $n = 6$ in the ${}^1S_0$ channel. Such a scheme regularizes the OPEP to zero in the origin, and hence, the whole interaction is described by the short-range potential terms. On the lattice we firstly have an inherent natural hard regulator in momentum space by the lattice spacing as $\Lambda = \pi/a$ which is chosen as $a = 1.97$ fm, $a = 1.32$ fm and $a = 0.98$ fm in this subsection. Secondly, the discretization scheme itself may serve as a regulator as the momentum can be discretized in different schemes. We show the OPEP for for three different schemes. The first scheme uses a very basic discretization using trigonometric functions in momentum space. In the second scheme we improve it by using a superposition of trigonometric functions whereby in the last scheme we use the exact momentum on the lattice. For example, the lattice momentum component $\nu(p_l)$ in the numerator is discretized as $\nu(p_l) = \sin(p_l)$, $\nu(p_l) = 4/3\sin(p_l) - 1/6\sin(2p_l)$, and $\nu(p_l) = \mathrm{mod}(p_l+\pi, 2\pi) - \pi$,

respectively. As we see in Fig. 3.1 the continuum result and the continuum-regularized one are both attractive albeit the latter one vanishes for small lattice spacings. This is in line with effective field theory, where all short-range physics is absorbed in contact interaction terms. All lattice realizations show a very good agreement for distances larger than 3.5 fm, while the trigonometric ones show a repulsive behavior between 0 fm and 3 fm. This is partially compensated by some contributions which are very negative, e.g. at a distance of 2 fm for a lattice spacing of 0.98 fm. The exact discretization results are in a very good agreement with the continuum calculation. We see of course that for lattice spacings smaller than 1.0 fm, the exact discretization solution is far off from the continuum-regularized solution. This means that we can use the one-pion-exchange potential without extra regulator only in systems with lattice spacings larger than ∼1 fm. Otherwise, the contact interaction contributions become unnaturally large, and may not be able to compensate the OPE contribution.

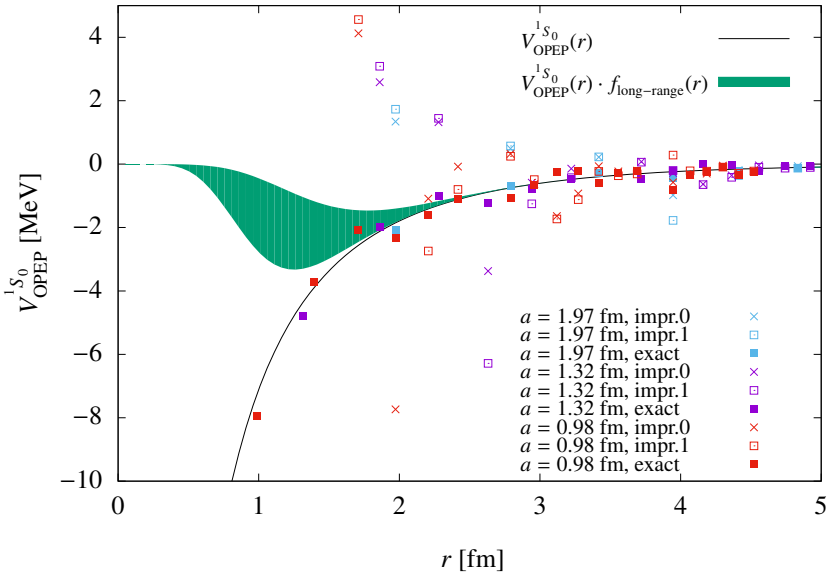

Figure 3.1: $^1S_0$ one-pion-exchange potential for various lattice discretization schemes and continuum solutions with and without position space regularization.

3.2 The reduced symmetry of SO(3, $\mathbb{Z}$)

As argued in Subsec. 2.2.1, the continuum SO(3) symmetry has an infinite number of irreducible representations and each irreducible representation is identified with the angular momentum j. This makes the identification straightforward, as each partial wave is directly linked to an irreducible representation with quantum number j. In fact, this is not possible anymore in a cubic finite volume. Due to the cubic symmetry, rotations are only allowed for a discrete and finite number of values, namely multiplicities of $\pi/2$. E. g., the $\pi/2$ rotation around the z-axes is given by the operator,

$$R_{\hat{z}}\left(\frac{\pi}{2}\right) = \exp\left(-i\frac{\pi}{2}j_z\right). \tag{3.7}$$

Rotations around the x- and y-axes are defined accordingly with respect to j_x, j_y. From Eq. (3.7) it is clear that also the quantum number j_z is not a good quantum number anymore, but only j_z modulo 4.

The reduced symmetry group is SO(3, $\mathbb{Z}$), which is a finite group consisting of the representations A_1, T_1, E, T_2, and A_2 [79]. The properties of the representation are summarized in Tab. 3.1.

Rep	dimensionality	j_z	Example
A_1	1	0 mod 4	$Y_{0,0}$
T_1	3	0,1,3 mod 4	$\{Y_{1,1}, Y_{1,0}, Y_{1,-1}\}$
E	2	0,2 mod 4	$\{Y_{2,0}, \frac{Y_{2,-2}+Y_{2,2}}{\sqrt{2}}\}$
T_2	3	1,2,3 mod 4	$\{Y_{2,1}, \frac{Y_{2,-2}+Y_{2,2}}{\sqrt{2}}, Y_{2,-1}\}$
A_2	1	2 mod 4	$\frac{Y_{3,2}-Y_{3,-2}}{\sqrt{2}}$

Table 3.1: Spherical harmonics for various representations [79].

j	irrep
0	A_1
1	T_1
2	$E \oplus T_2$
3	$A_2 \oplus T_1 \oplus T_2$
4	$A_1 \oplus E \oplus T_1 \oplus T_2$
5	$E \oplus T_1 \oplus T_1 \oplus T_2$
6	$A_1 \oplus A_2 \oplus E \oplus T_1 \oplus T_2 \oplus T_2$

Table 3.2: Irreducible representations for angular momentum $j \leq 6$ [79].

The mapping from SO(3) irreducible representations according to their angular momentum j to the irreducible representations of SO(3, $\mathbb{Z}$) is shown in Tab. 3.2. There is a one-to-one mapping for systems with angular momenta zero and one. The situation becomes difficult by including higher angular momenta and as such higher partial waves. Firstly, the partial waves begin to decompose into parts belonging to different representations. Hence, a formalism must be used that puts together the different pieces of different representations to restore the rotational invariant state where the angular momentum is a good quantum number, see for example in [80, 81]. Additionaly, a representation like the T_1 exist for $j = 1$ and $j = 3$, linking the coupled channels ${}^3S_1 - {}^3D_1$ and ${}^3D_3 - {}^3G_3$. Such a mixing is unphysical and should be removed from the data. This effect has been investigated in Refs. [82, 83] and it is removed by adding all possible rotational symmetry breaking operators in the theory.

3.3 Bound states on the lattice

The identification of bound states in the energy spectrum of a lattice calculation is quite important for the determination of deuteron, triton and helium properties as well as any other description of nuclei in the framework of NLEFT. Instead of neglecting finite-volume effects by using a box with large enough volume, one could also use these effects to extrapolate to the infinite volume. Therefore, it is necessary to know the finite-volume behaviour of the bound state.

Firstly, we rederive Lüscher's finite volume formula for non-relativistic two-body bound states [84]. The original approach takes into account only spinless pointlike particles for angular momentum $l = 0$.

Initial point is the infinite volume solution for a local and finite-range potential,

$$V(\vec{r}) = 0 \qquad \forall \left|\vec{r}\right| > R, \tag{3.8}$$

with R being the range of the potential. Then the Schrödinger equation with bound state solution $E_B > 0$ is

$$\left[\frac{1}{2\mu}\Delta_r + V(\vec{r})\right]\Psi_B(\vec{r}) = -E_B\Psi_B(\vec{r}), \tag{3.9}$$

where Ψ_B is the infinite-volume bound state solution for S wave scattering. In the asymptotic region with vanishing potential, the solution is given by Eq. (2.36) for $l = 0$ but with imaginary momentum leading to the solution,

$$\Psi_B(\vec{r}) = \frac{\mathcal{A}_\kappa}{\sqrt{4\pi}}\frac{\exp(-\kappa r)}{r}, \tag{3.10}$$

with $r = |\vec{r}|$. The respective binding momentum is $\kappa = \sqrt{2\mu E_B}$ and $\mathcal{A}_\kappa$ is the normalization constant. In the finite volume the situation is different as it is generally only defined in a box of size $L \times L \times L$ with periodic boundary conditions. This condition is used to extend the box to the whole space,

$$V_L(\vec{r}) = \sum_{\vec{n}} V(\vec{r} + \vec{n}L). \tag{3.11}$$

Correspondingly, the finite volume is periodically extended to the infinite volume and the new Schrödinger equation reads

$$H_L\Psi = (H_{\text{kin}} + V_L)\Psi. \tag{3.12}$$

We can define a periodic wave function using the infinte volume solution Ψ_B,

$$\Psi_0(\vec{z}) = \sum_{\vec{n}\in\mathbb{Z}} \Psi_B(|\vec{z} + \vec{n}L|), \qquad \vec{z} = \vec{x} - \vec{y}. \tag{3.13}$$

Now the new wave function almost fulfills the respective Schrödinger equation up to a correction term,

$$H_L\Psi_0 = -E_B\Psi_0 + \sum_{\vec{n}\neq\vec{n}'} V(\vec{z} + \vec{n}L)\,\Psi_B\left(|\vec{z} + \vec{n}'L|\right). \tag{3.14}$$

Requiring that the box is large enough such that the asymptotic wave function is applicable at the edge of the finite box, the correction term is suppressed by $O[\exp(-\kappa L)]$ due to Eq. (3.10). Hence, we can assume that $\Psi \approx \Psi_0$ as corrections are negligible once the volume is chosen large enough. Finally, the binding energy correction can be calculated by

$$\begin{aligned}
\Delta E_B = E_B - E_L &= -\left(\langle\Psi_B| H |\Psi_B\rangle - \langle\Psi| H_L |\Psi\rangle\right) \\
&= E_B - \langle\Psi_0| H |\Psi_0\rangle \\
&= \sum_{\vec{n}\neq\vec{n}'} \int \mathrm{d}\vec{z}\,\Psi_B(|\vec{z} + \vec{n}L|)\,V(\vec{z} + \vec{n}L)\,\Psi_B\left(|\vec{z} + \vec{n}'L|\right) \\
&= -24\pi|A|^2\frac{\exp(-\kappa L)}{mL} + O\left[\exp\left(-\sqrt{2}\kappa L\right)\right].
\end{aligned} \tag{3.15}$$

Clearly, mostly S wave bound states emerge in nuclear physics, but P wave bound states can be created in atomic physics as well. Hence, a generalization of the bound state energy shift formula may be useful

and it was derived in [85, 86].

As the computational power arises, three-body finite-volume effects are now an actual field of research. Certainly, this is far more difficult than the two-body problem as the most general three-body bound state is in between a 2+1 state, where a very deeply bound dimer exists and a shallow 1+1+1 bound state, which is restricted to the unitary limit case. Finite-volume formulas and discussions can be found in [87–92]. The explicit formula will be given in the respective chapter.

3.4 Scattering on the lattice

3.4.1 Lüscher's effective range expansion in the finite volume

Similar to the finite volume effects of bound states, we can have a look on finite volume calculations of the phase shift and the effective range expansion. In [93, 94], a finite volume effective range expansion was derived,

$$q \cot \delta (q) = \frac{1}{\pi L} S (\eta) , \qquad \eta = \left(\frac{Lq}{2\pi}\right)^2 , \tag{3.16}$$

and is related to Eq. (2.44) in the infinite volume. Here, $q = |\vec{q}|$ is the relative momentum linked to the measured finite-volume eigenenergy via $E_L = q^2/2\mu$ and $S(\eta)$ is the three-dimensional ζ-function,

$$S (\eta) = \lim_{\Lambda \to \infty} \left[\sum_{\vec{n}} \frac{\Theta\left(\Lambda^2 - \vec{n}^2\right)}{\vec{n}^2 - \eta} - 4\pi\Lambda \right]. \tag{3.17}$$

It is approximated for small η by

$$S (\eta) = -\frac{1}{\eta} + S_0 + S_1 \eta^1 + S_2 \eta^2 + S_3 \eta^3 + \dots \quad , \tag{3.18}$$

with

$$S_0 = \lim_{\Lambda -> \infty} \left[\sum_{\vec{n}} \frac{\Theta\left(\Lambda^2 - \vec{n}^2\right)}{\vec{n}^2} - 4\pi\Lambda \right], \tag{3.19}$$

$$S_j = \sum_{\vec{n} \neq \vec{0}} \frac{1}{\left(\vec{n}^2\right)^{j+1}} \qquad , j \geq 1. \tag{3.20}$$

The first coefficients were summarized in [32] and denote

$$\begin{aligned} &S_0 = -8.913631, \quad S_1 = 16.532288, \quad S_2 = 8.401924, \quad S_3 = 6.945808, \\ &S_4 = 6.426119, \quad S_5 = 6.202149, \quad S_6 = 6.098184, \quad S_7 = 6.048263. \end{aligned} \tag{3.21}$$

3.4.2 Spherical wall and radial projection

Lüscher's effective range expansion is the appropriate method for low energy and zero angular momentum. Although nowadays there are extensions to higher partial waves and one could also improve the predictability range by including higher terms in the effective range expansion, we choose another approach to describe two-particle scattering in a box. By imposing a spherical wall as a boundary condition at $r \approx R_W$ in the cubic box, one can almost enforce spherical symmetry on the system and the solutions will be standing waves which also cover a large range of momenta. As we have a localized

interaction, in the area between the interaction and the spherical wall the solution can be decomposed into spherical harmonics using Eqs. (2.40) and (2.41),

$$\left[\cos\delta_l j_l(qr) - \sin\delta_l n_l(qr)\right] Y_{l,l_z}(\theta,\phi)\,. \tag{3.22}$$

Due to the infinite spherical wall, the wave function must vanish for $r = R_\mathrm{W}$ leading to the condition,

$$\cos(\delta_l)\, j_l(qR_\mathrm{W}) = \sin(\delta_l)\, n_l(qR_\mathrm{W})\,, \tag{3.23}$$

which defines the phase shift,

$$\delta_l = \arctan\left[\frac{j_l(qR_\mathrm{W})}{n_l(qR_\mathrm{W})}\right]. \tag{3.24}$$

This equation is exact in the continuum. Nevertheless, there is some ambiguity due to the finite distance between lattice points making it necessary to fine tune R_W for each solution.

The upper equation is only valid for uncoupled channels like in the case of spin zero partial waves. If there is a system of coupled channels, one has to include both channels simultaneously. A detailed derivation of the expressions can be found in [61] and we briefly summarize the results in the following. As shown in Subsec. 2.2.2 we can rewrite the wave function in terms of an incoming and outgoing wave function as well as the S-matrix. Imposing the spherical wall gives rise to two standing waves Ψ^I and Ψ^{II} which are independent and which have the form

$$\Psi^{I/II} = \frac{1}{k^{I/II} r}\begin{bmatrix} A^{I/II}_{j-1}\sin\left(k^{I/II}r - \frac{j-1}{2}\pi + \Delta^{I/II}_{j-1}\right) \\ A^{I/II}_{j+1}\sin\left(k^{I/II}r - \frac{j+1}{2}\pi + \Delta^{I/II}_{j+1}\right)\end{bmatrix}, \tag{3.25}$$

with energies $E^{I/II} = \vec{q}^{\,(I/II)2}/(2\mu)$. The hard wall boundary condition is imposed by

$$-\Delta_{j\pm1} = qR_\mathrm{W} - \frac{j\pm1}{2}\pi. \tag{3.26}$$

This is linked to the mixing angle by

$$\tan\left(-\Delta^{I/II}_{j-1} + \delta_{j-1}\right)\tan\left(-\Delta^{I/II}_{j+1} + \delta_{j+1}\right) = \tan^2\left(\epsilon_j\right), \tag{3.27}$$

$$A^{I/II}_{j-1}\tan\left(\epsilon_j\right) = -A^{I/II}_{j+1}\frac{\sin\left(-\Delta^{I/II}_{j+1} + \delta_{j+1}\right)}{\sin\left(-\Delta^{I/II}_{j-1} + \delta_{j-1}\right)}. \tag{3.28}$$

For small ϵ_j and for two solutions with $q^I \approx q^{II}$ the former equations can be simplified and the mixing angle is given as

$$\epsilon_j = \frac{A^I_{j+1}}{A^I_{j-1}}\sin\left(\delta_{j+1} - \delta_{j-1}\right), \tag{3.29}$$

where the amplitudes $A^I_{j\pm1}$ are calculated by the overlap of the standing wave and the corresponding spherical harmonic close to the spherical wall.

This method only uses the binding energy as input for the phase shift calculation and some approximations are necessary particularly for the calculation of coupled channel phase shifts and mixing angles. In [83] a new method was proposed. Generally speaking, one takes advantage of the wave function itself as input and hence, one reduces the inevitable simplifications particularly for the mixing angle.

In order to calculate phase shifts with respect to their partial wave decomposition efficiently, we reverse

Nr.	1	2	3	4	5	...
$\lvert\vec{r}\rvert$	0	$\sqrt{2}$	$\sqrt{3}$	2	$\sqrt{5}$	...
$\#_{\lvert\vec{r}\rvert}$	1	6	12	8	6	...

Table 3.3: Radial projection and binning for the first radii. The second line gives the value of the radii and the third line gives the counting of points with the respective radius.

the ordering. While in the standard approach, one first calculates the spectrum and then assigns each solution to a partial wave, one could also first project the system onto the respective (coupled) partial wave and then solve the system. As the projection onto the partial waves only keeps the radial part of the wave function, the system is much smaller than before, and the phase shift is directly fitted to the radial wave function. In the following we give details in the case of uncoupled as well as coupled channels.

The change from a three-dimensional basis to a radial one is made by binning all points with the same radius R and total angular momentum as well as orbital angular momentum and spin according to the partial wave. The respective projection operator reads

$$\left|R, j, j_z, l, s\right\rangle = \sum_{|\vec{R}|=R, s_z, l_z} C^{j,j_z}_{l,l_z,s,s_z} Y_{l,l_z}\left(\hat{R}\right)\left|\vec{R}\right\rangle \otimes \left|s_z\right\rangle, \tag{3.30}$$

whereas C^{j,j_z}_{l,l_z,s,s_z} are the usual Clebsch-Gordan coefficients. While the radial norm in the continuum would be just proportional to r^2, one has to count the number of points for every possible radius and construct the norm according to the number of points. The first number of points per radius are shown in Tab. 3.3. The norm respecting the number of points per radius as well as the quantum number due to the partial waves reads

$$\mathcal{N}^{j,j_z}_{l,s}(R) = \left\langle R, j, j_z, l, s \mid R, j, j_z, l, s\right\rangle. \tag{3.31}$$

The projection operator and the norm correction are applied to all operators $O\left(\vec{R}\right)$ resulting in,

$$O(R)^{j,j_z}_{l,s} = \left[\mathcal{N}^{j,j_z}_{l,s}(R)\right]^{-\frac{1}{2}} \left\langle R, j, j_z, l, s\right| O\left(\vec{R}\right)\left|R, j, j_z, l, s\right\rangle \left[\mathcal{N}^{j,j_z}_{l,s}(R)\right]^{-\frac{1}{2}}. \tag{3.32}$$

After applying the projection operator to all operators, the eigensystem is solved efficiently. The eigenvalue corresponds to the energy of the system, and the eigenfunction is identified with a superposition of Bessel functions outside of the interaction region for the specific partial wave of interest. Instead of using Eqs. (2.40) and (3.24), we rewrite the respective function in terms of the Hankel functions $h^{\pm}_l$, which are a linear combination of the former ones, and the constants A and B,

$$\psi_l(r) \propto A h^-_l(pr) + B h^+_l(pr). \tag{3.33}$$

The explicit form of the Hankel functions are moved to App. A. These functions are identified as incoming and outgoing wave functions linked to the S-matrix in Eq. (2.32). Then the phase shift is calculated from

$$B = S_l A = \exp(2i\delta_l) A. \tag{3.34}$$

The procedure is shown schematically in Figs. 3.2 and 3.3. Firstly, a spherical wall is imposed at R_W, which generates standing waves. Secondly, all nodes with the same radius are binned together. The interaction region is close to the origin in region I, while we calculate the phase shift from the wave

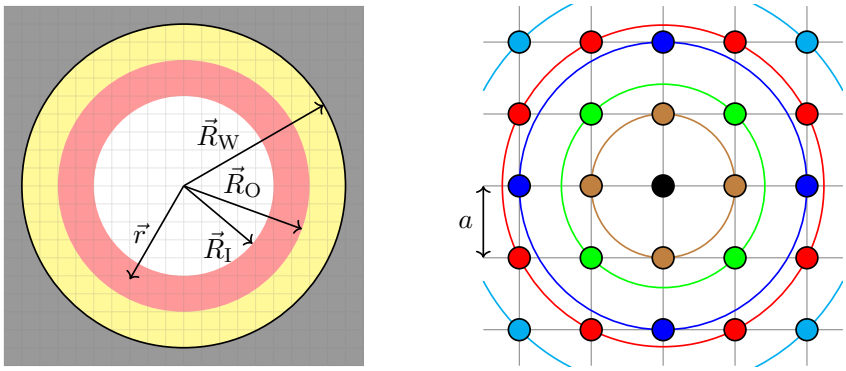

Figure 3.2: Schematic sketch of the radial wall and spherical projection method. Left figure: The spherical wall is introduced at $|\vec{R}_W|$. In the case of radial projection, the wave function is measured at all lattice points $\vec{r}$ with $|\vec{R}_I| < |\vec{r}| < |\vec{R}_O|$. Right figure: All lattice nodes and operators with the same radius are merged with respect to their partial wave spherical harmonic [83].

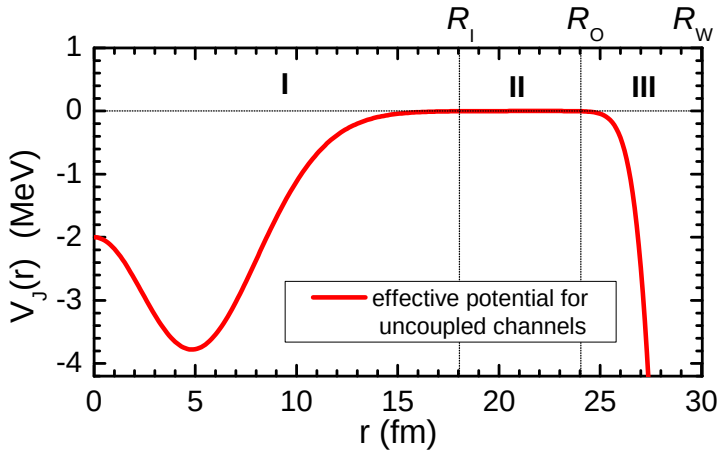

Figure 3.3: Sketch of an example potential in spherical projection [83].

function in region II, which is bordered by R_I and R_O. Though this approach is straightforward for uncoupled channels, it does not work in the coupled-channel system, which relates partial waves with $j = l \pm 1$. This means that the coefficients of Eqs. (3.33) and (3.34) are vector like, $A = (A_{j-1}, A_{j+1})$ and $B = (B_{j-1}, B_{j+1})$. Correspondingly, one needs two independent solutions (Ψ_{j-1}, Ψ_{j+1}) to determine phase shifts and mixing angles. In the previous case this was achieved by using different solutions which have approximately the same energy and neglect this difference. But this method is not applicable, because the solutions of Eq. (2.31) have exactly the same energy and they are dependent on each other. By introducing the Hermitian but time-reversal symmetry breaking auxiliary potential,

$$V \to V + \begin{pmatrix} 0 & iV_{\text{aux}} \\ -iV_{\text{aux}} & 0 \end{pmatrix}, \tag{3.35}$$

in region III of Fig. 3.2, the solutions decouple to ψ and ψ^* with the same energy and the conjugate equation for the S-matrix determination reads

$$A^* = S\,B^*. \tag{3.36}$$

Rewriting the S-matrix in terms of A, B gives

$$S = \begin{bmatrix} B & A^* \end{bmatrix} \begin{bmatrix} A & B^* \end{bmatrix}^{-1} . \tag{3.37}$$

where S is defined according to the Stapp parametrization of Eq. (2.53). Then again, the phase shifts as well as the mixing angles are fitted to Eq. (3.37).

In this thesis we calculate the nucleon-nucleon phase shift and mixing angle in the following manner. At LO, we use the spherical projection method for the determination of phase shifts and mixing angles while we use only the energy information for the perturbative inclusion of NLO and N2LO potentials in the calculation of the phase shift. As we cannot solve the mixing angle perturbatively for higher orders, we use again the spherical projection for these calculations.

3.5 Exact methods

As long as we consider only systems with a few particles, we can use the Lanczos/ Arnoldi algorithm [95, 96] for sparse matrices to solve the eigenvalue problem. Afterward, we have the energy and the wave function of the system and use this information for the calculation of binding energies and phase shifts. The Lanczos algorithm works as the following.

A general eigenvalue problem reads

$$A \cdot v = \lambda \cdot v, \tag{3.38}$$

where A is a $n \times n$ matrix, λ is the eigenvalue and v is the eigenvector which can be rewritten in the basis of the power-iterated subspace,

$$\left\{ q, Aq, A^2 q, A^3 q, \ldots \right\}, \tag{3.39}$$

where q is an arbitrary starting vector. Hence, we could use a finite number of m vectors based on Eq. (3.39) to orthogonally transform the matrix A into a Hessenberg matrix H_m, from which the eigenvalues and -vectors are calculated faster than for a general matrix. Admittedly, the aforementioned arguments of Eq. (3.39) do not have to be orthogonal. After orthogonalization, the basis is given by $p_1, \ldots, p_m$ and applied to the general matrix A, we get the $m \times m$ Hessenberg matrix, where all entries below the first subdiagonal are equal to zero. It is of the form

$$H_m = \begin{pmatrix} h_{1,1} & h_{1,2} & \cdots & h_{1,m} \\ h_{2,1} & h_{22} & \cdots & h_{2,m} \\ 0 & h_{3,2} & \cdots & h_{3,m} \\ 0 & 0 & \cdots & h_{4,m} \\ & & \cdots & \\ & & \cdots & h_{m,m} \end{pmatrix}, \tag{3.40}$$

and it is an similarity transformation of the original matrix A in the first m arguments. In the case of a real symmetric matrix A, Eq. (3.40) reduces to a tridiagonal matrix which can be evaluated even faster. As we work with finite m, the eigenvectors and -values are only an approximation of the exact solution, making it necessary to iterate the procedure until the desired precision is reached. Generally, we only have to perform a matrix-vector multiplication and we have to store the vectors $p_1, \ldots, p_m$ as well as the matrix H_m. This is particularly efficient for very sparse matrices, where most of the entries are zero and as such do not contribute to the calculation. Using a large enough basis and enough iterations it is also possible to calculate more than one eigenvalue which is particularly important for the calculation of phase shifts where one needs eigenvalues corresponding to a large range of energy.

3.6 The auxiliary field partition function

Generally, we use three different methods to extract physical observables. While we use the Hamiltonian formalism and the transfer matrix formalism for the exact calculations, we use a Grassmann path integral formalism with auxiliary fields in the case of Monte Carlo simulations. In the following we will show that all formalisms are equivalent up to higher order lattice artifacts. In the current and the subsequent section we follow [97, 98]. For the proof we consider a system of two fermions with spin ↑ and ↓ and a simple contact interaction $\propto C$. On the one hand, the corresponding path integral reads

$$Z = \int \mathrm{D}c\, \mathrm{D}c^* \exp\left[-S\left(c, c^*\right)\right], \tag{3.41}$$

with the action

$$S\left(c, c^*\right) = S_{\text{free}}\left(c, c^*\right) + C\alpha_t \sum_{\vec{n}, n_t} c_\uparrow^*\left(\vec{n}, n_t\right) c_\uparrow\left(\vec{n}, n_t\right) c_\downarrow^*\left(\vec{n}, n_t\right) c_\downarrow\left(\vec{n}, n_t\right). \tag{3.42}$$

Here, α_t is the ratio of the spatial and temporal lattice spacings, $\alpha_t = a/a_t$. The free part reads

$$\begin{aligned} S_{\text{free}}\left(c, c^*\right) = \sum_{\vec{n}, n_t, i=\uparrow,\downarrow} \Bigg\{ & \left[c_i^*\left(\vec{n}, n_t\right) c_i\left(\vec{n}, n_t + 1\right) - (1 - 6h) c_i^*\left(\vec{n}, n_t\right) c_i\left(\vec{n}, n_t\right)\right] \\ & + \sum_{\hat{l}=1,2,3} \left[c_i^*\left(\vec{n}, n_t\right) c_i\left(\vec{n} + \hat{l}, n_t\right) + c_i^*\left(\vec{n}, n_t\right) c_i\left(\vec{n} - \hat{l}, n_t\right)\right] \Bigg\}, \end{aligned} \tag{3.43}$$

with $h = \alpha_t/(2m)$. Eq. (3.43) represents the most simple discretization of the free action. On the other hand, the discrete Hamiltonian reads

$$\begin{aligned} H = & \sum_{\vec{n}, i=\uparrow,\downarrow} \left\{ \frac{3}{m} a_i^\dagger\left(\vec{n}\right) a_i\left(\vec{n}\right) - \frac{1}{2m} \sum_{\hat{l}=1,2,3} \left[a_i^\dagger\left(\vec{n}\right) a_i\left(\vec{n} + \hat{l}\right) + a_i^\dagger\left(\vec{n}\right) a_i\left(\vec{n} - \hat{l}\right)\right] \right\} \\ & + C \sum_{\vec{n}} a_\uparrow^\dagger(\vec{n}) a_\uparrow(\vec{n}) a_\downarrow^\dagger(\vec{n}) a_\downarrow(\vec{n}). \end{aligned} \tag{3.44}$$

Using the general properties of Grassman variables and anticommutation relations (see App. A.3 for details), one can proof the following identity

$$\mathrm{Tr}\left[: f\left(a^\dagger, a\right) :\right] = \int \mathrm{d}c\,(0)\, \mathrm{d}c^*\,(0) \exp\left\{c^*\,(0)\left[c\,(0) - c\,(1)\right]\right\} f\left[c^*\,(0), c\,(0)\right], \tag{3.45}$$

where the antiperiodic boundary condition in time direction is realized by $c(1) = -c(0)$.

The previous equation shows the connection only for one time slice, but it is extendable to the general identity,

$$\begin{aligned} & \mathrm{Tr}\left\{: F_{L_t-1}\left[a_{i'}^\dagger\left(\vec{n}'\right), a_i\left(\vec{n}\right)\right] : \ \ldots : F_0\left[a_{i'}^\dagger\left(\vec{n}'\right), a_i\left(\vec{n}\right)\right] : \right\} \\ & = \int \mathrm{D}c\, \mathrm{D}c^* \exp\left\{ \sum_{n_t=0}^{L_t-1} \sum_{\vec{n}, i} \left[c_i^*\left(\vec{n}, n_t\right) c_i\left(\vec{n}, n_t\right) - c_i\left(\vec{n}, n_t + 1\right)\right] \right\} \prod_{n_t=0}^{L_t-1} F_{n_t}\left[c_{i'}^*\left(\vec{n}', n_t\right), c_i\left(\vec{n}, n_t\right)\right]. \end{aligned} \tag{3.46}$$

Now the antiperiodic boundary condition reads $c_i(\vec{n}, L_t) = -c_i(\vec{n}, 0)$. Identifying $F_j[a_{i'}^\dagger(\vec{n}'), a_i(\vec{n})]$ with the transfer matrix

$$M =: \exp\left(-\alpha_t H\right) : , \tag{3.47}$$

and the terms in the second line of Eq. (3.46) with the action of Eq. (3.42) we have shown the equality between path integral and transfer matrix partition function,

$$Z = \mathrm{Tr}\left(M^{L_t}\right). \tag{3.48}$$

Using a Gaussian quadratic and completing the square, the path integral is rewritten as

$$Z = \prod_{\vec{n},n_t}\left[\int \mathrm{d}_A s\left(\vec{n}, n_t\right)\right] \int \mathrm{D}c\, \mathrm{D}c^* \exp\left[-S_A\left(c, c^*, s\right)\right], \tag{3.49}$$

with the new action including the auxiliary field,

$$S_A\left(c, c^*, s\right) = S_{\text{free}}\left(c, c^*\right) - \sum_{\vec{n},n_t} A\left[s\left(\vec{n}, n_t\right)\right] \rho\left(\vec{n}, n_t\right). \tag{3.50}$$

The auxiliary field integral reads [99, 100]

$$\int \mathrm{d}_A s\left(\vec{n}, n_t\right) = \frac{1}{2\pi} \int_{-\infty}^{\infty} \mathrm{d}s\left(\vec{n}, n_t\right) \exp\left[-\frac{1}{2} s^2\left(\vec{n}, n_t\right)\right], \tag{3.51}$$

$$A\left[s\left(\vec{n}, n_t\right)\right] = \sqrt{-C\alpha_t}\, s\left(\vec{n}, n_t\right). \tag{3.52}$$

The above written form is also known as Hubbard-Stratonovich transformation. In general, there are plenty of alternative forms of Eqs (3.51) and (3.52) for the auxiliary field which must fulfill the following equations,

$$\int \mathrm{d}_A s\left(\vec{n}, n_t\right) = 1, \tag{3.53}$$

$$\int \mathrm{d}_A s\left(\vec{n}, n_t\right)\, A\left[s\left(\vec{n}, n_t\right)\right] = 0, \tag{3.54}$$

$$-C\alpha_t = \int \mathrm{d}_A s\left(\vec{n}, n_t\right)\, A^2\left[s\left(\vec{n}, n_t\right)\right]. \tag{3.55}$$

Some of them are investigated in [101]. Eqs. (3.41) and (3.49) are equivalent but the two-body interaction is removed making the explicit calculation faster as the theory only consists of one-nucleon states which do not interact with each other but only via an auxiliary field. After showing the equivalence of the Hamiltonian transfer matrix method and the path integral with and without auxiliary field, the appropriate method depends on the problem. For many-body problems the only feasible way is to choose the path integral with auxiliary field formulation.

This method is extended to all LO smeared contact interaction as well as the one-pion exchange which we will be included in the subsequent calculations as well. As we already see, each operator requires an extra auxiliary field making it computationally expensive to include NLO operators in the partition function too.

3.7 Hybrid Monte Carlo algorithm for Nuclear Lattice Effective Field Theory

While there are a lot of different algorithms to calculate Eq. (3.41), we choose the Hybrid Monte Carlo (HMC) algorithm in this thesis [102]. In this algorithm we update the whole field and auxiliary field configuration at the same time making it very efficient and exact. In the following we give a detailed description of the method. Starting point is the path integral with auxiliary fields according to Eq. (3.49), where the path integral over the Grassmann fields is substituted by the transfer matrix formulation,

$$Z(t) = \int \mathrm{D}\pi_I \, \mathrm{D}s \, \mathrm{D}s_S \, \mathrm{D}s_I \, \mathrm{D}s_{SI} \, \exp\left[-S_{\pi\pi} - S_{ss}\right] \langle \Psi | \, M^{L_t}\left(\pi_I, s, s_S, s_I, s_{SI}\right) | \Psi \rangle \,. \tag{3.56}$$

Here, $|\Psi\rangle$ is the trial wave function and $M^{(n_t)}(\pi_I, s, s_I)$ is the transfer matrix including all auxiliary field-nucleon interactions,

$$\begin{aligned} M^{(n_t)}\left(\pi_I, s, s_S, \; s_I, s_{SI}\right) =: \; \exp\Bigg[& -H_{\text{free}}\alpha_t - \frac{g_A \alpha_t}{2F_\pi} \sum_{S,I} \Delta_S \pi_I\left(\vec{n}_s, n_t\right) \rho_{S,I}\left(\vec{n}_s\right) \\ & + \sqrt{-c_{00}\alpha_t} \sum_{\vec{n}} s\left(\vec{n}, \vec{n}\right) \rho\left(\vec{n}\right) + \sqrt{-c_{ss}\alpha_t} \sum_{S} \sum_{\vec{n}} s_S\left(\vec{n}, n_t\right) \rho_S\left(\vec{n}\right) \\ & + \sqrt{-c_{ii}\alpha_t} \sum_{I} \sum_{\vec{n}} s_I\left(\vec{n}, n_t\right) \rho_I\left(\vec{n}\right) + \sqrt{-c_{si}\alpha_t} \sum_{S,I} \sum_{\vec{n}} s_{SI}\left(\vec{n}, n_t\right) \rho_{SI}\left(\vec{n}\right) \Bigg] : \,. \end{aligned} \tag{3.57}$$

The free Hamiltonian is used in the discretized version of the upper line of Eq. (3.44), while the density operators are defined in App. B. The auxiliary fields s, s_S, s_I and s_{SI} correspond to the respective contact interaction. The pion and auxiliary field actions read

$$S_{\pi\pi} = \alpha_t \left(\frac{m_\pi^2}{2} + 3\right) \sum_{I} \sum_{\vec{n}} \pi_I\left(\vec{n}\right) \pi_I\left(\vec{n}\right) - \alpha_t \sum_{I} \sum_{\vec{n},\hat{l}} \pi_I\left(\vec{n}\right) \pi_I\left(\vec{n} + \hat{l}\right), \tag{3.58}$$

$$\begin{aligned} S_{ss} = & \frac{1}{2} \sum_{\vec{n},\vec{n}',n_t} s\left(\vec{n}, n_t\right) f^{-1}\left(\vec{n} - \vec{n}'\right) s\left(\vec{n}'\right) + \frac{1}{2} \sum_{\vec{n},\vec{n}',n_t,S} s_S\left(\vec{n}, n_t\right) f^{-1}\left(\vec{n} - \vec{n}'\right) s_S\left(\vec{n}'\right) \\ & + \frac{1}{2} \sum_{\vec{n},\vec{n}',n_t,I} s_I\left(\vec{n}, n_t\right) f^{-1}\left(\vec{n} - \vec{n}'\right) s_I\left(\vec{n}'\right) + \frac{1}{2} \sum_{\vec{n},\vec{n}',n_t,S,I} s_{SI}\left(\vec{n}, n_t\right) f^{-1}\left(\vec{n} - \vec{n}'\right) s_{SI}\left(\vec{n}'\right), \end{aligned} \tag{3.59}$$

with $f^{-1}(\vec{n} - \vec{n}')$ is the inverse smearing function,

$$f^{-1}\left(\vec{n} - \vec{n}'\right) = \frac{1}{L^3} \sum_{\vec{q}} \frac{1}{f\left(\vec{q}\right)} \exp\left[-i\vec{q}\left(\vec{n} - \vec{n}'\right)\right]. \tag{3.60}$$

A natural choice for the trial wave function is an antiymmetric combination of plane single-nucleon wave functions, $|\Psi^{\text{free}}\rangle$. As a time evolution of such a state through the complete LO transfer matrix is too expensive, we split the calculation into two parts. Firstly, we evolve this configuration through an SU(4) symmetric Hamiltonian L_{t_0} times. Such a simplified Hamiltonian does not suffer from the sign problem and it is already a good approximation to the full Hamiltonian [33, 103, 104]. Then the trial

wave function reads

$$|\Psi\rangle = \prod_{n_t=1}^{L_{t_o}} : \exp\left[-H_{\text{free}}\alpha_t - \frac{1}{2} \sum_{\vec{n},\vec{n}',n_t} s_{\text{SU(4)}}(\vec{n},n_t) f^{-1}_{\text{SU(4)}}\left(\vec{n}-\vec{n}'\right) s_{\text{SU(4)}}\left(\vec{n}',n_t\right) \right.$$
$$\left. + \sqrt{-C_{\text{SU(4)}}\alpha_t} \sum_{\vec{n}} s_{\text{SU(4)}}(\vec{n},n_t)\rho(\vec{n}) \right] : \left|\Psi^{\text{free}}\right\rangle . \tag{3.61}$$

Once the trial wave function is constructed, we can use the full Hamiltonian to calculate the amplitude,

$$Z_{\text{LO}}(t) = \langle\Psi| M_{\text{LO}}^{L_{t_i}} |\Psi\rangle , \tag{3.62}$$

with $t = 2L_{t_o} + L_{t_i}$ and where we have suppressed all auxiliary field notations in the expression. Now the ground state energy is given as

$$E_{\text{LO}}\left(t - \frac{\alpha_t}{2}\right) = -\frac{1}{\alpha_t} \log \frac{Z_{\text{LO}}(t)}{Z_{\text{LO}}(t-\alpha_t)}. \tag{3.63}$$

Over and above the LO transient energy, we will measure higher-order operators $\hat{O}$ perturbatively. We insert them in the center of our amplitude calculation,

$$Z_{\hat{O}}(t) = \langle\Psi| (M_{\text{LO}})^{L_{t_i}/2} M_{\hat{O}} (M_{\text{LO}})^{L_{t_i}/2} |\Psi\rangle , \tag{3.64}$$

with an energy contribution

$$E_{\hat{O}} = \frac{1}{\alpha_t}\left(1 - \frac{Z_{\hat{O}}}{Z_{\text{LO}}} + \ldots\right) \quad . \tag{3.65}$$

The time evolution for the different time steps is shown schematically in Fig. 3.4. Note that for the evaluation of the transient energy and perturbative insertions, one normaly evaluates the amplitude between neighboring time slices. Additionally, one could also take next-to-neighboring time slices and so on to get energies for times between t_o and t_i. However, it has been shown earlier that the data becomes poorly decorrelated quickly. In the following calculations, we will take neighboring and – if possible – partially next-to-neighboring time slices only. The operator $M_{\hat{O}}$ is constructed from an extended auxiliary field transfer matrix $M(\pi_I, s, s_S, s_I, s_{SI}, \epsilon)$ which includes all necessary operator structures in the form of external currents. In the following we give an explicit example for a simple two-body contact interaction without any spin, isospin or momentum dependence while all other interaction operators are calculated analogous after including the respective current structure in the transfer matrix. Hence, the transfer matrix is defined as

$$M\left(\pi_I, s, s_S, s_I, s_{SI}, \epsilon_\rho\right) = M(\pi_I, s, s_S, s_I, s_{SI}) \exp\left[\sum_{\vec{n}} \epsilon_\rho(\vec{n},n_t)\rho(\vec{n})\right]. \tag{3.66}$$

Then the perturbative insertion reads

$$\Delta M_\rho \propto -\alpha_t \sum_{\vec{n}} \frac{\delta}{\delta\epsilon_\rho(\vec{n},n_t)} \frac{\delta}{\delta\epsilon_\rho(\vec{n},n_t)} M(\pi_I, s, s_S, s_I, s_{SI}, \epsilon_\rho). \tag{3.67}$$

Now the amplitude is defined in terms of the auxiliary fields and we can use the HMC method to

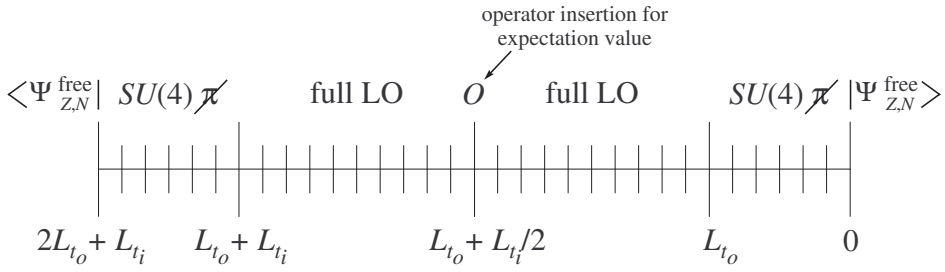

Figure 3.4: Schematic time steps for time evolution. Figure taken from [33].

determine the ground state energy. The procedure is as follows:

1. Initialization
   Firstly, we create a random configuration of auxiliary fields s_X, where s_X is an abbreviation for all auxiliary fields of the theory used in Eqs. (3.56), (3.57), and (3.61).

2. Molecular dynamics
   Corresponding to the initial configuration we create the conjugate momenta randomly according to a Gaussian distribution,
   $$P\left[p_{s_X}(\vec{n},n_t)\right] \propto \exp\left\{-\frac{1}{2}\left[p_{s_X}(\vec{n},n_t)\right]\right\}. \tag{3.68}$$
   The weight $\exp[-V(s)]$ and has the explicit form
   $$|Z(L_t)|\exp\left(-S_{s_X}\right), \tag{3.69}$$
   and it is used for the Hamiltonian dynamics of the auxiliary fields according to
   $$\dot{p}_{s_X}(\tau) = -\frac{\partial H_{\text{HMC}}}{\partial s_X}, \tag{3.70}$$
   $$\dot{s}_X(\tau) = p_{s_X}, \tag{3.71}$$
   whereas H_{HMC} is
   $$H_{\text{HMC}} = \frac{1}{2}p^2_{s_X} + V(s_X). \tag{3.72}$$

3. Exploring the phase space
   With the previous equations we can explore the phase space of the process using the discretized equations. Therefore, we use the leapfrog method, which is a simple and phase space area preserving discretization scheme. We start with a half step departing from the initial configuration,
   $$p'_{s_X}(0) = p_{s_X}(0) - \frac{\epsilon_{\text{HMC}}}{2}\dot{p}_{s_X}(0). \tag{3.73}$$
   Afterward we explore the phase space with full step size,
   $$s_X(\tau+1) = s_X(\tau) + \epsilon_{\text{HMC}}p'_{s_X}(\tau), \tag{3.74}$$
   $$p'_{s_X}(\tau+1) = p_{s_X}(\tau) + \epsilon_{\text{HMC}}\dot{p}'_{s_X}(\tau), \tag{3.75}$$

and add an additional half step in the end,

$$p_{s_X}(N_\tau) = p'_{s_X}(N_\tau) + \frac{\epsilon_{\text{HMC}}}{2}\dot{p}'_{s_X}(N_\tau). \tag{3.76}$$

The evaluation of momenta between two full steps pushes the error to $O(\epsilon^3_{\text{HMC}})$ instead of $O(\epsilon^2_{\text{HMC}})$ in the case of evaluating the field and the conjugate momenta at the same time point. For an efficient algorithm, it is necessary to choose the number of time steps N_τ and the step length ϵ_{HMC} such that the final acceptance rate is large enough to get enough statistics but also that the phase space is explored rapidly enough.

4. Metropolis test - accept or reject
At the end of the molecular dynamics evolution, one has a new configuration of auxiliary fields and their momenta, $s_X(N_\tau)$, $p_{s_X}(N_\tau)$., The accept/ reject criterion reads

$$u < \min\left\{1, \exp\left\{-H_{\text{HMC}}\left[s_X(N_\tau), p_{s_X}(N_\tau)\right] + H_{\text{HMC}}\left[s_X(0), p_{s_X}(0)\right]\right\}\right\}, \tag{3.77}$$

where u is a random number between 0 and 1. The new configuration is accepted if Eq. (3.77) is fulfilled. This accept/reject criterion is called Metropolis test and it fulfills the detailed balance, a necessary condition for the reversibility of the system in equilibrium.

5. Measuring observables
If the system is already in equilibrium and the state is accepted, we take statistics of all observables according to Eqs. (3.63) and (3.65).

6. Continue from step 2
We repeat this procedure for N_{trial} times, but we use the new configuration $s_X(N_\tau)$ as a starting point if it has been accepted or we use the old configuration $s_X(0)$ if it has been rejected.

3.8 The sign problem

As long as the system scales only proportional to the number of particles and L^3 in the spatial size, we do not have any storing problems for a large number of particles or a large box size. Sure enough, in fermionic Monte Carlo systems one has to deal with a sign problem. While we interpret the Boltzman factor as a probability factor and as such allows us to calculate the average of any observable just by summing over its value for any configurations weighted by its probability, this is not possible anymore if the weight is oscillating between negative and positive, which occurs by the exchange of two fermions just by Fermi statistics. Such a new configuration would cancel the old one making it very hard to extract any valuable information from a Monte Carlo simulation. To be specific, we follow [105] and consider a fermionic and bosonic path integral,

$$Z_f = \sum_n \text{Sign}(n) \exp\left[-S(n)\right], \tag{3.78}$$

$$Z_b = \sum_n \exp\left[-S(n)\right], \tag{3.79}$$

with $\mathrm{Sign}(n) = \pm 1$ depending on the configuration n of the system. $S(n)$ is an action of a bosonic system. Any fermionic observable is calculated as

$$\langle O \rangle_f = \frac{1}{Z_f} \sum_n O(n)\,\mathrm{Sign}(n) \exp\left[-S(n)\right], \tag{3.80}$$

which directly gives the expectation value of the Sign operator itself,

$$\langle \mathrm{Sign} \rangle = \frac{Z_f}{Z_b} \propto \exp\left[-\beta V \left(f_f - f_b\right)\right], \tag{3.81}$$

where the last equation is valid for large βV with the inverse temperature $\beta = 1/(k_B T)$ and f_f, f_b the free energy of the fermionic and bosonic system, respectively. Due to the Pauli principle the free energy density for fermions must be larger than the one for bosons and as such the average sign tends towards zero exponentially for larger volumes.

Generally, the sign problem becomes severe when very sharp potentials are employed or when including many fermions. In the framework of NLEFT, we can use a relatively low cutoff and trigonometric discretization schemes are used to reduce the sign problem. Concerning this thesis we restrict the Monte Carlo calculation to ^{4}He, which is almost a SU(4) eigenstate. SU(4) symmetric problems do not suffer from the sign problem and consequently, we do not expect too severe problems for the ^{4}He calculation.

CHAPTER 4

Regularization Methods for Nuclear Lattice Effective Field Theory★

4.1 Introduction

The Nuclear Lattice Effective Field Theory (EFT) method [33] has led to impressive progress in the last decade and it has been applied to few- and many-body-systems successfully, for reviews see e.g. Refs. [52, 107]. The lattice spacing serves as a natural UV regulator for the theory, as for a given value of a the maximal momentum is $p_{max} = \pi/a$. Although these calculations give a quite good description for the phase shifts, energy levels, etc., almost all calculations have been done for a fixed lattice spacing $a \simeq 2\,\mathrm{fm}$, corresponding to a soft momentum cut-off of about 300 MeV. This allows one to treat all corrections beyond leading order (LO) in perturbation theory. However, the cut-off dependence or lattice spacing dependence has not been analyzed systematically and there are still some problems in the two-nucleon system like the relatively poor description of the $^3S_1$-$^3D_1$ mixing angle [61]. Further, such soft potentials seem to lead to some overbinding in medium-mass nuclei, as discussed in Ref. [108]. Also, it has been shown that the leading order four-nucleon contact interactions need to be smeared to avoid a cluster instability when four nucleons reside on one lattice site [32]. One might argue that the extension of such smearing methods also to the pion exchange contributions leads to a natural regularization of the lattice EFT, allowing to vary the lattice spacing freely but using an explicit momentum cut-off in the spirit of the work of Ref. [38]. More precisely, this inherent physical cut-off was implemented by formulating the lattice action in terms of blocked fields.

In this chapter, we will focus on the neutron-proton two-body system at lowest order and discuss the lattice spacing dependence systematically. In addition, we discuss the necessity of regularizing the one-pion-exchange potential and provide a method that goes beyond smearing and is borrowed from continuum calculations, which leads to the lattice spacing independence of observables for a broad range in a, see Ref. [22].

While most of the calculations solve the transfer matrix using Monte Carlo methods or the Lanczos method for small eigenvalues of large sparse matrices, we use here the Hamiltonian formalism and solve it with the Lanczos method. Using this approach we can eliminate the discretization in the time direction and we have to consider only the variation in the position space discretization. In the following, all expressions are given in lattice units and one has to multiply the lattice results by the appropriate power of the lattice spacing a to get the physical values. Note also that we show simulations for various large enough volumes so that Lüscher's finite volume formulas are sufficient for the infinite volume extraction

★ The following chapter has been published in [106].

and we can entirely focus on the remaining dependence on the lattice spacing.

In what follows, we will first display the necessary formalism to calculate the neutron-proton system to lowest order on the lattice. It is important to already improve the free Hamiltonian so as to be as close as possible to the free non-relativistic dispersion relation. At very low energies, one can consider the theory with contact interactions only, the so-called pionless theory. As we will show, the smearing of the contact interactions can be used as a regulator, leading to regulator-independent results for a broad range of values of the lattice spacing a. Matters are different in the pionful theory, which to LO consists of two four-nucleon contact interaction and the long-ranged static one-pion-exchange potential (OPEP). As will be shown, combining the smearing of the contact interactions with a position-space regularization of the OPEP will again lead to results largely independent of a for the physically sensible range of lattice spacing. Hence, one could use this modified leading-order approach to improve the current auxiliary field Monte Carlo simulations in Nuclear Lattice EFT. In principle, now it is possible to consider the continuum limit $a \to 0$, however, we refrain from doing that here, as it is sufficient to demonstrate lattice spacing independence for a physically relevant range of a.

4.2 The lattice Hamiltonian

To set the stage and to introduce our notations, we first discuss the free Hamiltonian. Its discretized form reads

$$H_{\text{free}} = \frac{1}{2m_N} \sum_{\vec{n},i,j} \sum_{\hat{l}} \Bigg\{ 2\omega_0 a^\dagger_{i,j}(\vec{n})\, a_{i,j}(\vec{n}) + \sum_{k=1}^{3} (-1)^k \times \omega_k \left[a^\dagger_{i,j}(\vec{n})\, a_{i,j}\left(\vec{n} + k\hat{l}\right) + a^\dagger_{i,j}(\vec{n})\, a_{i,j}\left(\vec{n} - k\hat{l}\right) \right] \Bigg\} . \tag{4.1}$$

Here, $a_{i,j}, a^\dagger_{i,j}$ are the fermionic annihilation and creation operators with spin and isospin indices i, j, respectively, $m_N = (m_p + m_n)/2$ denotes the nucleon mass and $\hat{l}$ is a unit vector in spatial direction. The summation is over all lattice points $\vec{n}$ on the L^3 lattice. We use a stretched $O(a^m)$-improved action and its coefficients ω_k are summarized in Tab. 4.1, see e.g. Refs. [109, 110]. m indicates the number of hopping points beyond next-neighbor interaction used in the Laplacian discretization in each spatial direction and we use $m = 4$ throughout this chapter. The stretching factor N is introduced to minimize the errors arising from the discretized dispersion relations on the lattice especially for large momenta where the discretization does not approximate the continuum relation $E = \vec{p}^{\,2}/(2m_N)$ anymore. While there is some arbitrariness on the exact choice of N depending on the values of the respective momentum, $N = 3.5$ is a sensible choice.

	$O(a^4)$		$O(a^2)$
ω_0	$N \cdot \frac{1}{9} + \frac{49}{36}$	o_0	0
ω_1	$N \cdot \frac{1}{6} + \frac{3}{2}$	o_1	$\frac{4}{3}$
ω_2	$N \cdot \frac{1}{15} + \frac{3}{20}$	o_2	$\frac{1}{6}$
ω_3	$N \cdot \frac{1}{90} + \frac{1}{90}$	o_3	0

Table 4.1: The ω_i are the coefficients for the lattice discretization of the Laplacian and the dispersion relation whereas the o_i appear in the momentum components of the one-pion-exchange potential. Both depend on the stretching factor N.

The interaction potential consists of two/three terms in the pionless/pionful theory at lowest order. The contact interaction consists of two terms which can be chosen as

$$H_{\text{cont}} = \frac{1}{2}\sum_{\vec{n}}\left[C\rho^{a^\dagger,a}(\vec{n})\rho^{a^\dagger,a}(\vec{n}) + C_I\sum_I \rho_I^{a^\dagger,a}(\vec{n})\rho_I^{a^\dagger,a}(\vec{n})\right], \tag{4.2}$$

where the terms are summed over all lattice sites $\vec{n}$ and the isospin index $I = 1,2,3$. These terms appear in both versions of the EFT considered here. In the pionful theory, one has in addition the one-pion-exchange potential

$$H_{\text{OPE}} = -\frac{g_A^2}{8F_\pi^2}\sum_{S_1,S_2,I}\sum_{\vec{n}_1,\vec{n}_2} G_{S_1S_2}(\vec{n}_1-\vec{n}_2)\rho_{S_1,I}^{a^\dagger,a}(\vec{n}_1)\rho_{S_2,I}^{a^\dagger,a}(\vec{n}_2)\ , \tag{4.3}$$

with g_A the axial-vector coupling constant and F_π the pion decay constant. S_1, S_2 are the respective spin indices which run from 1 to 3. The corresponding lattice density operators read

$$\rho^{a^\dagger,a}(\vec{n}) = a_{i,j}^\dagger(\vec{n})\,a_{i,j}(\vec{n}), \tag{4.4}$$

$$\rho_I^{a^\dagger,a}(\vec{n}) = a_{i,j}^\dagger(\vec{n})\,\tau_{I,jj'}a_{i,j}(\vec{n}), \tag{4.5}$$

$$\rho_{S,I}^{a^\dagger,a}(\vec{n}) = a_{i,j}^\dagger(\vec{n})\,\sigma_{S,ii'}\tau_{I,jj'}a_{i,j}(\vec{n}), \tag{4.6}$$

and $G_{S_1S_2}(\vec{n})$ represents the pion propagator times the pion-nucleon vertex and is defined as

$$G_{S_1S_2}(\vec{n}) = \frac{1}{L^3}\sum_{\vec{p}}\frac{\exp(-i\vec{p}\cdot\vec{n})\,\nu\left(p_{S_1}\right)\nu\left(p_{S_2}\right)}{1+\frac{2}{q_\pi}\sum_{k=1}^{3}\sum_l(-1)^k\omega_k\cos(kp_l)} \tag{4.7}$$

with $q_\pi = M_\pi^2 + 6\omega_0$. $\nu(p_{S_1})$, $\nu(p_{S_2})$ are the discretized momentum components of the first and second pion field which yields $\nu(p_l) = o_1\sin(p_l) - o_2\sin(2p_l) = p_l(1+O(p_l^4))$ with the coefficients summarized in Tab. 4.1. We only use an $O(a^2)$ discretization, because we do not want to expand the respective interaction too much. A further improved momentum approximation is linked to a further expanded derivative in position space including more interactions at distinct lattice points and the locality of the pion-nucleon interaction is lost. These momenta arise from the pion field derivative in the pion nucleon Lagrangian $\mathcal{L}_{\pi N} = -g_A/(2F_\pi)N^\dagger\vec{\tau}\cdot(\vec{\sigma}\cdot\vec{\nabla})\vec{\pi}N$. To arrive at Eq. (4.7), we note that the pion propagator is derived from the discrete action for instantaneous pions which takes the form [32]

$$S_{\pi\pi}(\pi_I) = \left(\frac{m_\pi^2}{2}+3\omega_0\right)\sum_{\vec{n}}\pi_I(\vec{n})\,\pi_I(\vec{n}) + \sum_{\vec{n},\hat{l},k}(-1)^k\,\omega_k\pi_I(\vec{n})\,\pi_I\left(\vec{n}+k\hat{l}\right). \tag{4.8}$$

This is reparametrized by $\pi_I'(\vec{n}) = \sqrt{q_\pi}\pi_I(\vec{n})$. Finally, the new pion action reads

$$S_{\pi\pi}\left(\pi_I'\right) = \frac{1}{2}\sum_{\vec{n}}\pi_I'(\vec{n})\,\pi_I'(\vec{n}) + \frac{1}{q_\pi}\sum_{\vec{n},\hat{l},k}(-1)^k\,\omega_k\pi'(\vec{n})\,\pi_I'\left(\vec{n}+k\hat{l}\right) \tag{4.9}$$

and the respective pion propagator reads

$$D_\pi(\vec{p}) = \left[1 + \frac{2}{q_\pi}\sum_{k=1}^{3}\sum_{l}(-1)^k \cos(kp_l)\right]^{-1} . \tag{4.10}$$

Furthermore, we introduce a Gaussian smearing

$$f(\vec{p}) = \frac{1}{f_0}\exp\left[-b\frac{\tilde{v}(\vec{p})}{2}\right] \tag{4.11}$$

with a stretched $O(a^4)$ improved discretization

$$\tilde{v}(\vec{p}) = 2\sum_{k=0}^{3}\sum_{l=1}^{3}(-1)^k\omega_k\cos(kp_l) = \vec{p}^{\,2}\left[1 + O\left(p^6\right)\right] , \tag{4.12}$$

where the error estimation is valid for $N = 0$ and the coefficients given in Tab. 4.1. f_0 is necessary for normalization reasons and is given by $f_0 = (1/L^3)\sum_{\vec{p}}\exp[-b\tilde{v}(\vec{p})/2]$. This smearing modifies the contact interaction in momentum space according to

$$H_{\text{cont}} = \frac{1}{2}\sum_{\vec{p}} f(\vec{p})\left[C\rho^{a^\dagger,a}(\vec{p})\rho^{a^\dagger,a}(\vec{p}) + C_I\sum_I \rho_I^{a^\dagger,a}(\vec{p})\rho_I^{a^\dagger,a}(\vec{p})\right] . \tag{4.13}$$

Such a smearing was introduced in Ref. [32] to reduce the effect of high momentum contributions and remove the clustering instability of the contact interaction. As the leading order (LO) contribution is iterated to all orders, such a smearing sums up some of the higher order corrections. All other higher order corrections are then treated in perturbation theory (as long as the lattice spacing is sufficiently large). Here, we concentrate on the lowest order and leave the discussion of the treatment of the higher order effects to Chap. 5. In any case, the smearing of the LO contact terms is a useful tool to improve the description of the S-waves in a very efficient way without including all higher-order terms in a chiral counting scheme. In general, it is not necessary that the smeared contact interactions for the ${}^1S_0$- and ${}^3S_1$-channel have the same smearing function, $f(\vec{p})$. However, this is important for auxiliary-field Monte Carlo lattice simulations. Without the same smearing function for the two channels, the Monte Carlo simulation would have a far bigger problem with sign oscillations. For this reason we consider only one smearing function for both channels. The fact that we can approximately describe the effective ranges for both channels using only one smearing function can be viewed as a feature of the approximate SU(4) Wigner symmetry of the two-nucleon interaction.

In continuum chiral EFT it is necessary to regularize the one-pion-exchange potential due to its singularity at very small distances. We will show that such a singularity also appears for small lattice spacings and we will regularize it in position space as suggested in Ref. [22]

$$\tilde{f}(\vec{r}) = \left[1 - \exp\left(-\frac{\vec{r}^{\,2}}{2b}\right)\right]^n , \tag{4.14}$$

where the denominator is motivated by $\mathcal{F}_q\{\exp[-r^2/(2b)]\} \propto \exp(-bq^2/2)$. Here, b is a fitting parameter while n is a free parameter.

In the following we study the two-nucleon system for different lattice spacings. Therefore we use the finite-volume formulas for the binding energy and the effective range expansion given by Lüscher [84,

93]

$$E_B(L) - E_B^\infty = -24|A|^2 \frac{\exp\left(-\sqrt{-2\mu E_B^\infty}L\right)}{2\mu L}, \tag{4.15}$$

$$p\cot\delta_0(p) = \frac{1}{\pi L}S(\eta), \quad \eta = \left(\frac{Lp}{2\pi}\right)^2, \tag{4.16}$$

with A the normalization constant of the wave function for large distances and $\mu = m_p m_n/(m_p + m_n)$ the reduced mass. The energy eigenvalues of the system are linked to the momentum squared by $E = p^2/(2\mu)$ and $S(\eta)$ is the zeta function. Its expansion for small η is given by

$$S(\eta) = -\frac{1}{\eta} + S_0 + S_1\eta^1 + S_2\eta^2 + S_3\eta^3 + \ldots \tag{4.17}$$

and the coefficients S_i can be found in Chapt. 3.4.1. We do calculations at volumes large enough that Lüscher's finite volume formulas are sufficient for infinite volume extraction with negligible residual finite volume dependence so we can entirely focus on the remaining dependence on the lattice spacing. For the scattering state calculations, the finite volume corrections are of size $\exp(-L/R)$, where L is the box length and R is the range of the interactions [84]. For the bound state calculations, the finite-volume formula in Eq. (4.15) captures the leading $\exp(-\sqrt{-2\mu E_B^\infty}L)$, but there are also smaller corrections of size $\exp(-\sqrt{2}\sqrt{-2\mu E_B^\infty}L)$ [93]. For S-waves, the effective range expansion is $p\cot\delta_0(p) \approx -1/a_s + (r_e/2)p^2$ with a_s the scattering length and r_e the effective range. Hence, we match our finite volume results to the infinite volume effective range parameters and the deuteron binding energy, $a_{^1S_0} = -23.76(1)$ fm, $r_{^1S_0} = 2.75(5)$ fm, and $E_b = -2.224575(9)$ MeV.

In the fits, different lattice volumes are used to produce enough data points to make the respective fit using Eqs. (4.15,4.16) and predict $r_{^3S_1}$ as well as $a_{^3S_1}$. Finally, one can compare the prediction to the experimental values given by $a_{^3S_1} = 5.424(4)$ fm and $r_{^3S_1} = 1.759(5)$ fm. In the following we will repeat this procedure for lattice spacings between $a^{-1} = 100$ MeV and $a^{-1} = 400$ MeV, respectively, that is approximately between 2 fm and 0.5 fm in the pionless theory and for a between 0.3 and 2.0 fm the EFT with pions.

4.3 The pionless theory

a^{-1} [MeV]	a [fm]	$C_{^3S_1}$ [MeV]	$C_{^1S_0}$ [MeV]	b [MeV^{-2}]	$a_{^3S_1}$ [fm]	$r_{^3S_1}$ [fm]
100	1.97	−46.66	−28.18	$3.83 \cdot 10^{-5}$	5.611(1)	2.029(1)
130	1.52	−50.71	−30.16	$3.93 \cdot 10^{-5}$	5.630(1)	2.047(1)
160	1.23	−50.26	−29.84	$4.04 \cdot 10^{-5}$	5.624(1)	2.034(1)
200	0.99	−49.89	−29.70	$4.13 \cdot 10^{-5}$	5.614(1)	2.017(1)
240	0.82	−50.17	−29.92	$4.19 \cdot 10^{-5}$	5.607(1)	2.008(1)
300	0.66	−50.63	−30.24	$4.23 \cdot 10^{-5}$	5.602(1)	2.005(1)
350	0.56	−50.85	−30.38	$4.25 \cdot 10^{-5}$	5.601(1)	2.008(1)
400	0.49	−50.91	−30.43	$4.27 \cdot 10^{-5}$	5.605(1)	2.015(1)

Table 4.2: Fit results in the Gaussian-smeared pionless EFT case for $L = 34, 36, 38$ and $N = 3.5$. The values for $a_{^3S_1}$ and $r_{^3S_1}$ are predictions (modulo the consistency condition Eq. (4.20)).

Initially, we consider the pionless case which works well for very low energies and is described by the effective Hamiltonian

$$H = H_{\text{free}} + H_{\text{cont}} \,. \tag{4.18}$$

It was shown in Ref. [111] that for any lattice spacing the non-smeared contact interaction cannot reproduce the effective range correctly. Hence, we introduce a smearing according to Eq. (4.11). The calculation is performed for $N = 0$ and $N = 3.5$ to estimate the influence of the stretching factor in the improved action. As we only have to consider the S-wave projection, we use the appropriate linear combinations

$$C = \frac{1}{4}\left(3C_{^1S_0} + C_{^3S_1}\right) \quad C_I = \frac{1}{4}\left(C_{^1S_0} + C_{^3S_1}\right) \,. \tag{4.19}$$

The results for two stretching factors $N = 0$ and $N = 3.5$ are shown in Fig. 4.1. For $N = 3.5$, the explicit values of the fitted parameters and the predictions are listed in Tab. 4.2. The lattice size of $L = 34, 36, 38$ is motivated by the corresponding physical lattice length of $L_{\text{phys}} = 16.66, 17.64, 18.62$ fm for a minimal lattice spacing of $a = 0.49$ fm. This should be still large enough so that higher order terms to Eqs. (4.15,4.16) and in the effective range expansion are negligible. The LECs in the respective table and plot are obtained after rescaling $C_{^3S_1/^1S_0} \to C_{^3S_1/^1S_0}/a^3$ so as to account for the different volumes.

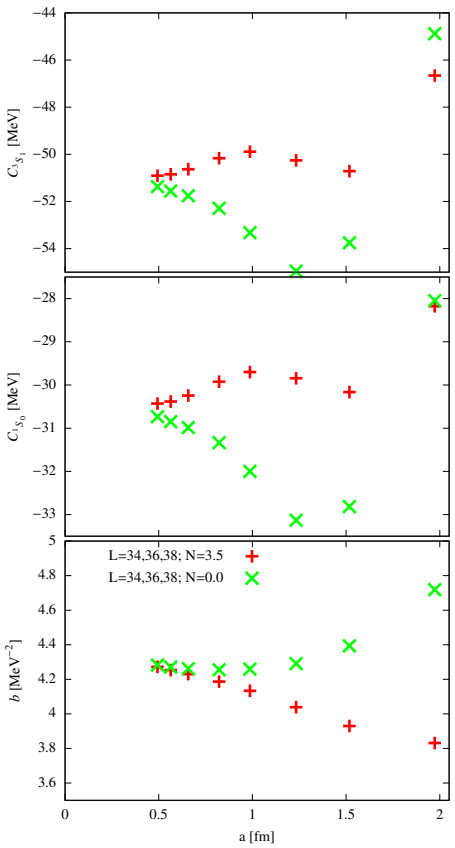

Figure 4.1: Low-energy coupling constants and the smearing parameter b in the pionless EFT for a lattice size of $L = 34, 36, 38$ and two different stretching factors.

First, we see the parameters belonging to $N = 0$ and $N = 3.5$ have similar values and they approach a constant value when the lattice spacing is minimized. But there is a preference for $N = 3.5$ case because for this case, the variation of the LECs is significantly decreased for various lattice spacings than in the

$N = 0$ case reflecting the improved dispersion relation approximation which is necessary as we receive data points in different regimes for different lattice spacings. Therefore, we use $N = 3.5$ for the following calculations.

Comparing the theoretical predictions with the experimental values gives the impression of a large deviation particularly for $r_{^3S_1}$. As we only work at lowest order, we cannot expect to get the physical value already. But we can perform a consistency check for our predictions as there exists a relation between the binding energy, the scattering length and the effective range, see e.g. Ref. [23]

$$E_B \approx -\frac{1}{2\mu a_s^2}\left(1 + \frac{r_e}{a_s} + \frac{5r_e^2}{4a_s^2} + \dots\right) . \tag{4.20}$$

This equation is valid for positive scattering length a_s and the expansion in r_e/a_s, with r_e the effective range, is useful provided $|r_e| \ll a_s$. As we do not include any partial wave mixing, we can use the expansion up to $O(r_e^2/a_s^2)$ and compare the physical binding energy in this scheme with our lattice predictions. Then the binding energy is $E_B = -2.052(1)$ MeV for the physical values of the scattering length and the effective range and our lattice predictions give a binding energy of $E_B = -2.009(1) \dots - 1.999(1)$ MeV showing that the relation in Eq. (4.20) is approximately fulfilled.

The constant value of b can be explained by the smearing function itself and the Fourier transformation of the contact interaction given in Eq. (4.13) in dependence of the cutoff/ lattice spacing. While we work on the lattice, the Fourier transformation is limited by the maximum momentum π/a. As we consider the continuum limit, new contributions to the summation are added in Eq. (4.13) as $\pi/a \to \infty$ and the value of the normalization constant changes. The normalization constant f_0 approaches a finite limit and the new contributions are exponentially suppressed. Hence, the lattice spacing dependence of the smearing constant should approach a constant value as long as other discretization errors are negligible. This is also a good check for other regularizations procedures. We will use this condition to find the best regularization scheme in the upcoming section. It is quite remarkable that the pionless theory can be regularized by such a constant Gaussian smearing leading to a-independent results for $0.5 \lesssim a \lesssim 2.0$ fm. Given that the typical extension of a nucleon is given by a scale of $r \simeq 0.85$ fm, this means that the EFT can be used for all momenta that do not lead to a resolution of the internal nucleon structure, at least in the pionless theory. A direct comparison with the results of a continuum calculation is difficult because the occuring divergences are usually treated in a different way. As done in Ref. [112], one can calculate the scattering matrix using the bubble chain summation with a regularization $\tilde{f}(\vec{p}) = \exp(-b\vec{p}^2/2)$ similar to the smeared contact interaction on the lattice instead of dimensional regularization or a finite cut-off. Then the T-matrix is expanded up to and including $O(\vec{p}^2)$ and matched to the effective range expansion parameters. The values one obtains are of the same order as the lattice values but do not match them exactly. Note further that the extension to the three-particle system is not straightforward because of the Efimov effect that requires the inclusion of a three-body contact interaction already at leading order [113].

4.4 The pionful theory

Including pions is necessary for an effective field theory at higher energies. Therefore pions are included according to Eq. (4.3) and the full Hamiltonian is

$$H = H_{\text{free}} + H_{\text{cont}} + H_{\text{OPE}} . \tag{4.21}$$

A problem is caused by the singularities which arise in the short-range region of the OPE contribution. On the one hand, this singularity exists for any lattice spacing as the relative distance $\vec{r} = 0$ is possible and gives a very large but still finite contribution. On the other hand, minimizing the lattice spacing leads to additional lattice points with non-zero but very small distances to the origin and which give an additional large short-range contribution.

Firstly, we switch off the smearing of the contact interaction and include the pion-nucleon interaction according to Eq. (4.3). In this case, the predictions for the effective range parameter are not close to the physical value and it is still necessary to include the smearing of the contact interaction [32].

In the case of smeared contact interaction and non-smeared pion-nucleon interaction the LECs do not give a reasonably close value for the effective range in the ${}^3S_1$-channel. The prediction is reasonable and constant for a lattice spacing larger than 1 fm, but it does decrease towards zero for smaller lattice spacings. As we do not include a regularization, the divergent πN-contribution for small lattice spacings is more and more resolved for smaller lattice spacings resulting in a very sharp potential. The contact interaction in combination with the smearing factor b can compensate this effect but as the ${}^1S_0$- and ${}^3S_1$-channel do not have exactly the same dependence, while it is still possible to fit to one of the effective ranges, the agreement for the other one gets worse.

Now we turn on the smearing of the pion-nucleon interaction. While a smearing in momentum space according to Eq. (4.11) could be possible, we follow the arguments given in Ref. [22] and introduce the regularization in position space as proposed in Eq. (4.14). Then, the new OPE potential reads

$$H_{\mathrm{OPE}} = -\frac{g_A^2}{8F_\pi^2} \sum_{S_1,S_2,I} \sum_{\vec{n}_1,\vec{n}_2} \tilde{f}\left(\vec{n}_1 - \vec{n}_2\right) G_{S_1S_2}\left(\vec{n}_1 - \vec{n}_2\right) \rho^{a^\dagger,a}_{S_1,I}\left(\vec{n}_1\right) \rho^{a^\dagger,a}_{S_2,I}\left(\vec{n}_2\right) \ . \tag{4.22}$$

Throughout this chapter, we use $n = 4$ in Eq. (4.14), but we also checked for different n and the results are similar. Higher values of n are only necessary for strongly divergent contributions like two-pion-exchange potentials which we neglect in this exploratory study.
In Fig. 4.2, the finite volume binding energy of the deuteron and the respective effective range expansion for the S-waves for a subset of the lattice spacings used are shown. Finite volume effects modify the binding energy so that a correction according to Eq. (4.15) is necessary but higher order terms are still negligible. Also the data points we obtain for the effective range expansion still have small enough momenta squared so that the expansion up to $O(p^2)$ is feasible. The resulting LECs, the smearing constant as well as the predictions for $L = 34, 36, 38$ are displayed in Tab. 4.3. While the value of the LECs are different to the pionless case, their general shape depending on the lattice spacing does not change and the LECs remain negative as well. Also the smearing factor b remains in a certain range between 2.40 to 2.92 $\times 10^{-5}\,\mathrm{MeV}^{-2}$, indicating that this regularization scheme works quite well. We do not show the results for the smaller set of lattice sizes, but we have shown that finite volume effects between these two sets become negligible for lattice spacings larger than 0.7 fm. Assuming a large enough lattice there is a rise in the smearing constant between 1.8 fm and 0.7 fm, and it is constant again for lattice spaces smaller than 0.7 fm. While in the range from 0.7 fm and 1.8 fm the pion-nucleon contribution changes, the lattice sites closest to the origin contribute more and more to the potential due to the divergent structure of the potential. This effect is compensated by the regularization at a certain range as we further decrease the lattice spacing, and then the regularized potential does not change its shape anymore. Note that in the intermediate range there are lattice artifacts in the OPEP which cause the oscillatory behavior of the LECs as they appear at different physical lengths and multiplied by a different regularization factor. As a result, we cannot see a plateau for the LECs $C_{^3S_1}$ and $C_{^1S_0}$ at a lattice spacing of $a = 0.5$ fm, but we have to further decrease the lattice spacing. Simultaneously, we increase the number of lattice points to

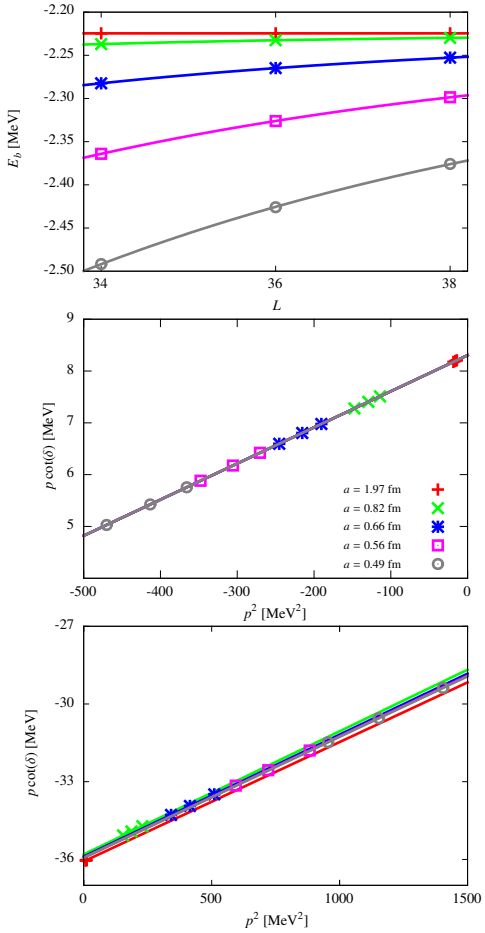

Figure 4.2: Lattice space dependence of various parameters. Upper panel: The finite-volume deuteron bound state energy. Central panel: The effective range expansion for the ${}^1S_0$-channel. Lower panel: The effective range expansion for the ${}^3S_1$-channel.

keep the physical lattice size. The respective values are shown in Tab. 4.3 as well and there is a plateau starting from $a = 0.39$ fm. The predictions for the effective range expansion parameters are also quite good as $a_{{}^3S_1} \approx 5.470(1)\ldots5.649(1)$ fm and $r_{{}^3S_1} \approx 1.818(1)\ldots1.899(1)$ fm depending on the lattice spacing. Repeating the calculation for the binding energy according to Eq. (4.20) up-to-and-including terms of $O(r_e^2/a_s^2)$ yields for the binding energy $E_B \approx 2.026(1)\ldots2.033(1)$ MeV for the various lattice spacings in the range between 0.5 fm and 2.0 fm. This is again close to the physical binding energy and the respective relation is fulfilled. For the remaining ones, it yields $E_B \approx 2.034(1)\ldots1.899(1)$ MeV indicating that larger volumes become necessary particularly for the smallest lattice spacing. Finally, the theory is well regularized and the differences between the lattice predictions and the experimental values of $a_{{}^3S_1}$ and $r_{{}^3S_1}$, respectively, can be compensated by higher order terms.

4.5 Conclusion and Outlook

In this chapter, we have studied the lattice spacing a dependence of the neutron-proton system at leading order in the pionless and the pionful theory. We have used the scattering length and the effective range

a^{-1} [MeV]	a [fm]	$C_{^3S_1}$ [MeV]	$C_{^1S_0}$ [MeV]	b [MeV^{-2}]	$a_{^3S_1}$ [fm]	$r_{^3S_1}$ [fm]
100	1.97	−54.07	−36.11	$2.59 \cdot 10^{-5}$	5.470(1)	1.818(1)
130	1.52	−67.11	−45.47	$2.40 \cdot 10^{-5}$	5.513(1)	1.878(1)
160	1.23	−69.31	−46.52	$2.41 \cdot 10^{-5}$	5.527(1)	1.899(1)
200	0.99	−63.83	−41.39	$2.65 \cdot 10^{-5}$	5.523(1)	1.893(1)
240	0.82	−61.55	−39.23	$2.83 \cdot 10^{-5}$	5.511(1)	1.876(1)
300	0.66	−62.20	−39.44	$2.92 \cdot 10^{-5}$	5.498(1)	1.858(1)
350	0.56	−63.30	−40.19	$2.92 \cdot 10^{-5}$	5.491(1)	1.842(1)
400	0.49	−64.31	−40.97	$2.91 \cdot 10^{-5}$	5.491(1)	1.842(1)
500	0.39	−65.47	−41.90	$2.89 \cdot 10^{-5}$	5.500(1)	1.836(1)
600	0.33	−66.14	−42.71	$2.82 \cdot 10^{-5}$	5.553(1)	1.835(1)
700	0.28	−65.61	−42.64	$2.86 \cdot 10^{-5}$	5.649(1)	1.845(1)

Table 4.3: Fit results in EFT with Gaussian-smeared contact interaction and position space regularization for the pion-nucleon interaction with $N = 3.5$. The lattice size is $L = 34, 36, 38$ for $a = 0.49 \ldots 1.97$ fm and $L = 38, 40, 42$ for $a = 0.39 \ldots 0.28$ fm. The values for $a_{^3S_1}$ and $r_{^3S_1}$ are predictions (modulo the consistency condition Eq. (4.20)).

in the $^1S_0$ partial wave together with the deuteron binding energy to fix the two LECs related to the LO four-nucleon contact interaction and the smearing parameter b. To focus on the lattice spacing dependence, we have worked at sufficiently large lattice volumes so that finite volume effects do not play any role here. In the pionless case, it is sufficient to smear the contact interactions with a Gaussian-type function, cf. Eq. (4.11), to achieve a-independence in the range $0.5 \lesssim a \lesssim 2.0$ fm. We have explicitly shown this for the scattering length and the effective range in the $^3S_1$-channel, being aware of the strong correlation between E_B and $a_{^3S_1}$. In the pionful theory, the contribution from the one-pion-exchange is best to be regularized in position space, as discussed in detail in Ref. [22]. Again, we can demonstrate lattice spacing independence for the same range of a. Therefore, it should be possible to calculate the phase shifts with the transfer matrix method and the spherical wall method. Smaller lattice spacings should minimize the lattice errors such as the broken rotational invariance and make it possible to increase the accuracy especially for higher momenta in the partial wave decomposition. Clearly, when decreasing the lattice spacing, one has to be aware that the perturbative treatment of the NLO and higher order corrections becomes doubtful and requires a separate investigation but it does not invalidate the results found here. Furthermore, one should implement this regularization in Monte Carlo simulations in order to minimize the lattice spacing and artifacts in the simulation. This, however, is a separate issue.

CHAPTER 5

The Tjon band in Nuclear Lattice Effective Field Theory*

5.1 Introduction

Nuclear Lattice Effective Field Theory (NLEFT) has become a powerful tool in the last years to study the formation of nuclei from nucleons in an *ab initio* way. Using this method it was possible to calculate the binding energies of medium mass nuclei with good accuracy [108, 115] and postdict the Hoyle state [34, 35], which is an excited state in carbon-12 indispensable for nucleosynthesis in stars. Besides binding energies, also scattering processes like nucleon-nucleon [61, 116] or alpha-alpha-scattering [36] were investigated. NLEFT combines two powerful concepts. First, we have chiral nuclear effective field theory [39, 52], which gives a systematic description of low-energy hadron physics based on the symmetries (and their breaking) of the underlying gauge field theory, Quantum Chromodynamics. This continuum approach can be combined with well established many-body continuum schemes to go beyond light nuclei, such as the shell model, the no-core-shell model, coupled cluster theory, variational Monte Carlo methods, and so on, see e.g. Refs. [117–127]. Second, we discretize Euclidean space time with spatial lattice spacing a and temporal lattice spacing a_t, and use Monte Carlo methods for the numerical evaluation of few- and many-body problems. While many interesting and precise results could be obtained in this scheme, a problem due to the discretization of space had never been resolved in a satisfactory fashion. In Ref. [115] an overbinding of the ground state of ^{4}He was observed which was traced back to the appearance of implicit multi-particle interactions which have significant effect on few-body physics on coarse lattices. In Ref. [128], this effect was demonstrated explicitly for an N-boson system in two dimensions with short-range interaction. This effect becomes even stronger in larger nuclei. In Ref. [108] this discretization artefact was cured by adding an *effective* four-nucleon force (4NF), that, however, is not related to the chiral expansion. Here, we want to reconsider this issue and prove the conjecture of the appearance of the implicit multi-particle interactions, and show that with decreasing lattice spacing their effect is diminished more and more. Consequently, the effective 4NF is not necessary any more once the lattice spacing is chosen small enough, and one should also confirm the correlation between $3N$ and $4N$ systems, known as the Tjon band [24, 72]. Note that historically, this correlation was called the Tjon line, but as theory has an inherent uncertainty, it really is a band as stressed in Ref. [72]. While the aforementioned overbinding of ^{4}He on coarse lattices results in correlation points relatively far off the Tjon band, the binding energies for triton and helium-4 should get closer to this band or already be on top of it once the lattice spacing is chosen small enough. Furthermore, note that one also has to

* The following chapter has been published in [114].

be aware of an additional effect that needs proper treatment. The configurations with four nucleons on one lattice site require smearing to prevent a strong overbinding [32]. In the chiral EFT action used for most investigations, this smearing was adjusted to get the proper neutron-proton effective range. This procedure might, however, not be sufficient in larger systems, as evidenced by the highly successful non-locally smeared leading order action proposed in Ref. [129].

Different to lattice QCD, we do not consider the continuum limit $a \to 0$. This is related to the fact that we are dealing with an effective field theory (EFT) that is only valid for a certain energy range. In fact, π/a serves as the ultraviolet cut-off of this EFT. Letting a tend to zero would generate large momenta that probe the inner structure of the nucleons, which is outside the realm of the EFT considered. Therefore, a must be chosen between 1 and 2 fm. This was explained e.g. in Ref. [82].

The EFT provides a counting scheme for the expansion of the effective potential [14] systematically up to any given order $\mathcal{O}(Q/\Lambda)$, where Q is a small expansion parameter with respect to the nuclear hard scale $\Lambda \approx 500\,\mathrm{MeV}$. Note that this hard scale is smaller than the usual chiral perturbation theory scale because of the non-perturbative nature of the nuclear interactions. For a detailed discussion, see e.g. Ref. [22]. The pertinent small expansion parameter in our case is the nucleon momentum p or the pion mass M_π or the electromagnetic charge $e \propto M_\pi/\Lambda$. Within this counting scheme, the two-body contact interactions start at leading order (LO), $\mathcal{O}[(Q/\Lambda)^0]$, while momentum-dependent and electromagnetic interactions are at next-to-leading order (NLO), $\mathcal{O}[(Q/\Lambda)^2]$ and do not have any additional contribution at N2LO, $\mathcal{O}[(Q/\Lambda)^3]$. Additional contact terms would arise at N3LO, $\mathcal{O}[(Q/\Lambda)^4]$, which is beyond the accuracy of our calculations in the three- and four-body sector performed here. The two-pion-exchange potential (TPEP) has contributions at NLO and N2LO. A detailed analysis of the lattice spacing dependence of the two-body sector can be found in Ref. [116], where higher-order corrections were included both perturbatively and non-perturbatively. In the following we will include and extend the two-body analysis, but we will focus on the perturbative approach as we want to be in agreement with former three- and four-body calculations in which all corrections beyond LO have been included perturbatively. In the three-body sector, 3NF corrections only start at N2LO as NLO contributions only consist of reducible topologies which do not produce any non-vanishing contributions. Concerning the 4NF, it was conjectured that they are not necessary due to the same argument of vanishing contributions for 3NF. However, it was shown by Ref. [130] that these forces matter at N3LO and a rough estimation of some of their contribution gives to the binding energy of ^{4}He is about 100 keV [131]. Hence, since they are beyond the order we include in our analysis and their actual contribution is beyond the accuracy of our work as well, we can safely neglect them. We remark that these chiral 4NFs are not the effective 4NFs that were included in Ref. [108].

The chapter is organized as follows. In Sec. 5.2 we introduce the method of NLEFT with an emphasis on the two-body sector. We calculate phase shifts up to N2LO for neutron-proton scattering, and we consider electromagnetic corrections for neutron-neutron and proton-proton scattering. Then in Sec. 5.3, we extend the method to three-body systems and calculate the properties of triton at each order in the framework of NLEFT. When describing the four-body system in Sec. 5.4, we also give a brief introduction into Monte Carlo method which is necessary for the calculation of the ^{4}He properties. All calculations are done for lattice spacings of $a = 1.97$ fm, $a = 1.64$ fm and $a = 1.32$ fm, which means that the respective cutoff $\Lambda_a = \pi/a$ remains below the breakdown scale of the theory. The respective temporal lattice spacing is chosen as $a_t = 1.32$ fm, $a_t = 0.91$ fm and $a_t = 0.59$ fm, such that the ratio a^2/a_t is kept fixed. Finally, we investigate the ^{3}H-^{4}He correlation in Sec. 5.5. In Sec. 5.6 we conclude and give an outlook on further improvements.

5.2 Two-body-sector

5.2.1 Theoretical framework

In the two-body sector we solve the LO non-pertubatively and we include the NLO and N2LO corrections perturbatively. For the free part of the Hamiltonian, we use an $O(a^4)$-improved version

$$H_{\text{free}} = \frac{1}{2m_N} \sum_{\vec{n},i,j} \Bigg\{ 2\omega_0 a^\dagger_{i,j}(\vec{n})\, a_{i,j}(\vec{n}) + \sum_{l=1}^{3} \sum_{\hat{s}} (-1)^k \omega_l \left[a^\dagger_{i,j}(\vec{n})\, a_{i,j}(\vec{n} + l\hat{s}) + a^\dagger_{i,j}(\vec{n})\, a_{i,j}(\vec{n} - l\hat{s}) \right] \Bigg\} . \tag{5.1}$$

The coefficients ω_l represent the improved action including a stretching factor which connects the $O(a^4)$ action with the $O(a^3)$ action to correct the dispersion relation of the nucleon-nucleon system. Explicitly we use

$$\begin{aligned} \omega_0 &= 10\left(\frac{49}{36} - \frac{5}{4}\right) + \frac{49}{36}, & \omega_1 &= 10\left(\frac{3}{2} - \frac{4}{3}\right) + \frac{3}{2}, \\ \omega_2 &= 10\left(\frac{3}{20} - \frac{1}{12}\right) + \frac{3}{20}, & \omega_3 &= 10\left(\frac{1}{90} - 0\right) + \frac{1}{90}. \end{aligned} \tag{5.2}$$

For a more detailed discussion on this, see Sec. 4.2. In the LO potential, we include smeared contact interaction operators which are projected on the S waves and the one-pion-exchange (OPE) potential. The short-range contact interaction reads

$$H_{\text{LO,contact}} = \sum_{\vec{n}_1,\vec{n}_2} f(\vec{n}_1 - \vec{n}_2) : \Bigg[c_0 \rho^{a^\dagger,a}(\vec{n}_1)\rho^{a^\dagger,a}(\vec{n}_2) + c_{ss} \sum_{S=1}^{3} \rho_S^{a^\dagger,a}(\vec{n}_1)\rho_S^{a^\dagger,a}(\vec{n}_2) + c_{ii} \sum_{I=1}^{3} \rho_I^{a^\dagger,a}(\vec{n}_1)\rho_I^{a^\dagger,a}(\vec{n}_2) + c_{si} \sum_{S,I=1}^{3} \rho_{S,I}^{a^\dagger,a}(\vec{n}_1)\rho_{S,I}^{a^\dagger,a}(\vec{n}_2) \Bigg] : \tag{5.3}$$

with

$$\begin{aligned} c_0 &= (3C_{^1S_0} + 3C_{^3S_1})/16\,, \; c_{ss} = (-3C_{^1S_0} + C_{^3S_1})/16\,, \\ c_{ii} &= (C_{^1S_0} - 3C_{^3S_1})/16\,, \quad c_{is} = (-C_{^1S_0} - C_{^3S_1})/16\,. \end{aligned} \tag{5.4}$$

$f(\vec{n})$ is the so-called smearing function, defined by

$$f(\vec{n}) = \mathcal{F}\left[f_0^{-1} \exp\left(-b\frac{\vec{q}^{\,4}}{4} \right) \right](\vec{n})\,, \tag{5.5}$$

with $\mathcal{F}$ denoting the Fourier transformation in the discrete space, and b is the smearing parameter. Furthermore, the normalization constant is given by $f_0 = \sum_{\vec{q}} \exp(-b\vec{q}^{\,4}/4)$. For the momentum-squared

discretization we use also an $O(a^4)$ improved one,

$$\vec{q}^{\,2} = 6\omega_0 + 2\sum_{l=1}^{3}\sum_{s=1}^{3}(-1)^n\omega_s \cos\left(\frac{2s\pi k_l}{L}\right). \tag{5.6}$$

As already argued in Ref. [32], this smearing improves the S wave description above a relative momentum of 50 MeV, and hence reduces the clustering instability for the few-body systems like ^{4}He. The long-range OPE is given by

$$H_{\rm OPE} = -\frac{g_A^2}{8F_\pi^2}\sum_{S_1,S_2,I}\sum_{n_1,n_2} G_{S_1,S_2}(\vec{n}_1-\vec{n}_2) : \rho^{a^\dagger,a}_{S_1,I}(\vec{n}_1)\,\rho^{a^\dagger,a}_{S_2,I}(\vec{n}_2) : \tag{5.7}$$

where the pion propagator is

$$G_{S_1,S_2}(\vec{q}) = \frac{q_{S_1}q_{S_2}}{M_\pi^2+\vec{q}^{\,2}} \tag{5.8}$$

with

$$q_S = \sin\left(\frac{2\pi k_S}{L}\right), \tag{5.9}$$

in momentum space. The pion mass is $M_\pi = 134.98$ MeV. For the pion-nucleon coupling constant and the pion decay constant, we use the values $g_A = 1.29$ (to account for the Goldberger-Treiman discrepancy) and $F_\pi = 92.2$ MeV. While there are various ways to regularize the long-range part with a Gaussian smearing function in momentum space or an analog function directly in position space [22], a similar analysis was done in Chapter 4 for the NLEFT approach where it was argued that the hard cut-off regularization due to lattice spacing is sufficient for the values of a we use in this chapter.

The NLO contact interaction contribution consists of ten terms totally. First, we have to include two operators which are not NLO operators by power counting but are necessary for accounting for the back-reaction of the NLO fits on the LO contribution. More precisely, for a coarse lattice spacing, these represent the full non-local structure of the TPEP [82] while for finer lattices they could be dropped. In addition, these additional terms assure that the NLO contributions can be treated perturbatively. Therefore, we keep them for consistency. These terms read,

$$V^1_{\rm NLO} = -\frac{\Delta C}{2} : \sum_{\vec{n}} \rho(\vec{n})\,\rho(\vec{n}) :, \tag{5.10}$$

$$V^2_{\rm NLO} = -\frac{\Delta C_{I^2}}{2} : \sum_{\vec{n}}\sum_{I=1}^{3} \rho_I(\vec{n})\,\rho_I(\vec{n}) : . \tag{5.11}$$

Then we have the seven standard NLO contact interactions,

$$V^3_{\rm NLO} = -\frac{C_{q^2}}{2} : \sum_{\vec{n}}\sum_{l=1}^{3} \rho(\vec{n})\,\nabla_l^2\rho(\vec{n}) :, \tag{5.12}$$

$$V^4_{\rm NLO} = -\frac{C_{I^2,q^2}}{2} : \sum_{\vec{n}}\sum_{I=1}^{3}\sum_{l=1}^{3} \rho_I(\vec{n})\,\nabla_l^2\rho_I(\vec{n}) :, \tag{5.13}$$

$$V^5_{\rm NLO} = -\frac{C_{S^2,q^2}}{2} : \sum_{\vec{n}}\sum_{S=1}^{3}\sum_{l=1}^{3} \rho_S(\vec{n})\,\nabla_l^2\rho_S(\vec{n}) :, \tag{5.14}$$

$$V^{6}_{\mathrm{NLO}} = -\frac{C_{S^2,I^2,q^2}}{2} : \sum_{\vec{n}} \sum_{S,I=1}^{3} \sum_{l=1}^{3} \rho_{S,I}(\vec{n}) \nabla_l^2 \rho_{S,I}(\vec{n}) :, \tag{5.15}$$

$$V^{7}_{\mathrm{NLO}} = \frac{C_{(q\cdot S)^2}}{2} : \sum_{\vec{n}} \sum_{S=1}^{3} \nabla_S \rho_S(\vec{n}) \sum_{S'=1}^{3} \nabla_{S'} \rho_{S'}(\vec{n}) :, \tag{5.16}$$

$$V^{8}_{\mathrm{NLO}} = \frac{C_{I^2,(q\cdot S)^2}}{2} : \sum_{\vec{n}} \sum_{S=1}^{3} \nabla_S \rho_{S,I}(\vec{n}) \sum_{S'=1}^{3} \nabla_{S'} \rho_{S'}(\vec{n}) :, \tag{5.17}$$

$$V^{9}_{\mathrm{NLO}} = -\frac{iC^{I=1}_{(q\times S)\cdot k}}{2} : \sum_{\vec{n}} \sum_{S=1}^{3} \sum_{l,l'=1}^{3} \varepsilon_{l,S,l'} \left[\Pi_l(\vec{n}) \nabla_{l'} \rho_S(\vec{n}) + \Pi_{l,S}(\vec{n}) \nabla_{l'} \rho(\vec{n}) \right] :, \tag{5.18}$$

with $\varepsilon_{a,b,c}$ the totally antisymmetric Levi-Civita tensor in three dimensions. Finally, we also include the following SO(3) breaking term

$$V^{10}_{\mathrm{NLO}} = \frac{C_{SO(3)}}{2} : \sum_{S} \rho_S(\vec{n}) \nabla_S^2 \rho_S(\vec{n}) :, \tag{5.19}$$

which allows us to remove lattice artefacts (unphysical partial wave mixing) due to rotational symmetry breaking. Rotational symmetry breaking is caused by the breakdown of the continuum SO(3) group to the SO(3, $\mathbb{Z}$), which consists of a finite number of irreducible representations and consequently allows a mixing of partial waves, which should not mix in the continuum. More details can be found in [33, 80, 82, 83, 132]. Specifically, this term is tuned to remove the mixing between the ${}^3S_1$-${}^3D_1$ and the ${}^3D_3$-${}^3G_3$ channels, but the physical mixing like e.g. ${}^3S_1$-${}^3D_1$ is of course not affected. Unphysical partial wave mixing in higher waves is so small that it can be ignored. More details of the notation can be found App. B.

At N2LO, there are no further contact terms. Further, we need to include the TPEP at NLO and N2LO. While they are largely absorbed in the NLO contact terms for a very coarse lattice, they play an important role for finer lattices [115]. At NLO, the TPEP reads

$$\begin{aligned} V^{\mathrm{TPEP}}_{\mathrm{NLO}} = \sum_{\vec{n}_1,\vec{n}_2} \Bigg\{ \sum_{I=1}^{3} -\frac{:\rho_I(\vec{n}_1)\rho_I(\vec{n}_2):}{384\pi^2 F_\pi^4} \Big[4M_\pi^2 \left(5g_A^4 - 4g_A^2 - 1\right) V^{\mathrm{TPEP},1}_{\mathrm{NLO}}(\vec{n}_1 - \vec{n}_2) \\ + \left(23g_A^4 - 10g_A^2 - 1\right) V^{\mathrm{TPEP},2}_{\mathrm{NLO}}(\vec{n}_1 - \vec{n}_2) + 48 g_A^4 M_\pi^4 V^{\mathrm{TPEP},3}_{\mathrm{NLO}}(\vec{n}_1 - \vec{n}_2) \Big] \\ - \frac{3g_A^4}{64\pi^2 F_\pi^4} \Bigg[: \sum_{S_1,S_2=1}^{3} V^{\mathrm{TPEP},4}_{\mathrm{NLO}}(\vec{n}_1 - \vec{n}_2, S_1, S_2) \rho_{S_1}(\vec{n}_1) \rho_{S_2}(\vec{n}_2) \\ - \sum_{S=1}^{3} V^{\mathrm{TPEP},2}_{\mathrm{NLO}}(\vec{n}_1 - \vec{n}_2) \rho_S(\vec{n}_1) \rho_S(\vec{n}_2) : \Bigg] \Bigg\} \end{aligned} \tag{5.20}$$

with the Fourier-transformed parts

$$V^{\mathrm{TPEP},1}_{\mathrm{NLO}}(\vec{n}) = \mathcal{F}\left[L(|\vec{q}|)\right](\vec{n}), \tag{5.21}$$

$$V^{\mathrm{TPEP},2}_{\mathrm{NLO}}(\vec{n}) = \mathcal{F}\left[L(|\vec{q}|)\,\vec{q}^{\,2}\right](\vec{n}), \tag{5.22}$$

$$V_{\mathrm{NLO}}^{\mathrm{TPEP},3}(\vec{n}) = \mathcal{F}\left[L(|\vec{q}|)\,\vec{q}^{\,2}\,\frac{1}{4M_\pi^2+\vec{q}^{\,2}}\right](\vec{n}), \tag{5.23}$$

$$V_{\mathrm{NLO}}^{TPEP,4}(\vec{n},S_1,S_2) = \mathcal{F}\left[L(|\vec{q}|)\,q_{S_1}q_{S_2}\right](\vec{n}), \tag{5.24}$$

where

$$L(q) = \frac{1}{2q}\sqrt{4M_\pi^2+q^2}\log\frac{\sqrt{4M_\pi^2+q^2}+q}{\sqrt{4M_\pi^2+q^2}-q}, \tag{5.25}$$

and $|\vec{q}| = \sqrt{\sum_{i=1}^{3} q_i^2}$. Note that this notation is different from Eq. (5.6), as the TPEP contributions should be absorbed in the NLO contact interaction up to $O(Q^2)$.

At N2LO, the TPE potential has a subleading contribution given by

$$\begin{aligned} V_{\mathrm{N2LO}}^{\mathrm{TPEP}} = \sum_{\vec{n}_1,\vec{n}_2}\Bigg\{ & -\frac{3g_A^2}{16\pi F_\pi^4}:\rho(\vec{n}_1)\rho(\vec{n}_2): \\ & \times\left[2M_\pi^2(2c_1-c_3)\,V_{\mathrm{N2LO}}^{\mathrm{TPEP},1}(\vec{n_1}-\vec{n}_2) - c_3 V_{\mathrm{N2LO}}^{\mathrm{TPEP},2}(\vec{n_1}-\vec{n}_2)\right] \\ & -\frac{g_A^4 c_4}{32\pi F_\pi^4}\Bigg[:\sum_{S_1,S_2=1}^{3}\rho_{S_1}(\vec{n}_1)\rho_{S_2}(\vec{n}_2)\,V_{\mathrm{N2LO}}^{\mathrm{TPEP},3}(\vec{n_1}-\vec{n}_2,S_1,S_2) \\ & -\sum_{S=1}^{3}\rho_S(\vec{n}_1)\rho_S(\vec{n}_2)\,V_{\mathrm{N2LO}}^{\mathrm{TPEP},4}(\vec{n_1}-\vec{n}_2):\Bigg]\Bigg\} \end{aligned} \tag{5.26}$$

with $c_1 = -1.10\ \mathrm{GeV}^{-1}$, $c_3 = -5.54\ \mathrm{GeV}^{-1}$ and $c_4 = 4.17\ \mathrm{GeV}^{-1}$ [46] and

$$A(q) = \frac{1}{2q}\arctan\frac{q}{2M_\pi} \tag{5.27}$$

with

$$V_{\mathrm{N2LO}}^{\mathrm{TPEP},1}(\vec{n}) = \mathcal{F}\left[A(|\vec{q}|)\left(2M_\pi^2+\vec{q}^{\,2}\right)\right](\vec{n}), \tag{5.28}$$

$$V_{\mathrm{N2LO}}^{\mathrm{TPEP},2}(\vec{n}) = \mathcal{F}\left[A(|\vec{q}|)\left(2M_\pi^2+\vec{q}^{\,2}\right)\vec{q}^{\,2}\right](\vec{n}), \tag{5.29}$$

$$V_{\mathrm{N2LO}}^{\mathrm{TPEP},3}(\vec{n},S_1,S_2) = \mathcal{F}\left[A(|\vec{q}|)\left(4M_\pi^2+\vec{q}^{\,2}\right)q_{S_1}q_{S_2}\right](\vec{n},S_1,S_2), \tag{5.30}$$

$$V_{\mathrm{N2LO}}^{\mathrm{TPEP},4}(\vec{n}) = \mathcal{F}\left[A(|\vec{q}|)\left(4M_\pi^2+\vec{q}^{\,2}\right)\vec{q}^{\,2}\right](\vec{n}). \tag{5.31}$$

Additionally, we also include corrections due to an improved version of the OPE and isospin-breaking effects due to the different pion masses. The correction caused by an improved discretization is given by

$$V_{\mathrm{Dx}} = -\frac{g_A^2}{8F_\pi^2}\sum_{S_1,S_2,I}\sum_{\vec{n}_1,\vec{n}_2}\left[\tilde{G}_{S_1,S_2}(\vec{n}_1-\vec{n}_2) - G_{S_1,S_2}(\vec{n}_1-\vec{n}_2)\right]:\rho_{S_1,I}^{a^\dagger,a}(\vec{n}_1)\rho_{S_2,I}^{a^\dagger,a}(\vec{n}_2):, \tag{5.32}$$

where the improved propagator is defined as

$$\tilde{G}_{S_1,S_2}(\vec{q}) = \frac{\tilde{q}_{S_1}\tilde{q}_{S_2}}{M_\pi^2+\vec{q}^{\,2}}, \tag{5.33}$$

with $\tilde{q}_S = (4/3)\sin(2\pi k/L) + (1/6)\sin(4\pi k/L)$ and $\vec{q}^{\,2}$ according to Eq. (5.6).
The isospin corrections caused by the pion mass differences are defined as

$$V_{\mathrm{IB}} = -\frac{g_A^2}{8F_\pi^2} \sum_{S_1,S_2,I} \sum_{\vec{n}_1,\vec{n}_2} \left[\bar{G}_{S_1,S_2}(\vec{n}_1 - \vec{n}_2) - G_{S_1,S_2}(\vec{n}_1 - \vec{n}_2)\right] : \rho^{a^\dagger,a}_{S_1,I}(\vec{n}_1)\rho^{a^\dagger,a}_{S_2,I}(\vec{n}_2) : \ . \tag{5.34}$$

The pion propagator with charged pions reads

$$\bar{G}_{S_1,S_2}(\vec{q}) = \frac{q_{S_1} q_{S_2}}{M_{\pi_\pm}^2 + \vec{q}^{\,2}}. \tag{5.35}$$

The charged pion mass is $M_\pm = 139.57$ MeV. Note that since isospin breaking is an NLO correction, we do not need to include the propagator discretization corrections analogous to Eqs. (5.32) and (5.33) for the charged pion propagator in Eq. (5.35). Hence, the complete $2N$ N2LO Hamiltonian reads

$$H^{2N}_{\mathrm{N2LO}} = \sum_{i=1}^{10} V^i_{\mathrm{NLO}} + V^{\mathrm{TPEP}}_{\mathrm{NLO}} + V^{\mathrm{TPEP}}_{\mathrm{N2LO}} + V_{\mathrm{Dx}} + V_{\mathrm{IB}} \tag{5.36}$$

As we want to describe light nuclei in a later stage, we also have to include Coulomb forces as well as proton-proton and neutron-neutron contact terms (for details, see Ref. [82]),

$$V^{\mathrm{Coul}} = \frac{\alpha_{\mathrm{EM}}}{2} \sum_{\vec{n}_1,\vec{n}_2} \frac{1}{\max\left(0.5, |\vec{n}_1 - \vec{n}_2|\right)} : \rho_p(\vec{n}_1)\rho_p(\vec{n}_2) : \ , \tag{5.37}$$

$$V^{pp} = \frac{C_{pp}}{2} \sum_n : \rho_p(\vec{n})\rho_p(\vec{n}) : \ , \tag{5.38}$$

$$V^{nn} = \frac{C_{nn}}{2} \sum_n : \rho_n(\vec{n})\rho_n(\vec{n}) : \ . \tag{5.39}$$

with α_{EM} the electromagnetic fine-structure constant and the projection densities are given in App. B. Thus, the complete electromagnetic contribution reads

$$V^{\mathrm{2N}}_{\mathrm{EM}} = V^{\mathrm{Coul}} + V^{pp} + V^{nn}. \tag{5.40}$$

The alert reader might notice that V^{pp} and V^{nn} are really strong isospin-breaking terms. We book them here, because V^{pp} is used to renormalize the Coulomb potential.

Now, the Hamiltonian is defined and, in the standard approach, we introduce a spherical wall boundary on the relative separation between nucleons in order to compute scattering phase shifts. This spherical wall is placed at radius R_{wall} outside the interaction region. We then solve for standing waves solutions of the transfer matrix [33]

$$: \exp\left[-\alpha_t \left(H_{\mathrm{free}} + H_{\mathrm{LO}}\right)\right] : \ |\Psi\rangle = \lambda\,|\Psi\rangle\,, \tag{5.41}$$

with $\alpha_t = a_t/a$ and the energy given by

$$E = -\frac{\log(\lambda)}{\alpha_t}\ . \tag{5.42}$$

The solutions must be identified with the correct partial wave, then one could use the energy shift between the free and interacting system to calculate the phase shifts [61]. The NLO and N2LO energy corrections are implemented perturbatively just by calculating the corresponding matrix element. In what follows,

we utilize a more sophisticated procedure: Using the radial projection method we impose a spherical wall, but we first project the system onto its partial waves where the only degree of freedom is the radial one. This projection accelerates the fit procedures and is necessary particularly in the case of small lattice spacings. Then the basis turns from a three-dimensional vector $|\vec{R}\rangle$ to a radial basis $|R\rangle^{l,l_z}$:

$$|R\rangle^{l,l_z} = \sum_{\vec{R}'} Y_{l,l_z}(\hat{R}')\delta_{R,R'} \left|\vec{R}'\right\rangle . \tag{5.43}$$

Here, the Y_{l,l_z} are the spherical harmonics specified by their angular momentum l, l_z. Consequently, all operators are projected to a radial basis, too,

$$O(\vec{R}) \to O(R) , \tag{5.44}$$

and the problem can be solved completely in the reduced basis analogous to Eqs. (5.41,5.42). Details of the method can be found in Refs. [83, 133] where the projection, the binning, the new radial metric and the extraction method for coupled channels are explained. In an uncoupled channel, the projected radial wave function solution $\psi_l^p(r)$ can be directly identified with the spherical Bessel functions in a region between the interaction region and the spherical wall, which we confine to be between R_{in} and R_{out}. Thus, the phase shift δ_l can be read off immediately,

$$\psi_l^p(r) = \mathcal{N}^p \left[\cot(\delta_l)\, j_l(pr) + n_l(pr)\right] , \tag{5.45}$$

where p is the relative momentum, $\mathcal{N}^p$ a normalization constant and $j_l(pr)$ and $n_l(pr)$ the spherical Bessel functions of first and second kind. For the perturbative energy corrections, we have to use the projected potentials and the new phase shifts are calculated using the energy shifts according to Ref. [61]. For the lattice spacing of $a = 1.97$ fm we use $L = 32$ [l.u.], $R_{\text{wall}} = 14.02$ [l.u.], $R_{\text{in}} = 9.02$ and $R_{\text{out}} = 12.02$ [l.u.]. For the smaller lattice spacings, we use the same values for these parameters in physical units (fm). For the neutron-proton fit procedure we follow Ref. [116]. In general, we do a χ^2 fit to partial wave analysis data PWA, NijmI, NijmII and Reid93 of [134] according to [22],

$$\chi^2 = \sum_i \frac{\left(\delta_i - \delta_i^{\text{PWA}}\right)^2}{\Delta_i^2} \tag{5.46}$$

where the error is defined as $\Delta_i = \max[\Delta_i^{\text{PWA}}, |\delta_i^{\text{NijmI}} - \delta_i^{\text{PWA}}|, |\delta_i^{\text{NijmII}} - \delta_i^{\text{PWA}}|, |\delta_i^{\text{Reid93}} - \delta_i^{\text{PWA}}|]$. Further details on errors and error propagation can be found in App. C. At LO we fit the LECs $C_{^1S_0}$ and $C_{^3S_1}$ to the $^1S_0$ and $^3S_1$ channel up to 100 MeV, and we keep the smearing parameter b fixed at $b = 0.07$. While we could use it as a fit parameter as well for the coarse lattice, it will cause some problem for small lattice spacing. As one can see in Ref. [116], most of the partial waves are better described with smaller lattice spacing except for the $^1S_0$ channel which becomes too strong. The reason is that the LO smearing parameter is mainly determined by the $^3S_1$ channel due to the different errors in the PWA analysis. This effect is negligible for large lattice spacings but becomes sizable for smaller ones and worsens the prediction of the $^1S_0$ wave. Hence, we keep the smearing parameter close to the fit value for $a = 1.97$ fm and all corrections are done by NLO and N2LO insertions.

Once the LO is fixed, we include isospin-breaking effects, the improved description of the OPEP, the TPEP at NLO and N2LO as well as the NLO contact terms. We fit all remaining coefficients to S and P waves up to 150 MeV momentum as well as the deuteron binding energy. Afterwards we fit the proton-proton interaction term to the pp $^1S_0$ phase shift and the neutron-neutron interaction term to the

Table 5.1: Summary of fit results with perturbatively improved OPE (in units of a) for the perturbative NLO+NNLO analysis at $a = 1.97$ fm. All LECs are given in lattice units: $C_{^1S_0}$,$C_{^3S_1}$,ΔC,ΔC_{I^2},C_{nn},C_{pp} are multiplied with a^2, while the rest is multiplied with a^4.

	$a = 1.97$ fm	$a = 1.64$ fm	$a = 1.32$ fm
$C_{^1S_0}$	−0.421(2)	−0.370(4)	−0.289(3)
$C_{^3S_1}$	−0.603(2)	−0.549(3)	−0.424(3)
ΔC	−0.2(2)	0.4(3)	−0.5(2)
ΔC_{I^2}	−0.0(1)	−0.0(1)	−0.08(9)
C_{q^2}	−0.05(6)	0.10(8)	0.45(6)
C_{I^2,q^2}	−0.06(3)	0.13(4)	0.27(4)
C_{S^2,q^2}	−0.00(7)	−0.0(1)	0.00(5)
C_{S^2,I^2,q^2}	−0.01(5)	0.0(1)	−0.10(3)
$C_{(q\cdot S)^2}$	0.00(8)	−0.0(0)	0.05(3)
$C_{I^2,(q\cdot S)^2}$	0.02(8)	0.2(1)	0.20(3)
$C^{I=1}_{(q\times S)\cdot k}$	0.033(6)	0.04(1)	0.09(1)
$C_{SO(3)}$	0.1(1)	1(1)	−0.5(1)
C_{nn}	0.01(4)	0.02(5)	0.04(5)
C_{pp}	0.003(1)	0.003(1)	0.008(3)
E_{LO} [MeV]	−2.20(4)	−2.42(8)	−2.6(1)

nn scattering length of $a_{nn} = 18(1)$ fm. Due to the long-range nature of the Coulomb force we include it non-perturbatively in the pp channel and change the Bessel functions with the respective Coulomb ones [115], namely $j_l(pr)$ by $F_l(\eta, pr)$ and $n_l(pr)$ by $G_l(\eta, pr)$, where $\eta = \alpha_{\mathrm{EM}} m/(2p)$ and

$$F_l(\eta, pr) = (pr)^{l+1} \exp(-ipr) c_l(\eta) {}_1F_1(l + 1 - i\eta, 2l + 2, 2ipr), \tag{5.47}$$

$$G_l(\eta, pr) = \frac{(2i)^{2l+1}(pr)^{l+1} \exp(-ipr)\Gamma(l + 1 - i\eta)}{\Gamma(2l + 2)c_l(\eta)} U(l + 1 - i\eta, 2l + 2, 2ipr) + iF_l(\eta, pr), \tag{5.48}$$

with ${}_1F_1$ and U the Kummer functions of the first and second kind while c_l is defined as

$$c_l(\eta) = \frac{2^l \exp(-\pi\eta/2)|\Gamma(l + 1 + i\eta)|}{\Gamma(2l + 2)}. \tag{5.49}$$

However, the contact interaction V_{pp} is included perturbatively as all other higher-order operators.

5.2.2 Results

The results for np scattering can be found in Figs. 5.1,5.2,5.3, and the pp scattering results are shown in Fig. 5.4. The corresponding LECs are summarized in Tab. 5.1.

When we compare the LO results for the various lattice spacings, we see that the ${}^1S_0$ phase shift is

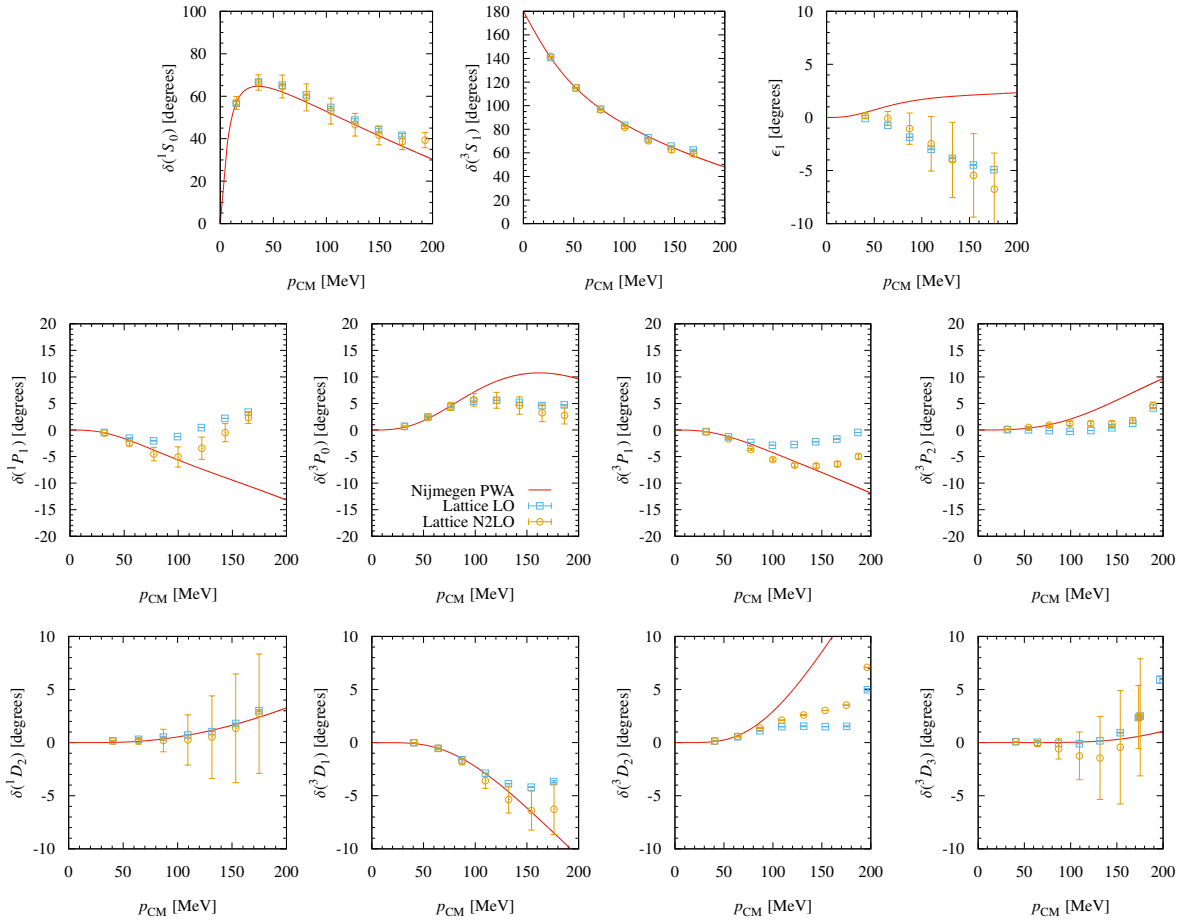

Figure 5.1: LO (squares) and NNLO (circles) neutron-proton phase shifts and mixing angles for $a = 1.97$ fm. The Nijmegen partial wave analysis (NPWA) is given by the solid line.

too strong already at 70 MeV while the description of the $^3S_1$ phase shift is quite accurate even beyond the fit range of 100 MeV, but the best description is for $a = 1.64$ fm instead of $a = 1.32$ fm. The reason is that the smearing constant b is fixed instead of a fit parameter which results also in a fixed shape of the $^3S_1$ phase shift. The calculated P wave phase shifts are in agreement with the PWA phase shifts roughly up to 80 MeV for $a = 1.97$ fm and the description improves with smaller lattice spacing. As the only influence is from the OPE, this does not come as a surprise as the simplified description of the OPE numerator approaches more and more the exact one with smaller lattice spacings. Also the D wave description at LO improves significantly, e.g. the $^3D_1$ channel description is quite fine up to 80 MeV for the coarse lattice while it is quite good up to 170 MeV for the fine lattice. At N2LO the general description improves as the fit range is extended up to 150 MeV and also the P waves as well as the deuteron binding energy is included. This improvement can be seen particularly in the $^1S_0$ channel where the phase shift moves closer to the PWA analysis and $^1P_1$ where the agreement range is extended by 40 MeV. Comparing the different lattice spacings, one sees again a clear improvement particularly for the P waves which are now described up to the fit range of 150 MeV. In D waves for the smallest lattice spacing we still have some small deviations at least for the $^1D_2$ channel as well as the $^3D_3$ channel which would be fixed by the inclusion of N3LO corrections.

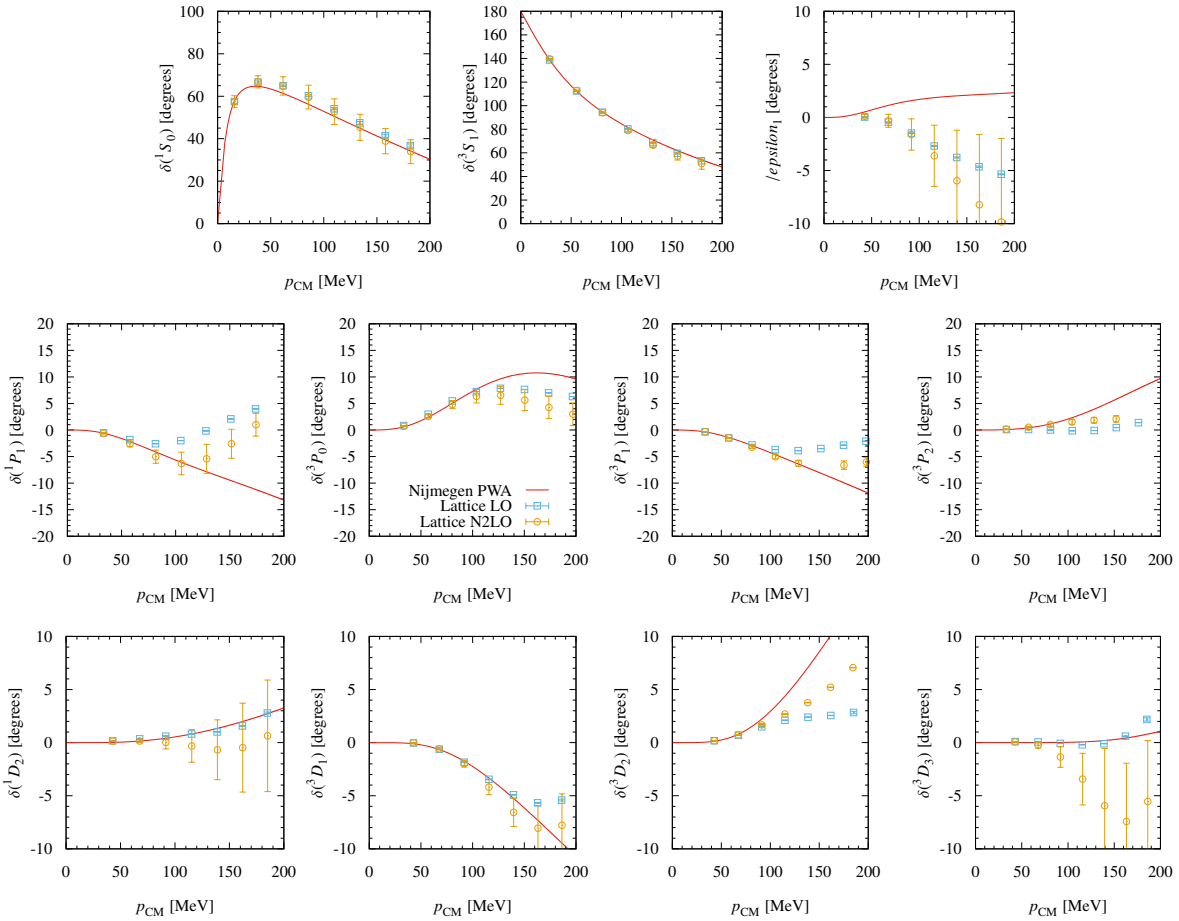

Figure 5.2: LO (squares) and NNLO (circles) neutron-proton phase shifts and mixing angles for $a = 1.64$ fm. The NPWA is given by the solid line.

Having a closer look at the $pp\ ^1S_0$ phase shift one sees that the phase shift is too large for $a = 1.97$ fm particularly for high energies. While the phase shift becomes smaller and finally too small with finer lattices at LO, the N2LO phase shifts is getting more and more close to the NPWA phase shift in the whole momentum region from 0 to 200 MeV.

5.3 Three-body sector

In the three-body sector we only have to consider the triton. Its experimental binding energy is given by $E_{^3\mathrm{H}} = -8.4820(1)$ MeV.

5.3.1 Theoretical framework

Although we work in the three-body sector, we are still able to do an exact calculation using the Lanczos method. Therefore we extend the former analysis of the $2N$ sector to the triton, which means that we cannot work in radial coordinates anymore but we calculate the spectrum in a cubic box. In addition to two-body forces we include three-body potentials, which were reviewed in [115]. They consist of a

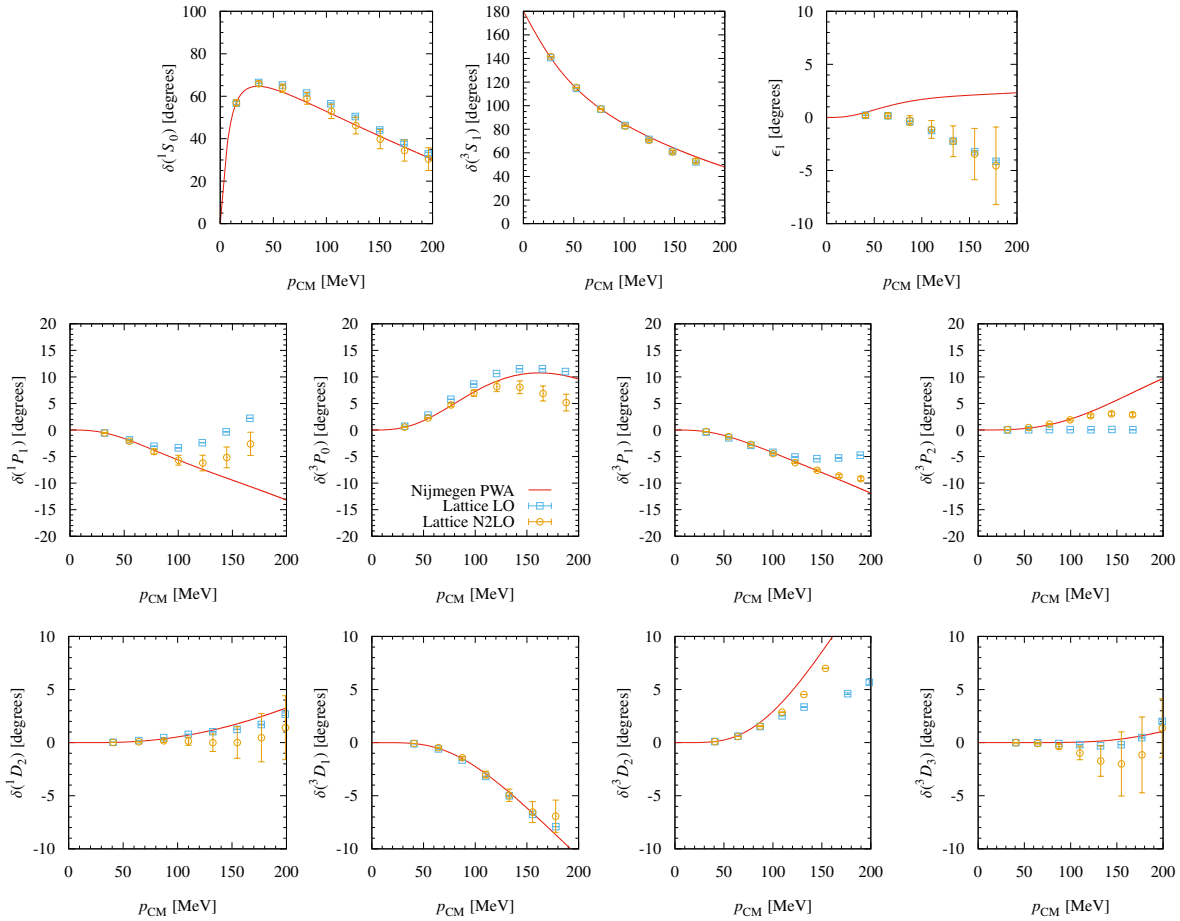

Figure 5.3: LO (squares) and NNLO (circles) neutron-proton phase shifts and mixing angles for $a = 1.32$ fm. The NPWA is given by the solid line.

three-body contact interaction, a one- and a two-pion exchange interaction. These terms are

$$V^{3N}_{\rm contact} = D^{\rm 3N}_{\rm contact} \sum_{\vec{n}} : \rho(\vec{n})\rho(\vec{n})\rho(\vec{n}) : \ , \tag{5.50}$$

$$V^{3N}_{\rm OPE} = -D^{\rm 3N}_{\rm OPE} \sum_{\vec{n}_1,S_1,\vec{n}_2,S_2,I} \left[G_{S_1,S_2}(\vec{n}_1-\vec{n}_2) \times : \rho_{S_1,I}(\vec{n}_1)\rho_{S_2,I}(\vec{n}_2)\rho(\vec{n}_2) : \right] , \tag{5.51}$$

$$V^{3N}_{\rm TPE} = V^{3N}_{{\rm TPE},m^2} + V^{3N}_{{\rm TPE},p^2} + V^{3N}_{\rm TPE,xx}. \tag{5.52}$$

The latter equation describing the TPEP among three particles can be split up into three parts which read

$$V^{3N}_{{\rm TPE},q^2} = D^{3N}_{q^2} \sum_{\substack{\vec{n}_1,S_1,\vec{n}_2,S_2,\\ \vec{n}_3,S_3,I}} \left[G_{S_1,S_3}(\vec{n}_1-\vec{n}_3) G_{S_2,S_3}(\vec{n}_2-\vec{n}_3) : \rho_{S_1,I}(\vec{n}_1)\rho_{S_2,I}(\vec{n}_2)\rho(\vec{n}_3) : \right] , \tag{5.53}$$

$$V^{3N}_{{\rm TPE},m^2} = D^{3N}_{m^2} \sum_{\vec{n}_1,S_1,\vec{n}_2,S_2,\vec{n}_3,I} \left[G_{S_1}(\vec{n}_1-\vec{n}_3) G_{S_2}(\vec{n}_2-\vec{n}_3) : \rho_{S_1,I}(\vec{n}_1)\rho_{S_2,I}(\vec{n}_2)\rho(\vec{n}_3) : \right] , \tag{5.54}$$

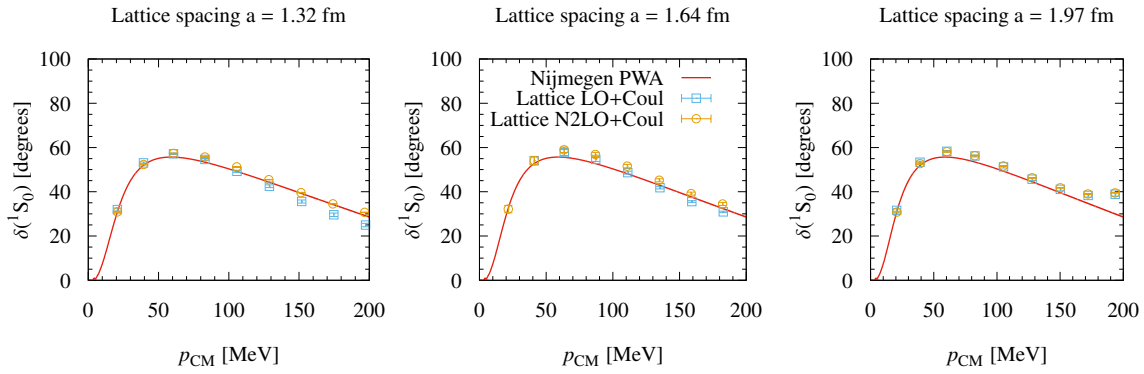

Figure 5.4: LO (squares) and NNLO (circles) (both including Coulomb) proton-proton $^1S_0$ phase shift for $a = 1.97$ fm, $a = 1.64$ fm and $a = 1.32$ fm. The NPWA is given by the solid line.

$$V^{3N}_{\mathrm{TPE,xx}} = D^{3N}_{xx} \sum_{\substack{\vec{n_3},\tilde{S}_1,\tilde{S}_2,\tilde{S}_3,I_1,I_2,\\ I_3,\vec{n}_2,S_2,\vec{n}_3,S_3}} \Big[G_{S_1,\tilde{s}_1}(\vec{n}_1-\vec{n}_3)\, G_{S_2,\tilde{s}_2}(\vec{n}_2-\vec{n}_3)\, \epsilon_{\tilde{s}_1,\tilde{s}_2,\tilde{s}_3}\epsilon_{I_1,I_2,I_3} \times{:}\, \rho_{S_1,I_1}(\vec{n}_1)\rho_{S_2,I_2}(\vec{n}_2)\rho_{\tilde{S}_3,I_3}(\vec{n}_3) \,{:}\, \Big] , \tag{5.55}$$

where the coefficients are

$$\begin{aligned} D^{3N}_{\mathrm{contact}} &= \frac{-3c_E}{F_\pi^4\Lambda}, & D^{3N}_{\mathrm{OPE}} &= \frac{c_D}{4F_\pi^3\Lambda}\frac{g_A}{2F_\pi}, \\ D^{3N}_{q^2} &= \frac{c_3}{F_\pi^2}\frac{g_A^2}{4F_\pi^2}, & D^{3N}_{m^2} &= \frac{-2c_1}{F_\pi^2}\frac{M_\pi^2 g_A^2}{4F_\pi^2}, \\ D^{3N}_{xx} &= \frac{c_4}{2F_\pi^2}\frac{g_A^2}{4F_\pi^2}, \end{aligned} \tag{5.56}$$

with $\Lambda = 700$ MeV as the reference scale. There are two new dimensionless parameters c_D and c_E which must be determined using at least two three-body observables. While we use the well-measured triton binding energy as one parameter, it was summarized in Ref. [115] that c_D and c_E could be disentangled by additionally including of nucleon-deuteron scattering, triton beta decays or some other observable in the analysis. As this is beyond the scope of this work, we keep the correlation between c_D and c_E and we fix $c_D = -0.79$ as it was shown to be of $O(1)$. Hence, we use c_E as the only fit parameter and fix it with the triton binding energy of $E_B^{^3\mathrm{H}} = -8.4820(1)$ MeV. In the subsequent part of this chapter we also have a look on systematic errors due to this particular choice of c_D. Of course, there are better ways of fixing c_D by now, but for the sake of consistency we have to use the same method that was employed in earlier NLEFT calculations

As we are interested in the binding energy of the system, we have to calculate the ground state at large enough volume or do an infinite volume extrapolation for a three-particle system. Using a box volume of $V \approx (10 \cdot 1.97\ \mathrm{fm})^3 \approx (12 \cdot 1.64\ \mathrm{fm})^3 \approx (20\ \mathrm{fm})^3$ for the two coarsest lattices is enough for neglecting the finite volume effects and it is still calculable with in a reasonable amount of computational resources. Unfortunately, this volume is not computable with the given resources anymore for a lattice spacing of $a = 1.32$ fm as the problem scales $\propto L^6$. Finite volume binding energy corrections for three particles

were calculated in the unitary limit as well as the shallow binding of one particle to a deeply bound dimer in Refs. [87, 88, 90]. While the triton is a system between these two limits, the numerical difference between the two calculations is negligible once the volume is chosen large enough. Hence, we do an infinite volume extrapolation using the LO formula in the unitary limit given by

$$E^{3N}(L) = E_{\infty}^{3N} + \mathcal{A}\frac{\exp\left(\frac{2\kappa L}{\sqrt{3}}\right)}{(\kappa L)^{\frac{3}{2}}}, \tag{5.57}$$

where $\kappa = \sqrt{-mE_{\infty}^{3N}}$. We use all data points for $L = 10$ [l.u.] and larger as for smaller lattices the NLO contributions of the finite volume corrections become significant. Afterwards, we fit each perturbative higher-order operator $\langle O_i \rangle$ according to

$$\langle O_i \rangle(L) = \langle O_i \rangle_{\infty} + \mathcal{A}_i\frac{\exp\left(\frac{2\kappa L}{\sqrt{3}}\right)}{(\kappa L)^{\frac{3}{2}}}. \tag{5.58}$$

5.3.2 Results

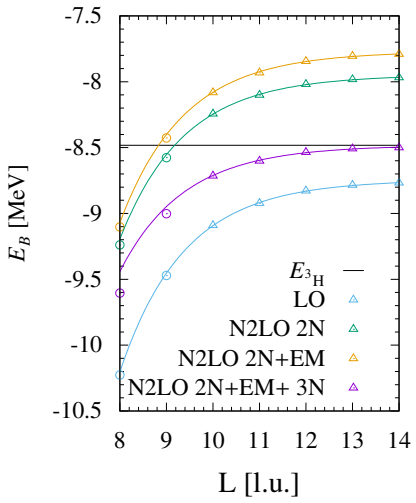

Figure 5.5: Infinite volume extrapolation for the triton and a lattice spacing of $a = 1.32$ fm. The triangles are included in the fit while the circles are not due to higher order finite volume effects.

The extrapolation is plotted in Fig. 5.5 where one can see excellent agreement with the data points. The fit quality also makes it unnecessary to include higher order corrections or use other methods like twisted mass boundary conditions to further pin down the infinite volume binding energy [135]. The results for the various lattice spacings are summarized in Tab. 5.2. Focusing on the LO, one sees an underbinding at LO of only -7.80 MeV for $a = 1.97$ fm, an almost perfect binding energy of -8.29 MeV for $a = 1.64$ fm, and an overbinding of -8.74 MeV for the smallest lattice spacing of $a = 1.32$ fm. By comparing these results with the neutron-proton phase shifts, one can attribute this mainly to the $^3P_0$ phase shift where one has a strong shift from its underestimation of it at the coarse lattice spacing to its overestimation at the fine one. At N2LO, the binding energy varies around 8 MeV. In particular, the triton

Table 5.2: Triton binding energy predictions at LO, N2LO, N2LO+EM, N2LO+EM+3NF and the fit parameter c_D. The energy errors in brackets are due to the uncertainties of the LECs. The * denotes the triton binding energy as an input parameter.

	$a = 1.97$ fm	$a = 1.64$ fm	$a = 1.32$ fm
E_{LO} [MeV]	−7.80	−8.29	−8.74
E_{N2LO} [MeV]	−7.846(4)	−8.11(2)	−7.95(2)
$E_{\mathrm{N2LO}}^{+\mathrm{EM}}$ [MeV]	−7.68(2)	−7.91(3)	−7.77(2)
$E_{\mathrm{N2LO}}^{+\mathrm{EM+3N}\star}$ [MeV]	−8.48(3)	−8.48(3)	−8.48(2)
c_E	0.5309(2)	0.3854(3)	1.0386(5)

becomes less bound as a is decreased from $a = 1.64$ fm to $a = 1.32$ fm even though the $^3P_0$ prediction is stronger. The reason is that the difference between the $^3P_0$ phase shifts is relatively small and the $^1S_0$ as well as the $^3P_1$ phase shifts become smaller and finally have a larger effect on the three-particle binding energy. The fit value for c_E is of natural size and its pattern is consistent with the missing attraction at N2LO+EM.

5.4 Four-body sector

5.4.1 Theoretical framework

In the four-body system, we do not have any new operator as our system should be describable by the 2NFs and 3NFs only. As the four-body system scales with L^9, an exact calculation at sufficient large lattices is not practical anymore, and hence we have to use Monte Carlo methods. More precisely, we use auxiliary field Monte Carlo with the hybrid Monte Carlo algorithm [33]. In the following we will define the LO auxiliary field transfer matrix which we will minimize afterwards. All other contributions are calculated perturbatively. For an increased convergence we prepare our trial states using a SU(4) symmetric Hamiltonian

$$H_0 = H_{\mathrm{free}} + \frac{1}{2} C_0 \sum_{\vec{n}_1,\vec{n}_2} f_{\mathrm{SU(4)}}(\vec{n}_1 - \vec{n}_2)\,\rho(\vec{n}_1)\,\rho(\vec{n}_2)\,, \tag{5.59}$$

with $f_{\mathrm{SU(4)}}(\vec{n}_1 - \vec{n}_2)$ a Gaussian smearing function. This operator is used to efficiently create trial states which are close to realistic nuclei,

$$\left|\psi_{^4\mathrm{He}}\right\rangle = \exp\left(-t_0 H_0\right)\left|\psi_0\right\rangle, \tag{5.60}$$

where $|\psi_0\rangle$ is the antisymmetrized free-particle solution for ^{4}He in a finite volume. The correlation function at Euklidean time t is defined as

$$Z_{^4\mathrm{He}}(t) = \left\langle \psi_{^4\mathrm{He}} \mid \exp(-tH_{\mathrm{LO}}) \mid \psi_{^4\mathrm{He}} \right\rangle\,, \tag{5.61}$$

where $H_{\mathrm{LO}} = H_{\mathrm{free}} + H_{\mathrm{LO,contact}} + H_{\mathrm{OPE}}$ is the full LO Hamiltonian according to Eqs. (5.1,5.3,5.7), and $|\psi_{^4\mathrm{He}}\rangle$ is the antisymmetrized wave function of the nucleons given by Eq. (5.61). The above-mentioned expression can be calculated using auxiliary field Monte Carlo methods for different time steps and the

corresponding energy is given by

$$E_{\mathrm{LO}}(t) = -\frac{d \log Z_{^4\mathrm{He}}(t)}{dt}. \tag{5.62}$$

The correlation function for any perturbative operator O is defined by

$$Z_O(t) = \left\langle \psi_{^4\mathrm{He}} \left| \exp\left(\frac{-tH}{2}\right) O \exp\left(\frac{-tH}{2}\right) \right| \psi_{^4\mathrm{He}} \right\rangle, \tag{5.63}$$

and their expectation value is given by the ratio

$$\langle O \rangle(t) = \frac{Z_O(t)}{Z_{^4\mathrm{He}}(t)}. \tag{5.64}$$

The ground state energy is calculated by performing the Euclidean time extrapolation to the infinity. Note that for the calculation of the ground state energy and the perturbative insertions, it is necessary to use the wave function of neighboring and next-to-neighboring time-slices. While the neighboring time slices do not suffer from correlations, the next-to-neighboring time-slices may do. Therefore we fit LO, additional $2N$ N2LO, additional $2N$ electromagnetic and additional $2N$ N2LO contribution separately with one or two exponential functions depending on the contribution and sum them up finally,

$$E_O(t) = E_{0,O} + c_1 \exp\left(-\Delta E_{1,O} t\right) \quad \left[+c_2 \exp\left(-\Delta E_{2,O} t\right)\right]. \tag{5.65}$$

The necessity of two or even more exponentials for the extrapolation of perturbative operators was already shown in [108], where an analysis with particular emphasis on the infinite time extrapolation was done. In the following we do a benchmark calculation for $L = 4$ and $a = 1.97$ fm which we can compare with an exact Lanczos calculation. Then we do the calculation for $L = 6$ and $a = 1.97$ fm, $L = 7$ and $a = 1.64$ fm and $L = 9$ and $a = 1.32$ fm. The physical box length is between 11 fm and 12 fm, and it is large enough that finite volume errors will be within truncation errors due to chiral expansion and uncertainties in the respective low-energy coupling constants (LECs).

5.4.2 Results

First of all, we start with the benchmark calculation. The results are shown in Tab. 5.3. One can see very good agreement particularly for the LO result which is around one per mille relative error. The difference for the perturbative corrections is larger but still below 10 % which is finally within the error bars of the infinite time LO extrapolation. Even though the accuracy will go down with larger volumes due to the sign problem, we do expect trustable results within our estimated errors. The infinite time extrapolation order by order for the three lattice spacings are shown in Figs. 5.6, 5.7 and 5.8 while the summed binding energy predictions are shown in Tab. 5.4. First, one can see very good time extrapolation order by order for all three lattice spacings. While the statistical errors at LO are below 1%, the perturbative relative errors are around 3% except for the N2LO contribution for $a = 1.32$ fm where the error is much larger. This is caused by relatively bad statistics of the data points due to the very difficult calculations of large lattices. As the higher-order contributions are quite small, their error due to statistical uncertainties as well as uncertainties in the LECs are dominated by the LO statistical uncertainties as shown in Tab. 5.4. As mentioned in Sec. 5.3, there is some ambiguity in the determination of c_D and c_E where c_D is of $O(1)$. Therefore, we fit c_E for different values of c_D, namely $-2 \leq c_D \leq 2$. The difference in the ^{4}He binding energy comes out very small, $\Delta E^{^4\mathrm{He}}_{c_D - c_E} \approx 0.2$ MeV. This systematic error is compatible with the errors caused by statistics as well as the uncertainties of the NLO and N2LO LECs.

Table 5.3: ^{4}He benchmark calculation for $a = 1.97$ fm and $L = 4$. The first bracket of Monte Carlo error are statistical ones, while the latter ones and the Lanczos ones are errors due to uncertainties of the LECs.

	Monte Carlo	Lanczos
E_{LO} [MeV]	−30.32(2)(1)	−30.34
ΔE_{N2LO} [MeV]	0.511(9)(10)	0.52(2)
ΔE_{EM} [MeV]	0.86(4)(2)	0.91(3)
$\Delta E_{\mathrm{3NNLO}}$ [MeV]	−5.1223(1128)(5)	−5.0278(5)

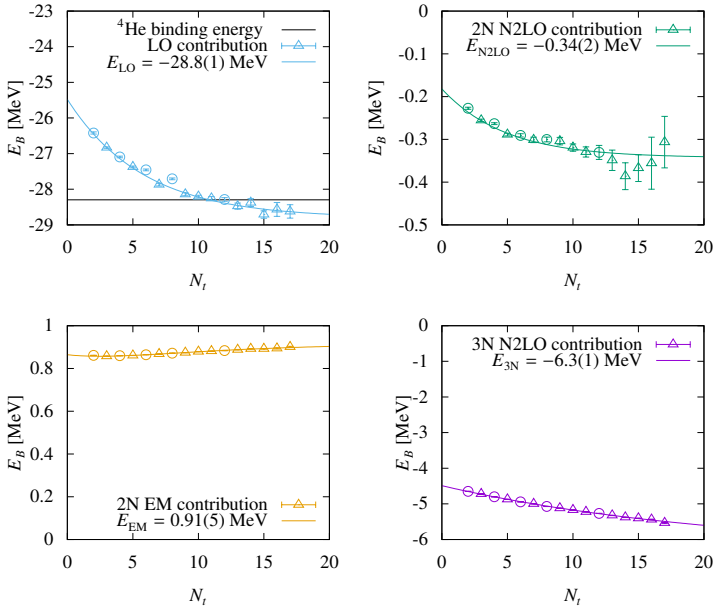

Figure 5.6: ^{4}He time extrapolation for lattice spacing of $a = 1.97$ fm. The triangles are included in the fit while the circles are excluded due to statistics. See Sec. 3.7 for details.

5.5 The Tjon band

5.5.1 Theoretical framework

The correlation between the ^{3}H and ^{4}He binding energies was first observed by Tjon [24] for a large class of 2N potentials of different accuracy. This was later dubbed the Tjon line. It was shown in Refs. [70, 71, 136] that this correlation still holds in the case of modern, accurate semi-phenomenological potentials as well as nuclear effectice field theory. In Ref. [72] this correlation was studied in the framework of pionless effective field theory, where the only input parameters are the singlet and triplet neutron-proton scattering lengths as well as the deuteron binding energy E_d. In this study, also a range of correlation is given by calculating it either with $a_{^1S_0}$ and $a_{^3S_1}$ scattering lengths as input parameters or with $a_{^1S_0}$ and E_d as input parameters. In this way, the so-called Tjon band is generated. In Fig. 5.9 the upper bound is due to the first fit while the lower bound is due to the latter one. A similar analysis using resonating group techniques in the framework of pionless EFT was done in Ref. [73]. However, in NLEFT a general

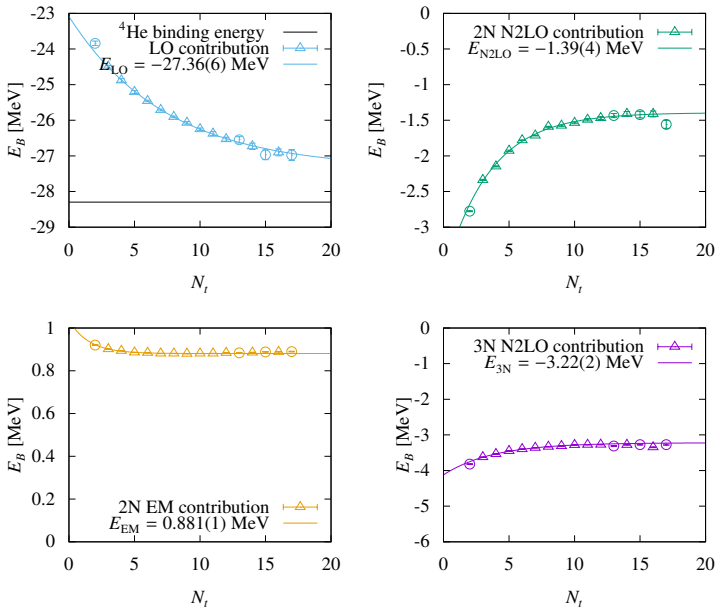

Figure 5.7: ^{4}He time extrapolation for lattice spacing of $a = 1.64$ fm. The triangles are included in the fit while the circles are excluded due to statistics. See Sec. 3.7 for details.

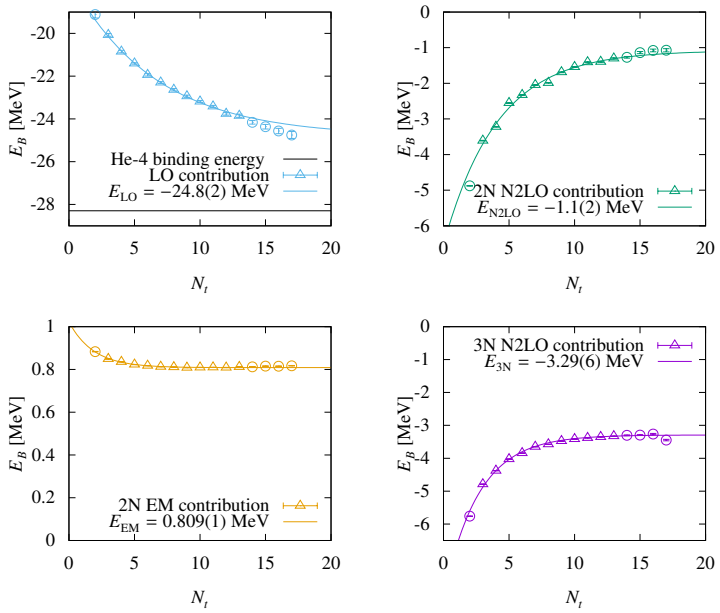

Figure 5.8: ^{4}He time extrapolation for lattice spacing of $a = 1.32$ fm. The triangles are included in the fit while the circles are excluded due to statistics. See Sec. 3.7 for details.

overbinding was observed [108, 115] in the case of a very coarse lattice of $a = 1.97$ fm. This overbinding was systematically absorbed in an effective four-body contact interaction which was fitted to the binding

Table 5.4: ^{4}He binding energy prediction at LO, N2LO, N2LO+EM, N2LO+EM+3N. The first brackets give the statistical error while the latter ones give the errors due to uncertainties of the LECs. All binding energies are given in MeV.

	$a = 1.97$ fm	$a = 1.64$ fm	$a = 1.32$ fm
E_{LO}	−28.81(11)	−27.36(6)	−24.81(19)
E_{N2LO}	−29.15(11)(3)	−28.75(7)(5)	−25.89(27)(3)
$E_{\mathrm{N2LO}}^{+\mathrm{EM}}$	−28.23(12)(3)	−27.87(7)(6)	−25.08(27)(3)
$E_{\mathrm{N2LO}}^{+\mathrm{EM+3N}}$	−34.55(18)(3)	−31.09(7)(6)	−28.37(28)(3)

energy of the alpha-cluster nucleus ^{24}Mg. It was argued that this overbinding is a lattice arfefact which is caused by an implicit 4NF due to the superposition of four particles at the same space point. In general, this contribution is negligible in the continuum, but due to the binning of the wave function over the lattice point volume, this contribution may become unphysically large and result in very deep bound states. This was shown explicitly in two dimensions in Ref. [128] and it should vanish once the lattice spacing is small enough.

5.5.2 Results

The results for the binding energy of triton and ^{4}He in the previous sections are combined and shown in Fig. 5.9. For the standard coarse lattice spacing of $a = 1.97$ fm already the LO is above the Tjon line as ^{3}H is approximately 1 MeV underbound or ^{4}He is approximately 2.5 MeV overbound. The data points for $2N$ N2LO are close the LO data point as there is not very much difference in the np phase shift shown in Fig. 5.1 as well. Including the $2N$ EM interaction results in a data point closer to the Tjon line but still around 2 MeV above. However, the inclusion of $3N$ N2LO contributions results in a very large overbinding of approximately 6 MeV. For the next lattice spacing of $a = 1.64$ fm the results already get improved as the LO data point is already on the Tjon band and the N2LO/ N2LO+EM correction is closer to the band as well but still above. After the inclusion of the $3N$ forces, the overbinding of ^{4}He is only 2.5 MeV for $a = 1.64$ fm. In the case of the finest lattice spacing of $a = 1.32$ fm, the LO triton binding energy is approximately overbound by 0.3 MeV while the ^{4}He binding energy is roughly 4 MeV underbound. The respective ^{4}He-^{3}H data point is now below the Tjon line which does not come as a surprise. The reason is that for a good description within the Tjon band it is necessary to have a very good description of the $^1S_0$, $^3S_1$ phase shifts and the deuteron binding energy. By comparing the LO deuteron binding energies summarized in Tab. 5.1 one can see an appearing overbinding for smaller lattice spacings. Such a overbinding should lead to a decrease of the Tjon band towards the measured ^{3}H-^{4}He energy. Once higher orders are included the binding energy is fixed and the results are within the Tjon band around −7.95 MeV for the triton and −25 MeV for ^{4}He. The electromagnetic contributions shift the data point, but it is still almost in the center of the Tjon band. After including the 3NF, the triton energy is at the physical point and the ^{4}He energy is −28.37(28) MeV within the Tjon band. This means that all lattice artefacts are systematically removed, and one can reproduce the correlation between the three- and a four-body system for NLEFT. As the physical point is already within the error bands, one would need more statistical improvement as this is the main error source. Then one can observe the influence of other remaining possible issues like more accurate N3LO np data or the ambiguity in the determination of c_D and c_E.

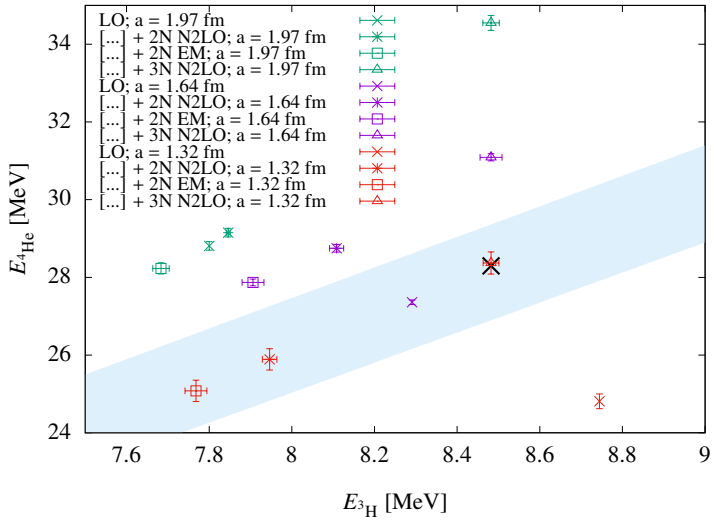

Figure 5.9: ^{3}H-^{4}He binding energy plot for various lattice spacings. The black dot is the physical point and the blue band is the Tjon band according to [72]. The ^{4}He errors include statistical and LEC errors while the ^{3}H errors only include LEC errors.

5.6 Conclusion

In this chapter we have analysed the Tjon band in the framework of NLEFT. We studied the two-, three-, and four-body sector for lattice spacings from $a = 1.97$ fm to $a = 1.32$ fm up to N2LO and including subleading two-pion-exchange contributions as well as the electromagnetic interaction and the leading 3NFs. There is a general convergence of the phase shifts in the two-body sector by including higher orders as well as shifting to smaller lattice spacings. In the three-body sector we found almost similar results at N2LO for all three-cases. The reason for this is that the three-body bound state is not sensitive to all np phase shifts in the same way, and even though the description of the phase shifts becomes better in general, some particular phase shifts do not improve leading to the general underbinding of the system. In the ^{4}He system we observed a strong overbinding of about 6 MeV due to lattice effects for the coarse lattice which becomes smaller with decreasing lattice spacings and vanishes finally. By comparing the triton and ^{4}He binding energies for each lattice spacing and each order, one can see a convergence towards the Tjon line with smaller lattice spacing after including N2LO-forces, N2LO+EM-forces and N2LO+EM+3N forces, respectively. Finally the Tjon line is hit and confirming the conjecture that light (and medium mass) nuclei can be described by 2NFs and 3NFs only. The inclusion of 3N forces gives a helium-4 binding energy prediction of $E_B = -28.37(28)(4)$ MeV which is consistent with the experimental value, $E^{\mathrm{exp}}_{^4\mathrm{He}} = -28.30$ MeV. Even though the deviation from the Tjon band vanishes for small lattice spacings, further investigation of these implicit multi-particle interactions is necessary as these small lattice spacings require very expensive computational resources due to the increased number of nodes necessary for a reasonable volume. Further improvements on the results discussed here can be obtained by improved statistics particularly for the smallest lattice spacing, by more accurate N3LO np and pp phase shifts, and also from more detailed studies of the discretization effects arising from variations of the ratio a^2/a_t that was kept fixed here. Finally, a reassessment of the determination of the 3NFs LECs c_D and c_E would be useful.

CHAPTER 6

Lattice Improvement in Lattice Effective Field Theory*

6.1 Introduction

Lattice simulations based on the framework of effective field theory (EFT) have been used in the study of nuclear forces [116, 138], nuclear structure [34, 35, 108, 129, 139, 140], as well as scattering and reactions [36, 133, 141]. It has also been applied to few-body [142, 143] and many-body [144–150] problems in ultracold atomic systems. One of the challenges common to all of these lattice calculations is the need to eliminate errors caused by the non-vanishing lattice spacing a. Lattice spacing errors or artifacts can grow in importance as the number of particles increases. This is especially true in cases where the particles form compact bound states. The problem of lattice errors in computing compact bound states has been studied in two-dimensional droplets of bosons with attractive zero range interactions [128]. In Chap. 5 lattice spacing errors were studied in light nuclei to understand deviations from a universal relation between the triton and alpha-particle binding energies called the Tjon line [24, 72].

One practical approach to reducing lattice artifacts is to introduce a continuous-space regulator that renders the particle interactions ultraviolet finite. In that case one can take the lattice spacing to zero smoothly without any need to renormalize operator coefficients, see [38] and Chap. 4. This process does not remove errors produced by the continuous-space regulator, but it has the advantage of eliminating unphysical lattice artifacts such as rotational symmetry breaking. Another approach to removing lattice artifacts is accelerating the convergence to the continuum limit by including irrelevant higher-dimensional operators into the lattice action. This general technique is called lattice improvement and was first introduced by Symanzik [3, 4]. The key idea is to write the lattice action as

$$S(a) = S_0 + f_1(a) \cdot S_1 + f_2(a) \cdot S_2 + \cdots \tag{6.1}$$

where the coefficient functions $f_i(a)$ vanish in the continuum limit $a \to \infty$ and are tuned to cancel the dependence of the lattice Green's functions on the lattice spacing, a, at momentum scales well below the lattice cutoff momentum, π/a. The coefficient functions are ordered so that $f_i(a)$ vanishes more rapidly in the limit $a \to 0$ with increasing i.

Symanzik's improvement program has been widely used in lattice quantum chromodynamics [151–154]. The improvement program has also been implemented to varying degrees in lattice effective field theory calculations. However, a systematic study of the size of lattice errors arising in systems with

* The following chapter has been prepared for publication [137].

increasing numbers of particles has not yet been performed. In this chapter we address this problem and benchmark the effectiveness of the lattice improvement program in removing lattice errors for a one-dimensional system of bosons with zero-range interactions [62]. By building the improved lattice action step by step, we show that the lattice errors go from $O(a^1)$ at leading order (LO), to $O(a^3)$ at next-to-leading order (NLO), and then to $O(a^4)$ at next-to-next-to-leading order (N2LO). Our discussion is organized as follows. In Sec. 6.2 we introduce the one-dimensional boson system in the continuum, and in Sec. 6.3 we present the lattice implementation. We show and discuss our results in Sec. 6.4 and then summarize and give an outlook for future applications in Sec. 6.5.

6.2 Bosons in one dimension

We consider a one-dimensional system of bosons with attractive zero-range interactions [62]. The Hamiltonian is given by

$$H = -\frac{1}{2m}\sum_{i=1}^{N}\frac{d^2}{dx_i^2} + C_0\sum_{i>j=1}^{N}\delta(x_i - x_j), \tag{6.2}$$

where m is the boson mass, N is the number of particles and $C_0 < 0$ is the two-boson contact interaction coefficient. From either the Bethe ansatz [155] or by direct inspection, the ground state of this Hamiltonian is a bound state with energy

$$E_B^{N\mathrm{b}} = -\frac{m}{24}C_0^2 N(N^2-1), \tag{6.3}$$

and wave function

$$\Psi_N(x_1, x_2, \ldots, x_N) = \mathcal{N}\exp\left[\frac{mC_0}{2}\left(|x_1 - x_2| + |x_1 - x_3| + \ldots\right)\right], \tag{6.4}$$

with normalization constant $\mathcal{N}$ [62]. We note that no regularization or renormalization is needed, and all quantities are finite.

Here, we consider several different bound state and scattering observables. We will consider the binding energies of the N-boson bound state for up to five bosons and the root-mean-square radii of their corresponding wave functions. The root-mean-square radii for all the particle positions will be the same due to Bose symmetry and can be calculated as

$$r_{\mathrm{rms}}^2 = \int \mathrm{d}x_1 \cdots \mathrm{d}x_N \left|x_1 - \frac{x_1 + \cdots + x_N}{N}\right|^2 \left|\Psi_N(x_1, x_2, \ldots, x_N)\right|^2. \tag{6.5}$$

For the scattering observables, we compute coefficients of the effective range expansion for the boson-boson and dimer-boson even-parity scattering phase shifts, which we denote as δ_2 and δ_3, respectively. We use the conventions

$$p\tan\delta_2 = \frac{1}{a_2} + \frac{r_2}{2}p^2 + \ldots, \tag{6.6}$$

$$p\tan\delta_3 = \frac{1}{a_3} + \frac{r_3}{2}p^2 + \ldots, \tag{6.7}$$

where a_i is the scattering length, r_i is the effective range, and p is the relative momentum. From the

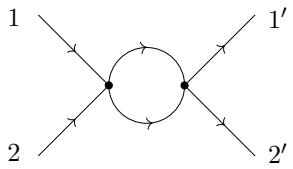

Figure 6.1: One-loop diagram $\mathcal{I}_2$ involving two bosons in the initial and the final state.

Bethe ansatz, these effective range functions are known exactly [156],

$$p \tan \delta_2 = \sqrt{-mE_B^{2b}}\,, \tag{6.8}$$

$$p \tan \delta_3 = -4\frac{a_2 p^2}{\frac{3}{2}a_2^2 p^2 - 2}\,, \tag{6.9}$$

where E_B^{2b} is the two-boson bound state energy and $a_2 = -2/(mC_0)$ is the two-boson scattering length. When implemented on a spatial lattice, this theory will be modified by the lattice momentum cutoff scale $\Lambda = \pi/a$. In order to study the size of the lattice errors, we must know the dependence of the Green's functions upon the cutoff momentum. For this analysis we use perturbation theory and determine the cutoff dependence of individual Feynman diagrams. In some cases there can be non-perturbative effects that arise from correlations that modify the ultraviolet properties of the Green's functions. However, perturbation theory is still a good starting point, and the cutoff error estimates can then be verified by numerical calculations. For our one-dimensional system of bosons, all diagrams are ultraviolet finite and so all of the cutoff effects will be of residual dependences that vanish in the continuum limit.[⋆]

The Feynman diagram with the highest degree of divergence (albeit negative) is the one-loop diagram $\mathcal{I}_2$ involving two bosons as shown in Fig. 6.1. Let the energies and momenta of the incoming particles be (E_1, p_1) and (E_2, p_2), and the energies and momenta of the outgoing particles be (E_1', p_1') and (E_2', p_2'). We write ΔI_2 for the difference between the continuum-limit amplitudes and the lattice amplitudes at lattice spacing a. We expand in powers of momenta and energies and get

$$\Delta I_2 = A_2(a) + (p_1 + p_2)^2 B_2(a) + m(E_1 + E_2)C_2(a) + O(p^4), \tag{6.10}$$

where $O(p^4)$ is shorthand for terms with more powers of momentum or energy. From dimensional analysis we find that $A_2(a) \sim O(a^1)$, while $B_2(a) \sim O(a^3)$ and $C_2(a) \sim O(a^3)$. All even expansion terms vanish in the integral calculation, and thus terms with higher powers of momentum or energy start at $O(a^5)$. The dependence on the total momentum, $p_1 + p_2$, is a result of the fact that the lattice regulator breaks Galilean invariance and so the residual amplitude ΔI_2 can depend on the frame of reference.

The diagram with the next highest degree of divergence is the one-loop diagram $\mathcal{I}_3$ involving three bosons as shown in Fig. 6.2. Let the energies and momenta of the incoming particles be (E_1, p_1), (E_2, p_2), (E_3, p_3) and the energies and momenta of the outgoing particles be (E_1', p_1'), (E_2', p_2'), (E_3', p_3'). We let ΔI_3 be the difference between the continuum-limit and lattice amplitudes. Expanding in powers of momenta and energies gives

$$\Delta I_3 = A_3(a) + O(p^2). \tag{6.11}$$

From dimensional analysis we conclude that $A_3(a) \sim O(a^3)$ and the terms with higher powers of momentum or energy start at $O(a^5)$. Our analysis thus far might give the false impression that all other

[⋆] The case of non-perturbative regularization in the two-body sector is given in App. E.

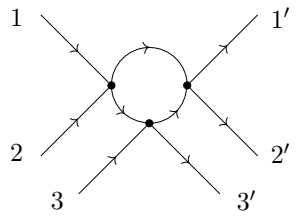

Figure 6.2: One-loop diagram $\mathcal{I}_3$ involving three bosons in the initial and the final state.

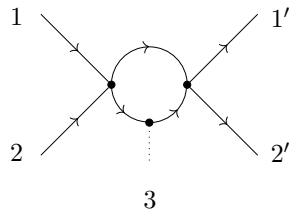

Figure 6.3: One-loop form factor diagram $\mathcal{I}_2'$ involving two bosons in the initial and the final state and one external insertion.

errors start at $O(a^5)$. However, we should note that there are two-loop diagrams involving three bosons that give a cutoff dependence that is $O(a^4)$. Furthermore, there will be $O(a^4)$ errors in the two-boson system when we iterate the improved energy-independent interactions that we use to cancel the $O(a^1)$ and $O(a^3)$ errors. We give further details for the expressions appearing in Eq. (6.10) and Eq. (6.11) in the Appendix D.

Since we are computing the root-mean-square radius, we also need to consider form factor diagrams associated with the boson density. The form factor diagram with the highest degree of divergence is the one-loop diagram $\mathcal{I}_2'$ shown in Fig. 6.3. Structurally this diagram is the same as $\mathcal{I}_3$, and so the residual amplitude will have a similar form,

$$\Delta I_2' = A_2'(a) + O(p^2). \tag{6.12}$$

From dimensional analysis $A_2'(a)$ will be $O(a^3)$. In this case, however, the momentum-independent part of the form factor just counts the number of bosons. So $A_2'(a)$ will vanish if number conservation is properly implemented on the lattice, and we assume this is the case. The root-mean-square radius is proportional to the derivative of the form factor with respect to the squared momentum transfer, and so the correction to the root-mean-square radius from this diagram will be $O(a^5)$.

6.3 Lattice implementation

We now implement our one-dimensional theory of bosons on the lattice. We use lattice units where all quantities are multiplied by powers of the lattice spacing to form dimensionless combinations. Since we are interested in methods that can be readily applied to many-body calculations, we work with energy-independent interactions only. We use an $O(a^4)$-improved free Hamiltonian lattice action,

$$H_{\text{free}} = \frac{1}{2m}\sum_n 2\omega_0 a^\dagger(n)a(n) + \frac{1}{2m}\sum_{l=1}^{3}(-1)^l\omega_l\left[a^\dagger(n+l)a(n) + a^\dagger(n)a(n+l)\right], \tag{6.13}$$

with coefficients

$$\omega_0 = \frac{49}{36}, \quad \omega_1 = \frac{3}{2}, \quad \omega_2 = \frac{3}{20}, \quad \omega_3 = \frac{1}{90}. \tag{6.14}$$

The lattice artifacts due to the free Hamiltonian start at $O(a^6)$. At LO, we have a contact interaction in the two-boson sector,

$$V_{\rm LO} = \frac{C_0}{2} \sum_n :\rho^2(n): , \tag{6.15}$$

where $\rho(n) = a^\dagger(n)a(n)$ and the :: symbols indicate normal ordering where the annihilation operators stand to the right and the creation operators stand to the left. The lattice contact interaction is tuned to the same value as the continuum-limit interaction, C_0. At NLO we have a finite renormalization of the LO interaction,

$$V_{\rm NLO} = \frac{\Delta C_0}{2} \sum_n :\rho^2(n): , \tag{6.16}$$

which is sufficient to cancel the function $A_2(a)$ in Eq. (6.10).

At N2LO, two additional operators are required in the two-boson sector. The first is proportional to the square of the transferred momentum between particles,

$$V_{{\rm N2LO},q^2} = -\frac{C_{q^2}}{2} : \sum_n \rho(n) \left[\rho(n+1) + \rho(n-1) - 2\rho(n)\right] :, \tag{6.17}$$

and it removes the residual energy dependence $C_2(a)$ in Eq. (6.10) for on-shell two-boson scattering. The second N2LO operator is a Galilean-invariance-restoring (GIR) term that is proportional to the square of the total momentum,

$$\begin{aligned} V_{\rm N2LO,GIR} = -\frac{C_{\rm GIR}}{8} \sum_n \Big[& a^\dagger(n+1)a^\dagger(n+1)a(n)a(n) + a^\dagger(n-1)a^\dagger(n-1)a(n)a(n) \\ & -2a^\dagger(n)a^\dagger(n)a(n)a(n)\Big]. \end{aligned} \tag{6.18}$$

We use this operator to correct the two-boson dispersion relation on the lattice, thereby removing the $B_2(a)$ term in Eq. (6.10). One three-boson interaction is also needed at order N2LO,

$$V_{\rm N2LO,3b} = \frac{C_{\rm 3b}}{6} \sum_n :\rho^3(n): , \tag{6.19}$$

which cancels the contribution the function $A_3(a)$ in Eq. (6.11). In all of our lattice calculations, we must also careful that finite volume errors are not being confused with lattice discretization errors. To this end, we always take the volume to be sufficiently large so that the finite volume errors are negligible.

6.4 Results

We now present lattice results at LO, NLO and N2LO and the discrepancies that remain when compared with the zero-range continuum limit. All continuum observables are calculated with $C_0 = -0.1$ and $m = 938.92$ MeV, which give binding energies roughly comparable to that of the deuteron, triton and helium-4. Of course, in the real world there is no five-body nucleonic state analogous to the five-boson bound state we consider here. Nevertheless, our analysis of residual lattice errors for this bosonic system will demonstrate the steps needed for systematic lattice improvement in nuclear lattice simulations.

row	observable	continuum result	LO	NLO	N2LO
1	E_B^{2b}	−2.347 MeV	0.974(6)	—	—
2	$r_{\rm rms}^{2b}$	1.486 fm	0.997(3)	3.05(2)	4.1(3)
3	E_B^{3b}	−9.389 MeV	0.97(2)	2.97(2)	—
4	$r_{\rm rms}^{3b}$	1.108 fm	0.97(2)	3.01(1)	4.0(3)
5	E_B^{4b}	−23.473 MeV	0.967(5)	3.05(1)	3.9(1)
6	$r_{\rm rms}^{4b}$	0.867 fm	0.97(1)	3.09(5)	4.1(2)
7	E_B^{5b}	−46.946 MeV	0.94(2)	3.21(4)	3.9(2)
8	$r_{\rm rms}^{5b}$	0.709 fm	0.86(5)	3.4(1)	4.0(2)
9	$m_{\rm eff}^{2b}$	1877.8 MeV	2.91(9)	2.96(5)	—
10	$1/a_2$	46.946 MeV	0.978(6)	2.99(6)	—
11	$1/a_3$	0 MeV	2.80(3)	2.93(6)	4.08(3)

Table 6.1: Continuum observables and lattice error exponents b_O as defined in Eq. (6.21).

We vary the lattice spacing from a maximum of $a = 1.97$ fm to values as small as computationally possible, while keeping the physical box length large enough so that finite volume effects are negligible. The determination of the lattice parameters are as follows. At LO, we consider the contact interaction with the continuum value $C_0 = -0.1$, and no fitting is needed. At NLO we fit ΔC_0 to reproduce the two-boson continuum bound-state energy E_B^{2b}. At N2LO, we fit the coefficients ΔC_0, C_{q^2}, $C_{\rm GIR}$ and C_{3b} in order to simultaneously reproduce the continuum two-boson bound-state energy E_B^{2b}, two-boson effective range r_2, two-boson effective mass $m_{\rm eff,2}$, and the three-boson bound-state energy E_B^{3b}. We determine the effective range using Eq. (6.6) and compute the elastic scattering phase shifts at finite volume using the relation [93],

$$\exp\left[2i\delta(p)\right]\exp\left(ipL\right) = 1\,. \tag{6.20}$$

Each lattice observable is fitted using the asymptotic fit function,

$$O(a) = O_c + A_O \cdot a^{b_O}, \tag{6.21}$$

where O_c is the zero-range continuum-limit value of the observable and A_O and b_O are fit parameters in the limit $a \to 0$. We show the LO bound state energies and root-mean-square radii for up to five bosons in Fig. 6.4 as well as the best fits using the asymptotic form in Eq. (6.21). The vertical lines give the upper limits of the fit range. The low-energy coupling constants are summarized in Tab. 6.2. As we see from rows one through eight of Table 6.1, the LO exponent b_O is consistent with 1. This is the same as the $O(a^1)$ estimate we derived from our perturbative analysis and the $A_2(a)$ correction in Eq. (6.10). While the lattice errors in the two-boson system are nearly linear in a over a fairly wide range, the higher powers of a become stronger as we increase the number of bosons. This goes hand-in-hand with the decreasing radius of the bound state, and is a signature that we are probing higher-momentum scales as we increase the number of particles.

The NLO and N2LO bound state energies and root-mean-square radii for up to five boson are shown in Fig. 6.5 as well as the best fits using the asymptotic form in Eq. (6.21). The crosses indicate the NLO results while the open circles are the N2LO results. The vertical lines gives the upper limits of the fit range. As shown in rows one through eight of Table 6.1, the NLO exponent b_O is about 3 while the N2LO exponent b_O is about 4. This is consistent with our $O(a^3)$ estimate of errors at NLO and $O(a^4)$ estimate of errors at N2LO. We again see that the higher powers of a become stronger as we increase the

	NLO	N2LO			
a [fm]	ΔC_0 [$\times 10^{-3}$]	ΔC_0 [$\times 10^{-3}$]	C_{3b} [$\times 10^{-3}$]	C_{q^2} [$\times 10^{-4}$]	C_{GIR} [$\times 10^{-3}$]
1.973	−8.79793	−9.09089	1.04056	7.16271	1.43521
1.715	−7.55226	−7.72824	1.11585	4.55222	1.23930
1.315	−5.67790	−5.75996	0.97610	2.41371	0.93898
0.986	−4.19286	−4.23347	0.64741	1.41280	0.69463
0.789	−3.32409	−3.34855	0.43540	0.98669	0.54967
0.659	−2.75375	−2.77014	0.30594	0.75364	0.45367
0.563	−2.35055	−2.36231	0.22429	0.60773	0.38527
0.438	−1.81824	−1.82514	0.13387	0.43622	0.29366
0.373	−1.53939	−1.54429	0.09575	0.35513	0.24475
0.303	−1.25151	−1.25473	0.06429	0.27726	0.19161
0.282	−1.16105	−1.16381	0.05604	0.25397	0.17423
0.246	−1.01441	−1.01650	0.04444	0.21731	0.14466
0.164	−0.67394	−0.67486	0.02664	0.13771	0.06049
0.098	−0.40326	−0.40360	0.02427	0.08263	0.03280

Table 6.2: Low-energy coupling constants for NLO and N2LO. All constants are in lattice units.

number of bosons, and this is likely responsible for some systematic errors in our fitted values for b_O in the five-boson system.

The lattice results for the effective two-boson mass at LO and NLO are shown Fig. 6.6 as well as the best fits using Eq. (6.21). We omit the N2LO results since they are directly fit to the continuum-limit results. As shown in row nine of Table 6.1, the values for b_O for each case is about 3. This is consistent with our perturbative analysis for the dependence on the total momentum. We found that the function $B_2(a)$ in Eq. (6.10) scales as $O(a^3)$.

In Fig. 6.7 we show the two-boson inverse scattering length $1/a_2$ at LO and NLO. The difference between the lattice scattering length at N2LO and the continuum value is so small that residual errors such as finite-volume effects get in the way of a systematic analysis of lattice spacing dependence. The dotted vertical lines give the upper limits of the fit range. As shown in row ten of Table 6.1, the values for b_O are about 1 at LO and about 3 at NLO. These are consistent with our $O(a^1)$ estimate of errors at LO and $O(a^3)$ estimate of errors at NLO. In Fig. 6.8 we show the dimer-boson inverse scattering length at LO, NLO, N2LO. The dotted vertical lines give the upper limits of the fit range. As shown in row eleven of Table 6.1, the values for b_O is about 3 at LO, 3 at NLO, and 4 at N2LO. These are consistent with our $O(a^3)$ estimate of errors at NLO and $O(a^4)$ estimate of errors at N2LO. The smaller than expected errors at LO can be understood from the fixed-point behavior of the dimer-boson inverse scattering length $1/a_3$. As can be seen in Eq. (6.9), $1/a_3$ remains zero independent of the value of $1/a_2$. As a result the $O(a^1)$ error in $1/a_3$ vanishes, and the LO errors start only at $O(a^3)$.

6.5 Summary and outlook

In this chapter we have applied the Symanzik lattice improvement program to lattice calculations of zero-range bosons in one spatial dimensions. We have considered up to five-boson bound states and computed bound-state energies, root-mean-square radii, effective masses, and inverse scattering lengths

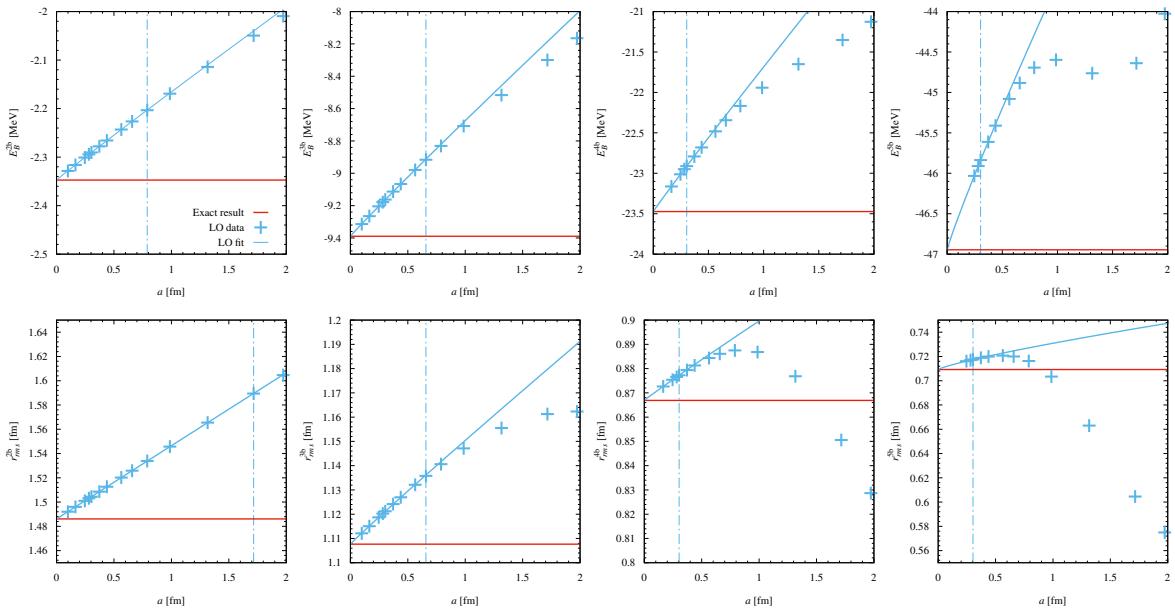

Figure 6.4: Bound-state energies and root-mean-square radius versus lattice spacing for up to five bosons at LO. The vertical lines give the upper limits of the fit range.

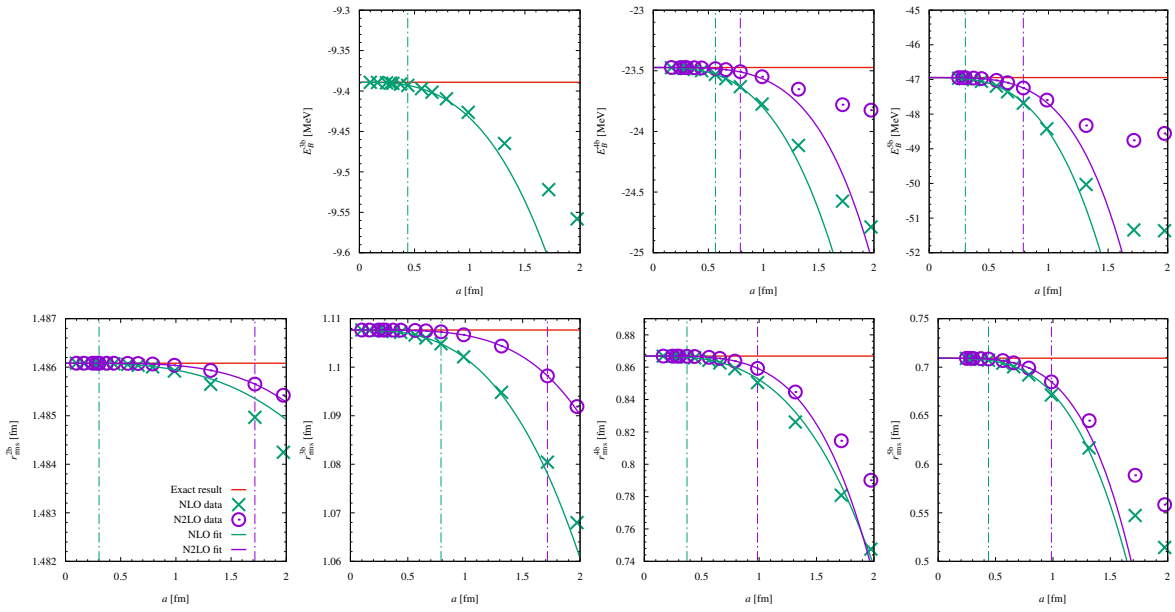

Figure 6.5: Bound-state energies and root-mean-square radius versus lattice spacing for up to five bosons at NLO and N2LO. The vertical lines give the upper limits of the fit range.

for two-boson and dimer-boson scattering. For these calculations we have constructed the lattice action at LO, NLO, and N2LO and demonstrated that the size of the lattice errors are consistent with a perturbative analysis of cutoff effects in individual Feynman diagrams. We have found that at LO the lattice errors

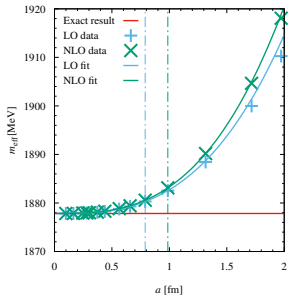

Figure 6.6: Effective mass in the two-boson sector at LO and NLO. The vertical lines gives the upper limits of the fit range.

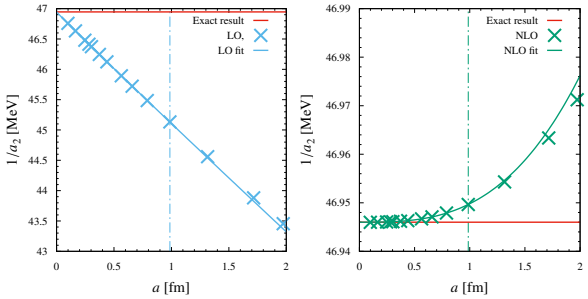

Figure 6.7: The two-boson inverse scattering length $1/a_2$ versus lattice spacing at LO and NLO. The dotted vertical lines give the upper limits of the fit range.

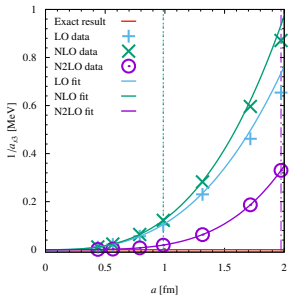

Figure 6.8: The dimer-boson inverse scattering length $1/a_3$ versus lattice spacing at LO, NLO, and N2LO. The vertical lines give the upper limits of the fit range.

are $O(a^1)$, unless suppressed due to kinematical reasons or special fixed-point behavior, as noted in a couple of examples above. Meanwhile, the errors at NLO are typically $O(a^3)$, and the errors at N2LO are $O(a^4)$. The removal of any of the terms in the improved action would result in a larger lattice error in the continuum limit.

The N2LO three-boson interaction proportional to C_{3b} is particularly interesting. We have used it to cancel lattice errors at $O(a^3)$, and it does indeed remove residual errors in the structure and binding of bound states with three or more bosons. We note that for zero-range bosons in three spatial dimensions, the three-boson interaction is required at LO to properly renormalize the theory [67, 69], see also [157].

While a four-boson contact interaction is not needed for renormalization in the three-dimensional theory [158, 159], one lesson learned from the analysis presented here is that the four-boson interaction could be useful as part of a comprehensive lattice improvement program to remove lattice errors in systems with four or more bosons.

The lattice improvement program for more complicated systems in lattice effective field theory can proceed along similar lines, but may require more effort. Some complications occur in effective field theories where non-perturbative iteration is used and singular interactions prevent the limit of infinite cutoff momentum. For example, this is the case in chiral effective field theory for nucleons (see Ref. [52] for a review). In such cases one would need to verify the convergence of improved lattice formulations over a finite range of lattice spacings with each other rather than comparing with the limit of zero lattice spacing. Similar issues strategies are used in non-relativistic QCD for heavy quarks on the lattice, where the lattice spacing should not be much smaller than the Compton wavelength of the heavy quark [160–162].

While the analysis we presented here is for a simple system of zero-range bosons in one dimension, it serves as a useful guide for increasing the accuracy of more complicated calculations in lattice effective field theory with improved lattice actions. For zero-range bosons in one dimension, we found that our estimates of the lattice errors from naive dimensional analysis of individual diagrams were accurate. However, this is directly related to the ultraviolet finiteness of our one-dimensional system. In general, we will need to regulate and renormalize divergent diagrams. And, therefore, the renormalization group will be needed to compute anomalous dimensions that modify the naive dimensional analysis.

CHAPTER 7

Conclusions and Perspectives

Some limitations and challenges of nuclear lattice effective field theory have been studied in this thesis. For a better understanding and a link to continuum nuclear effective theory, we have done a detailed investigation into the connection between lattice spacing artifacts, cutoff effects and physical observables of the effective theory for few-body systems in nuclear physics. This analysis helps to bridge the gap between the lattice community and the continuum nuclear effective theory community and as such enhances the acceptance of this rather new approach for challenging calculation in the analysis of nuclear structure on the one hand and nuclear scattering on the other hand.

After a thorough introduction into continuum and lattice nuclear effective field theory as well as scattering theory in the infinite and finite volume we had a look at the two-nucleon problem at leading order in Chap. 4. We calculated the binding energy and S wave effective range expansion parameters for different lattice spacings in the range of $a \approx 2$ fm, $\Lambda \approx 314$ MeV to $a \approx 0.5$ fm, $\Lambda \approx 1240$ MeV. The lattice volume was chosen such that the finite volume extrapolation formulas for bound states as well as effective range could be used. The latter value of $\Lambda \approx 1240$ MeV is beyond the cutoff of nuclear effective field theory and as such it is a good test for the decoupling of the lattice cutoff and the soft regulator acting over and above on all nucleon-nucleon potentials. Firstly, we did the calculation in the framework of pionless theory whereas in the second part we included pions as well. The contact interaction was smeared to increase the stability and predictability of S wave scattering properties. The one-pion exchange potential has been regularized using a position space regularization scheme to avoid unphysical effects caused by the short-range singularity of the potential. It was shown that one can successfully decouple the physical meaning of the lattice spacing by introducing a smooth cutoff in all potential terms. Hence, the physics of the two-nucleon system became independent of the lattice spacing a, or the hard cutoff Λ, respectively, and only depended on the soft regulator, which was fitted to physical properties.

The main project of this thesis was given in Chap. 5 where we did an analysis of the $2N$, $3N$ and $4N$ system to reproduce the well-known Tjon band. Therefore we put the complete next-to-next-to-leading order nuclear effective theory framework on the lattice. The parameters of the $2N$ sector were fitted to Nijmegen phase shift data for S and P waves as well as the deuteron binding energy $E_{^2\mathrm{H}} = -2.224575(9)$ MeV. The remaining $3N$ parameter was fitted to the triton binding energy $E_{^3\mathrm{H}} = -8.4820(1)$ MeV. We used exact methods in the $2N$ and $3N$ sector, albeit we had to rely on Monte Carlo methods in the $4N$ sector. We repeated the procedure for three distinct lattice spacings $a = 1.97$ fm, $a = 1.64$ fm and $a = 1.32$ fm. In the $2N$ sector, we have found a general improvement for large momenta by decreasing the lattice spacing while the physics is lattice spacing independent for low momenta. Some deterioration particularly for the ${}^1S_0$ description and the finest lattice spacing could be traced back to the

smearing parameter, which was chosen constant for all three lattice spacings. For P and D waves there was a general improvement from leading order to next-to-next-to-leading order and from coarse to the fine lattice. While the next-to-next-to-leading order descriptions stopped to give a very good description for almost half of the P and D waves at 100 MeV for $a = 1.97$ fm, almost all P and D waves are described well up to 150 MeV or even beyond for $a = 1.32$ fm. The extension to pp and nn interaction worked quite well and the ${}^1S_0$ pp description follows the same pattern as the ${}^1S_0$ np description. In the $3N$ sector, we have shown that the necessary infinite volume extrapolation due to increased lattice size was precise for the finest lattice spacing and the difference between an assumed 2+1 or 1+1+1 bound state is negligible. The main motivation for this chapter was the Tjon band, which states that ^{4}He binding energy should be automatically reproduced once the remaining $3N$ parameter is fixed by the physical ^{3}H binding energy. Without a $3N$ force, the ^{3}H-^{4}He data points should appear in an almost linear band. However, we have found a strong overbinding of ^{4}He at the standard lattice spacing of $a = 1.97$ fm. This has been observed in earlier calculations and it has been conjectured that the overbinding is caused by the coarse lattice and that it should vanish with smaller lattice spacing. After fixing the triton binding energy at its physical value, the ^{4}He binding energy prediction was -34.55(18)(3) MeV, -31.09(7)(6) MeV and -28.37(28)(3) MeV for $a = 1.97$ fm, $a = 1.64$ fm, $a = 1.32$ fm respectively. Hence, the lattice spacing of $a = 1.32$ fm is small enough to reproduce the ^{4}He binding energy of $E_{^4\mathrm{He}} = -28.30$ MeV without an additional $4N$ force.

The third part was given in Chap. 6 where we turned to some aspects of lattice field. The well-known Symanzik improvement program has been applied successfully to the few-boson system in one dimension. We calculated binding energies and radial mean square radii up to five bosons as well as scattering properties for 1+1 and 2+1 scattering processes. As these systems have an exact solution, it is possible to distinct lattice spacing errors from other error sources. Due to dimensional analysis, the lattice spacing errors scale with $O(a)$, $O(a^3)$ and $O(a^4)$ at leading order, next-to-leading order and next-to-next-to-leading order. We could reproduce the predicted scaling particularly for two- and three-bosons system as well as for next-to- and next-to-next-to-leading order. For instance, having a look at the binding energy, we see the expected overbinding for large lattice spacings, which is reduced for finer lattice spacings as well as for the inclusion of higher-order corrections. The overbinding becomes more severe, the more particles are in the system reflecting its origin in the implicit many-particle interaction.

Generally, we have successfully handled the lattice spacing effects in NLEFT for the description of few-body nuclear physics. However, there are still different possibilities to increase the predictability and efficiency of NLEFT:

- In Chap. 4 we have used a soft position-space regularization for the one-pion-exchange. It would be interesting to use such an operator for the full analysis in combination with an exact momentum space discretization. The advantages are two-fold. Firstly, the one-pion exchange does not have a singular structure in the origin anymore due to the position-space regularization and thus it improves Monte Carlo simulations. Secondly, one already has an improved description of P waves at leading order due to the exact momentum space discretization [116].

- There was already a preliminary study on the effect of the temporal discretization in relation to the spatial discretization [163]. Hence, it may be useful to vary this parameter and see, whether we could reach the Tjon band already for coarse lattices and as such reduce the effect of implicit multiparticle interaction.

- The analysis of Chap. 5 could be extended to larger nuclei like ^{8}Be, ^{12}C, ^{16}O, etc.. Once the four-body force is not necessary in the case of ^{4}He, it should not be necessary in larger nuclei as well and these binding energies should be reproduced correctly.

- For higher accuracy, it would be useful to clearly separate physical cutoff effects and lattice spacing discretization effects such that one could transfer the ideas from Chap. 6 to Chap. 5. Though this is doubtful for a full theory due to the large number of interaction terms and the general non-existence of non-perturbative solutions, it may be feasible in the case of pionless effective theory. Here, the number of terms is reduced and there exists already a lot of work on renormalization group, the dibaryon field trick for a simpler solution of the three-body problem and so on.

APPENDIX A

Special functions and algebras

A.1 Partial wave decomposition

In the following we give the definition of special functions used throughout the thesis. A basis of spherical functions is given by the spherical harmonics $Y_{l,l_z}(\phi,\theta)$, where $l = 0, 1, 2, \infty$ and $l_z = -l, -l+1, \ldots, l$. They are defined as

$$Y_{l,l_z}(\phi,\theta) = (-1)^{l_z}\left[\frac{2l+1}{4\pi}\frac{(l-l_z)!}{(l+l_z)!}\right]^{\frac{1}{2}} P_{l,l_z}(\cos\theta)\exp\left(il_z\phi\right), \tag{A.1}$$

with the Laguerre polynomials,

$$P_{l,l_z}(x) = (1-x^2)^{\frac{l_z}{2}}\frac{\mathrm{d}^{l_z}}{\mathrm{d}x^{l_z}}P_l(x). \tag{A.2}$$

$P_l(x)$ are the Legendre polynomials

$$P_l(x) = \frac{1}{2^l l!}\frac{\mathrm{d}^l}{\mathrm{d}x^l}\left(x^2-1\right)^l. \tag{A.3}$$

The spherical harmonics have the following properties,

$$Y_{l,l_z}(\theta,\phi) = (-1)^{l_z}\left[Y_{l,l_z}(\theta,\phi)\right]^*, \tag{A.4}$$

$$\left\langle Y_{l,l_z}(\phi,\theta)\,\middle|\, Y_{l',l'_z}(\phi,\theta)\right\rangle = \delta_{l,l'}\delta_{l_z,l'_z} \tag{A.5}$$

$$\sum_{l=0}^{\infty}\sum_{l_z=-l}^{l}\left|Y_{l,l_z}(\phi,\theta)\right\rangle\left\langle Y_{l,l_z}(\phi',\theta')\right| = \delta_{\phi,\phi'}\delta_{\theta,\theta'}. \tag{A.6}$$

The Riccati-Bessel functions are defined recursively by

$$y_{l+1}(z) = -y'_l(z) + (l+1)z^{-1}y(z), \tag{A.7}$$

where $y_l(z)$ is the regular [irregular] solution $u_l(z)$ [$n_l(z)$]. The first solutions have the form

$$u_0(z) = \sin(z), \tag{A.8}$$

$$n_0(z) = \cos(z). \tag{A.9}$$

As the Riccati-Bessel functions do not represent in- and outgoing wave functions, we have to use the Hankel functions, which are a linear combination of the former ones defined as

$$h_l^{\pm}(z) = u_l(z) \pm i n_l(z)\,. \tag{A.10}$$

Then $h_l^{\pm}(z)$ represents an outgoing and incoming partial wave, respectively.

The confluent hypergeometric function which is necessary for the Coulomb wave functions reads

$$F(a,b;z) = \sum_{n=0}^{\infty} \frac{\Gamma(a+n)}{\Gamma(a)} \frac{\Gamma(b)}{\Gamma(b+n)} \frac{z^n}{n!}. \tag{A.11}$$

Similar to the regular and irregular Bessel functions, there exists a second confluent hypergeometric function U which is defined as

$$U(a,b;z) = \frac{\Gamma(1-b)}{\Gamma(a-b+1)} F(a,b;z) + \frac{\Gamma(b-1)}{\Gamma(a)} z^{1-b} F(a-b+1, 2-b; z). \tag{A.12}$$

Depending on the evaluation procedure, it may be useful to replace the functions F and U by the corresponding Whittaker functions,

$$M_{k,m}(z) = \exp\left(\frac{-z}{2}\right) z^{m+\frac{1}{2}} F\left(m-k+\frac{1}{2}; 1+2m; z\right), \tag{A.13}$$

$$W_{k,m}(z) = \exp\left(\frac{-z}{2}\right) z^{m+\frac{1}{2}} U\left(m-k+\frac{1}{2}; 1+2m; z\right). \tag{A.14}$$

The aforementioned Γ function is defined by

$$\Gamma(z+1) = \int_0^{\infty} \mathrm{d}t\, t^z \exp(-t), \tag{A.15}$$

and fulfills the recursive equation

$$\Gamma(z+1) = z\Gamma(z). \tag{A.16}$$

A.2 Pauli matrices and spin algebra

The Pauli matrices are the generators of the SU(2) algebra. They are defined as

$$\sigma_1 = \begin{pmatrix} 0 & 1 \\ 1 & 0 \end{pmatrix}, \qquad \sigma_2 = \begin{pmatrix} 0 & -i \\ i & 0 \end{pmatrix}, \qquad \sigma_3 = \begin{pmatrix} 1 & 0 \\ 0 & -1 \end{pmatrix}, \tag{A.17}$$

and fulfill the following angular momentum algebra,

$$\left[\sigma_i, \sigma_j\right] = 2i\epsilon_{ijk}\sigma_k, \tag{A.18}$$

with ϵ_{ijk} the totally antisymmetric Levi-Civita tensor. The respective spin matrix is defined as

$$\vec{S} = \frac{1}{2}\vec{\sigma}, \tag{A.19}$$

whose eigenvalues are

$$S^2 \left|S, S_z\right\rangle = S(S+1) \left|S, S_z\right\rangle, \tag{A.20}$$

$$S_z \left|S, S_z\right\rangle = S_z \left|S, S_z\right\rangle. \tag{A.21}$$

It can be used to evaluate the appearing operators $\sigma_1 \cdot \sigma_2$ in the respective triplet and singlet channel,

$$\vec{\sigma}_1 \cdot \vec{\sigma}_2 \left|S = 1\right\rangle = 1 \left|S = 1\right\rangle, \tag{A.22}$$

$$\vec{\sigma}_1 \cdot \vec{\sigma}_2 \left|S = 0\right\rangle = -3 \left|S = 0\right\rangle. \tag{A.23}$$

The isospin case for $\vec{\tau}_1 \cdot \vec{\tau}_2$ is analogous.

A.3 Anticommutator and Grassmann algebra

As nucleons are fermions, their respective creation and annihilation operators fulfill the following anticommutating relations,

$$\left\{a_i\left(\vec{n}\right), a_j\left(\vec{n}'\right)\right\} = 0, \tag{A.24}$$

$$\left\{a_i^\dagger\left(\vec{n}\right), a_j^\dagger\left(\vec{n}'\right)\right\} = 0, \tag{A.25}$$

$$\left\{a_i\left(\vec{n}\right), a_j^\dagger\left(\vec{n}'\right)\right\} = \delta_{i,j}\delta\left(\vec{n} - \vec{n}'\right). \tag{A.26}$$

Here, i represents any internal quantum number of the creation and annihilation operator, which acts on the spatial point $\vec{n}^{(\prime)}$.

The Grassmann variables are a special kind of numbers, which are defined by the following properties,

$$\int \mathrm{d}c_i\left(\vec{n}, n_t\right) = \int \mathrm{d}c_i^*\left(\vec{n}, n_t\right) = 0, \tag{A.27}$$

$$\int \mathrm{d}c_i\left(\vec{n}, n_t\right)\, c_i\left(\vec{n}, n_t\right) = 1, \tag{A.28}$$

$$\int \mathrm{d}c_i^*\left(\vec{n}, n_t\right)\, c_i^*\left(\vec{n}, n_t\right) = 1. \tag{A.29}$$

Using the abovementioned properties, one can show explicitly that

$$\mathrm{Tr}\left[:\, f\left(a^\dagger, a\right) :\right] = \int \mathrm{d}c\mathrm{d}c^*\, \exp\left(2c^\dagger c\right) f\left(c^*, c\right), \tag{A.30}$$

where the argument of a, c are suppressed for better readability.

APPENDIX B

Density and current operators

Here, we define the various nucleon density, current and derivative operators that we are using. Following Refs. [32, 116, 164], we define the local density operators. The LO and NLO density operators include contact, contact isospin, contact spin as well as contact spin-isopsin operators given by

$$\rho(\vec{n}) = \sum_{i,j=0,1} a^{\dagger}_{i,j}(\vec{n}) a_{i,j}(\vec{n}), \tag{B.1}$$

$$\rho_I(\vec{n}) = \sum_{i,j,j'=0,1} a^{\dagger}_{i,j}(\vec{n}) (\tau_I)_{j,j'} a_{i,j'}(\vec{n}), \tag{B.2}$$

$$\rho_S(\vec{n}) = \sum_{i,i',j=0,1} a^{\dagger}_{i,j'}(\vec{n}) (\sigma_S)_{i,i'} a_{i',j}(\vec{n}), \tag{B.3}$$

$$\rho_{S,I}(\vec{n}) = \sum_{i,i',j,j'=0,1} a^{\dagger}_{i,j}(\vec{n}) (\sigma_S)_{i,i'} (\tau_I)_{j,j'} a_{i',j'}(\vec{n}), \tag{B.4}$$

while the current, isospin, spin and spin-isospin current density operator are given by

$$\Pi_l(\vec{n}) = \sum_{i,j=0,1} a^{\dagger}_{i,j}(\vec{n}) \nabla_l a_{i,j}(\vec{n}) - \sum_{i,j=0,1} \nabla_l a^{\dagger}_{i,j}(\vec{n}) a_{i,j}(\vec{n}),$$

$$\Pi_{l,I}(\vec{n}) = \sum_{i,j,j'=0,1} a^{\dagger}_{i,j}(\vec{n}) (\tau_I)_{j,j'} \nabla_l a_{i,j'}(\vec{n}) - \sum_{i,j,j'=0,1} \nabla_l a^{\dagger}_{i,j}(\vec{n}) (\tau_I)_{j,j'} a_{i,j'}(\vec{n}),$$

$$\Pi_{l,S}(\vec{n}) = \sum_{i,i',j=0,1} a^{\dagger}_{i,j}(\vec{n}) (\sigma_S)_{i,i'} \nabla_l a_{i',j}(\vec{n}) - \sum_{i,i',j=0,1} \nabla_l a^{\dagger}_{i,j}(\vec{n}) (\sigma_S)_{i,i'} a_{i',j}(\vec{n}),$$

$$\Pi_{l,S,I}(\vec{n}) = \sum_{i,i',j,j'=0,1} a^{\dagger}_{i,j}(\vec{n}) (\sigma_S)_{i,i'} (\tau_I)_{j,j'} \nabla_l a_{i',j'}(\vec{n}) - \sum_{i,i',j,j'=0,1} \nabla_l a^{\dagger}_{i,j}(\vec{n}) (\sigma_S)_{i,i'} (\tau_I)_{j,j'} a_{i',j'}(\vec{n}),$$

where the derivative operator reads $\nabla_l f(\vec{n}) = (1/2)[f(\vec{n} + \hat{e}_l) - f(\vec{n} - \hat{e}_l]$. Due to the inclusion of electromagnetic corrections, we include isospin-up and -down operators

$$\rho_p(\vec{n}) = a^{\dagger}(\vec{n})(\mathbb{1} + \tau_3) a(\vec{n}), \tag{B.5}$$

$$\rho_n(\vec{n}) = a^{\dagger}(\vec{n})(\mathbb{1} - \tau_3) a(\vec{n}), \tag{B.6}$$

as well.

APPENDIX C

Uncertainty analysis

From the definition of χ^2 given in Eq. (5.46), we note that χ^2 is a function of the LO and NLO coupling constants

$$\chi^2_{\mathrm{LO}} = \chi^2\left(C_{^1S_0}, C_{^3S_1}, \right), \tag{C.1}$$

$$\chi^2_{\mathrm{N2LO}} = \chi^2\left(C_1, \ldots, C_{10}\right), \tag{C.2}$$

$$\ldots.$$

χ^2 can be expanded around its minimum, giving

$$\chi^2 = \chi^2_{\mathrm{min}} + \frac{1}{2}\sum_{i,j} h_{ij}(C_i - C_i^{\mathrm{min}})(C_j - C_j^{\mathrm{min}}) + \ldots, \tag{C.3}$$

where the Hessian matrix is denoted by

$$h_{ij} \equiv \frac{\partial^2 \chi^2}{\partial C_i \partial C_j}, \tag{C.4}$$

and C_i^{min} denotes the result of the χ^2 fit. Then the error (or variance-covariance) matrix is defined as

$$\mathcal{E}_{ij} \equiv \frac{1}{2}[h^{-1}]_{ij}, \tag{C.5}$$

while the error of any fit parameter is given by its standard deviation,

$$\sigma_i = \sqrt{\mathcal{E}_{ii}}. \tag{C.6}$$

Following Ref. [116] we again find a very large χ due to the underestimation of the PWA errors. Hence we have to rescale χ^2 in the case of the phase shift calculation to get reasonable error estimates. In this case, we rescale χ^2 by

$$\chi^2 \to N_{\mathrm{dof}} \frac{\chi^2}{\chi^2_{\mathrm{min}}}, \tag{C.7}$$

such that $\chi^2/N_{\mathrm{dof}} \approx 1$ in the minimum [165, 166].
In the analysis, we also have to propagate the errors of the LECs to physical observables like phase shifts

or binding energies. For a given observable O, we assign an uncertainty according to

$$\Delta O \equiv \sqrt{(J_O^T)_i \mathcal{E}_{ij} (J_O)_j}, \tag{C.8}$$

where

$$(J_O)_i \equiv \frac{\partial O}{\partial C_i}, \tag{C.9}$$

is the Jacobian vector of O with respect to the C_i.

APPENDIX D

Loop integrals

In the following we give more details about the terms appearing in Eq. (6.10) and Eq. (6.11). In our notation, (E_i, p_i) are the incoming energies/ momenta and (E_i', p_i') are the outgoing energies/ momenta. The non-relativistic propagator for a single boson is defined as

$$S(E,p) = \frac{1}{E - \frac{p^2}{2m} + i\epsilon}, \tag{D.1}$$

and the one-loop integral for the two-boson diagram in Fig. 6.1 reads

$$\begin{aligned} \mathcal{I}_2\left(E_1,p_1,E_2,p_2;E_1',p_1',E_2',p_2'\right) &\sim \int_{\pi/a}^{\pi/a}\frac{\mathrm{d}p}{2\pi}\int\frac{\mathrm{d}p_0}{2\pi}S\left(E_{12}-p_0,p+p_{12}\right)S\left(p_0,p\right) \\ &\sim \frac{im}{2}\sqrt{\frac{1}{-mE_{12}}} - \frac{1}{16\sqrt{m}}\left(\frac{1}{E_{12}}\right)^{\frac{3}{2}}p_{12}^2 - \frac{ima}{\pi^2} - \frac{iE_{12}m^2}{3\pi^4}a^3 + \frac{mp_{12}^2}{6\pi^4}a^3 + O(a^5,p^4), \end{aligned} \tag{D.2}$$

where we use energy and momentum conservation, $E_{12} = E_1 + E_2 = E_1' + E_2'$ and $p_{12} = p_1 + p_2 = p_1' + p_2'$, respectively. The $A_2(a)$, $B_2(a)$ and $C_2(a)$ can be read off immediately from Eq. (D.2).

The one-loop integral for the three-boson diagram in Fig. 6.2 is given by

$$\begin{aligned} &\mathcal{I}_3\left(E_1,p_1,E_2,p_2,E_3,p_3;E_1',p_1',E_2',p_2',E_3',p_3'\right) \\ &\quad\sim \int_{\pi/a}^{\pi/a}\frac{\mathrm{d}p}{2\pi}\int\frac{\mathrm{d}p_0}{2\pi}S\left(E_{12}-p_0,p+p_{12}\right)S\left(p_0,p\right)S\left(p_0,p\right) \\ &\quad\sim \frac{-1}{4}\frac{\sqrt{m}}{E_{12}^{\frac{3}{2}}} - \frac{3}{32}p_{12}^2\frac{\sqrt{m}}{E_{12}^{\frac{5}{2}}} + \frac{im^2}{3\pi^4}a^3 + O(a^5,p^4), \end{aligned} \tag{D.3}$$

where we choose for simplicity that $E_3 = E_3' = 0$, $p_3 = p_3' = 0$ and set $E_{12} = E_1 + E_2 = E_1' + E_2'$ and $p_{12} = p_1 + p_2 = p_1' + p_2'$. Then $A_3(a)$ is given by Eq. (D.3) for this choice of momenta and energies.

APPENDIX E

Non-perturbative calculation of lattice artifacts in the two-boson sector

In Chap. 6 we argued that a non-perturbative treatment of cutoff/ lattice spacing effects in an effective framework is preferable but not practical. However, in the two-body sector with only contact interaction it is possible. In the following we give explicit expressions for the coupling constants ΔC_0 and C_{q^2} which cancel the cutoff artifacts at $O(a)$ and $O(a^3)$ in the T-matrix of the two-body sector. In general, we follow the arguments of [112, 167]. The potential is written as

$$V\left(p, p'\right) = C + C_2\left(p^2 + p'^2\right), \tag{E.1}$$

where p, p' are the momenta of incoming and outgoing state. For simplicity, C consists of its LO and NLO term, $C = C_0 + \Delta C$. Then Eq. (E.1) can be reexpressed as

$$V\left(p, p'\right) = \sum_{i,j=0}^{1} p'^{2i} \lambda_{ij} p^{2j}, \tag{E.2}$$

with

$$\lambda = \begin{pmatrix} C & C_2 \\ C_2 & 0 \end{pmatrix}. \tag{E.3}$$

Now the Lippmann-Schwinger equation has the form

$$T\left(p', p; E\right) = \sum_{i,j=0}^{1} p'^{2i} \tau_{ij}(E) p^{2j}, \tag{E.4}$$

where τ must fulfill the following equation

$$\tau(E) = \lambda + \lambda \mathcal{I}(E) \tau(E), \tag{E.5}$$

with

$$\mathcal{I}(E) = \begin{pmatrix} I_0(E) & I_2(E) \\ I_2(E) & I_4(E) \end{pmatrix}. \tag{E.6}$$

The full expressions for the integrals $I_n(E)$ read

$$I_n(E) = \int_{-\frac{\pi}{a}}^{\frac{\pi}{a}} \frac{\mathrm{d}k}{2\pi} \frac{k^n}{E - \frac{k^2}{2\mu} + i\epsilon}, \tag{E.7}$$

$$I_0(E) = \frac{\sqrt{2}\mu \tanh^{-1}\left(\frac{\pi}{\sqrt{2}a\sqrt{E\mu}}\right)}{\pi\sqrt{E\mu}}, \tag{E.8}$$

$$I_2(E) = \frac{2\sqrt{2}\mu\sqrt{E\mu}\tanh^{-1}\left(\frac{\pi}{\sqrt{2}a\sqrt{E\mu}}\right)}{\pi} - \frac{2\mu}{a}, \tag{E.9}$$

$$I_4(E) = -\frac{2\pi^2\mu}{3a^3} - \frac{4\sqrt{2}E^2\mu^3\sqrt{-\frac{1}{E\mu}}\tan^{-1}\left(\frac{\pi\sqrt{-\frac{1}{E\mu}}}{\sqrt{2}a}\right)}{\pi} - \frac{4E\mu^2}{a}. \tag{E.10}$$

Remember that the integral momentum cutoff Λ is given by $\Lambda = \pi/a$. The reduced mass of the system reads μ. We can solve the integral equation in Eq. (E.5) and get an explicit solution for the T-matrix,

$$\frac{1}{T^{\mathrm{on}}(E)} = \frac{\left[C_2 I_2(E) - 1\right]^2 - I_0(E)\left[C + C_2^2 I_4(E)\right]}{C + C_2\left\{C_2\left[I_4(E) - 4EI_2(E)\mu(E\mu+1)\right]\right\} + 4E\mu(E\mu+1)}. \tag{E.11}$$

Note that the integrals $I_2(E)$ and $I_4(E)$ are UV divergent for $a \to 0$. Therefore we regularize the expressions such that the divergent parts are absorbed by the bare coupling constants. In the following we use the regularized expressions, but we do not change the notation for better readability. Then the inverse T-matrix reads

$$\frac{1}{T^{\mathrm{on}}(E)} = \frac{\sqrt{2}\sqrt{\mu}\tanh^{-1}\left(\frac{\pi}{\sqrt{2}a\sqrt{E}\sqrt{\mu}}\right)(C + 4C_2E\mu) - \pi\sqrt{E}}{\sqrt{E}\left\{4\sqrt{2}C_2^2E^{3/2}\mu^{5/2}(2E\mu+1)\tanh^{-1}\left(\frac{\pi}{\sqrt{2}a\sqrt{E}\sqrt{\mu}}\right) - \pi\left[C + 4C_2E\mu(E\mu+1)\right]\right\}}. \tag{E.12}$$

As we want to do an effective range expansion, we rewrite the previous equation in terms of p^2 using the dispersion relation $E = p^2/(2\mu)$,

$$\frac{1}{T^{\mathrm{on}}(p)} = \frac{\sqrt{2}\left(\sqrt{2}\sqrt{\mu}\left(C + 2C_2p^2\right)\tanh^{-1}\left(\frac{\pi}{a\sqrt{\mu}\sqrt{\frac{p^2}{\mu}}}\right) - \frac{\pi\sqrt{\frac{p^2}{\mu}}}{\sqrt{2}}\right)}{\sqrt{\frac{p^2}{\mu}}\left\{2C_2^2\left(p^2+1\right)\mu^{5/2}\left(\frac{p^2}{\mu}\right)^{3/2}\tanh^{-1}\left(\frac{\pi}{a\sqrt{\mu}\sqrt{\frac{p^2}{\mu}}}\right) - \pi\left[C + 2C_2\left(\frac{p^2}{2}+1\right)p^2\right]\right\}}. \tag{E.13}$$

First of all, we set $a = 0$ and $C_2 = 0$. Then the inverse scattering amplitude reads

$$\frac{1}{T^{\mathrm{on}}(p)} = \frac{1}{C} + i\frac{\mu}{p}, \tag{E.14}$$

which is the well-known solution in the case of momentum-independent zero-range interaction and which gives a binding energy of $E_B = -C^2m/4$, the exact result already given by [62]. We expand the general

equation up to $O(a^3)$ and $O(p^2)$,

$$\frac{1}{T^{\text{on}}(p)} = -\frac{2a^3p^2\mu}{3\pi^4} - \frac{2a\mu}{\pi^2} + p^2\left(\frac{C_2^2\mu^2}{C} - \frac{2C_2}{C^2}\right) + \frac{1}{C} + \frac{i\mu}{p} + O\left(a^4, p^4\right), \tag{E.15}$$

where the lattice artifacts can be removed by redefining the coupling constants depending on the lattice spacing,

$$C(a) = C_0 - \frac{2aC_0^2\mu}{2aC_0\mu + \pi^2}, \tag{E.16}$$

$$C_2(a) = \frac{C(a)\left[\frac{2}{C(a)^2} - \sqrt{\frac{8a^3\mu^3}{3\pi^4C(a)} + \frac{4}{C(a)^4}}\right]}{2\mu^2}. \tag{E.17}$$

Then the corrections start at least at $O(a^4)$ or in higher orders of the effective range expansion, e.g. $O(p^4)$. This means that we have successfully removed the lattice artifacts up to and including $O(a^3)$ in the two-body sector.

Bibliography

[1] A. Deur, S. J. Brodsky, and G. F. de Téramond, Prog. Part. Nucl. Phys. **90** (2016) 1, arXiv: 1604.08082 [hep-ph] (cit. on p. 2).

[2] C. Gattringer and C. B. Lang, Lect. Notes Phys. **788** (2010) 1 (cit. on pp. 3, 22).

[3] K. Symanzik, Nucl. Phys. **B226** (1983) 187 (cit. on pp. 3, 7, 69).

[4] K. Symanzik, Nucl. Phys. **B226** (1983) 205 (cit. on pp. 3, 7, 69).

[5] S. Aoki et al., Eur. Phys. J. **C77** (2017) 112, arXiv: 1607.00299 [hep-lat] (cit. on p. 3).

[6] S. R. Beane et al., Phys. Rev. Lett. **97** (2006) 012001, arXiv: hep-lat/0602010 [hep-lat] (cit. on p. 3).

[7] S. R. Beane et al., Prog. Part. Nucl. Phys. **66** (2011) 1, arXiv: 1004.2935 [hep-lat] (cit. on p. 3).

[8] K. Orginos et al., Phys. Rev. **D92** (2015) 114512, arXiv: 1508.07583 [hep-lat] (cit. on p. 3).

[9] E. Fermi, Z. Phys. **88** (1934) 161 (cit. on p. 3).

[10] S. Weinberg, Physica **A96** (1979) 327 (cit. on p. 4).

[11] J. Gasser and H. Leutwyler, Annals Phys. **158** (1984) 142 (cit. on p. 4).

[12] J. Gasser and H. Leutwyler, Nucl. Phys. **B250** (1985) 465 (cit. on p. 4).

[13] S. Weinberg, Phys. Lett. **B251** (1990) 288 (cit. on p. 4).

[14] S. Weinberg, Nucl. Phys. **B363** (1991) 3 (cit. on pp. 4, 11, 50).

[15] V. Bernard et al., Nucl. Phys. **B388** (1992) 315 (cit. on pp. 4, 10).

[16] E. E. Jenkins and A. V. Manohar, Phys. Lett. **B255** (1991) 558 (cit. on p. 4).

[17] T. Fuchs et al., Phys. Lett. **B575** (2003) 11, arXiv: hep-ph/0308006 [hep-ph] (cit. on p. 4).

[18] T. Fuchs et al., Phys. Rev. **D68** (2003) 056005, arXiv: hep-ph/0302117 [hep-ph] (cit. on p. 4).

[19] V. Bernard, Prog. Part. Nucl. Phys. **60** (2008) 82, arXiv: 0706.0312 [hep-ph] (cit. on p. 4).

[20] S. Scherer and M. R. Schindler, Lect. Notes Phys. **830** (2012) pp.1 (cit. on p. 4).

[21] G. P. Lepage, "How to renormalize the Schrödinger equation," *Nuclear physics. Proceedings, 8th Jorge Andre Swieca Summer School, Campos do Jordao*, 1997 135, arXiv: nucl-th/9706029 [nucl-th] (cit. on p. 5).

[22] E. Epelbaum, H. Krebs, and U.-G. Meißner, Eur. Phys. J. **A51** (2015) 53, arXiv: 1412.0142 [nucl-th] (cit. on pp. 5, 13, 22, 39, 42, 46, 48, 50, 52, 56).

[23] E. Braaten and H.-W. Hammer, Phys. Rept. **428** (2006) 259, arXiv: cond-mat/0410417 [cond-mat] (cit. on pp. 5, 19, 45).

[24] J. A. Tjon, Phys. Lett. **56B** (1975) 217 (cit. on pp. 5, 19, 20, 49, 65, 69).

[25] F. Hoyle, Astrophys. J. Suppl. **1** (1954) 121 (cit. on p. 5).

[26] M. Freer and H. O. U. Fynbo, Prog. Part. Nucl. Phys. **78** (2014) 1 (cit. on p. 5).

[27] C. W. Cook et al., Phys. Rev. **107** (1957) 508 (cit. on p. 5).

[28] M. Freer et al., Rev. Mod. Phys. **90** (2018) 035004, arXiv: 1705.06192 [nucl-th] (cit. on p. 5).

[29] D. Lonardoni et al., Phys. Rev. **C97** (2018) 044318, arXiv: 1802.08932 [nucl-th] (cit. on p. 6).

[30] D. Lonardoni et al., Phys. Rev. Lett. **120** (2018) 122502, arXiv: 1709.09143 [nucl-th] (cit. on p. 6).

[31] J. Carlson et al., Rev. Mod. Phys. **87** (2015) 1067, arXiv: 1412.3081 [nucl-th] (cit. on p. 6).

[32] B. Borasoy et al., Eur. Phys. J. **A31** (2007) 105, arXiv: nucl-th/0611087 [nucl-th] (cit. on pp. 7, 21, 26, 39, 41, 42, 46, 50, 52, 87).

[33] D. Lee, Prog. Part. Nucl. Phys. **63** (2009) 117, arXiv: 0804.3501 [nucl-th] (cit. on pp. 7, 33, 35, 39, 53, 55, 63).

[34] E. Epelbaum et al., Phys. Rev. Lett. **106** (2011) 192501, arXiv: 1101.2547 [nucl-th] (cit. on pp. 7, 49, 69).

[35] E. Epelbaum et al., Phys. Rev. Lett. **109** (2012) 252501, arXiv: 1208.1328 [nucl-th] (cit. on pp. 7, 49, 69).

[36] S. Elhatisari et al., Nature **528** (2015) 111, arXiv: 1506.03513 [nucl-th] (cit. on pp. 7, 49, 69).

[37] C. Patrignani et al., Chin. Phys. **C40** (2016) 100001 (cit. on p. 7).

[38] I. Montvay and C. Urbach, Eur. Phys. J. **A48** (2012) 38, arXiv: 1105.5009 [nucl-th] (cit. on pp. 7, 39, 69).

[39] E. Epelbaum, Prog. Part. Nucl. Phys. **57** (2006) 654, arXiv: nucl-th/0509032 [nucl-th] (cit. on pp. 9, 49).

[40] S. L. Adler and W. A. Bardeen, Phys. Rev. **182** (1969) 1517, [,268(1969)] (cit. on p. 9).

[41] S. L. Adler, Phys. Rev. **177** (1969) 2426, [,241(1969)] (cit. on p. 9).

[42] J. S. Bell and R. Jackiw, Nuovo Cim. **A60** (1969) 47 (cit. on p. 9).

[43] J. Gasser, M. E. Sainio, and A. Švarc, Nucl. Phys. **B307** (1988) 779 (cit. on p. 10).

[44] N. Fettes and U.-G. Meißner, Nucl. Phys. **A676** (2000) 311, arXiv: hep-ph/0002162 [hep-ph] (cit. on p. 10).

[45] H. Krebs, A. Gasparyan, and E. Epelbaum, Phys. Rev. **C85** (2012) 054006, arXiv: 1203.0067 [nucl-th] (cit. on pp. 10, 13).

[46] M. Hoferichter et al., Phys. Rev. Lett. **115** (2015) 192301, arXiv: 1507.07552 [nucl-th] (cit. on pp. 10, 54).

[47] V. Bernard, N. Kaiser, and U.-G. Meißner, Int. J. Mod. Phys. **E4** (1995) 193, arXiv: hep-ph/9501384 [hep-ph] (cit. on p. 10).

[48] C. Ordóñez, L. Ray, and U. van Kolck, Phys. Rev. **C53** (1996) 2086, arXiv: hep-ph/9511380 [hep-ph] (cit. on p. 11).

[49] J. L. Friar and S. A. Coon, Phys. Rev. **C49** (1994) 1272 (cit. on p. 11).

[50] N. Kaiser, R. Brockmann, and W. Weise, Nucl. Phys. **A625** (1997) 758, arXiv: nucl-th/9706045 [nucl-th] (cit. on p. 11).

[51] E. Epelbaum, W. Glöckle, and U.-G. Meißner, Nucl. Phys. **A637** (1998) 107, arXiv: nucl-th/9801064 [nucl-th] (cit. on p. 11).

[52] E. Epelbaum, H.-W. Hammer, and U.-G. Meißner, Rev. Mod. Phys. **81** (2009) 1773, arXiv: 0811.1338 [nucl-th] (cit. on pp. 11, 12, 39, 49, 78).

[53] E. Epelbaum, W. Glöckle, and U.-G. Meißner, Nucl. Phys. **A747** (2005) 362, arXiv: nucl-th/0405048 [nucl-th] (cit. on pp. 13, 22).

[54] H. Krebs, A. Gasparyan, and E. Epelbaum, Phys. Rev. **C87** (2013) 054007, arXiv: 1302.2872 [nucl-th] (cit. on p. 13).

[55] R. G. Newton, *Scattering Theory of Waves and Particles*, Texts and monographs in physics, Springer, 1982 (cit. on p. 13).

[56] H. Friedrich, Lect. Notes Phys. **872** (2013) 1 (cit. on p. 13).

[57] H.-W. Hammer and D. Lee, Phys. Lett. **B681** (2009) 500, arXiv: 0907.1763 [nucl-th] (cit. on p. 17).

[58] J. M. Blatt and L. C. Biedenharn, Rev. Mod. Phys. **24** (1952) 258 (cit. on p. 17).

[59] J. M. Blatt and L. C. Biedenharn, Phys. Rev. **86** (1952) 399 (cit. on p. 17).

[60] H. P. Stapp, T. J. Ypsilantis, and N. Metropolis, Phys. Rev. **105** (1957) 302 (cit. on p. 18).

[61] B. Borasoy et al., Eur. Phys. J. **A34** (2007) 185, arXiv: 0708.1780 [nucl-th] (cit. on pp. 18, 27, 39, 49, 55, 56).

[62] J. B. McGuire, J. Math. Phys. **5** (1964) 622 (cit. on pp. 19, 70, 94).

[63] L. D. Faddeev, Sov. Phys. JETP **12** (1961) 1014, [Zh. Eksp. Teor. Fiz.39,1459(1960)] (cit. on p. 19).

[64] O. A. Yakubovsky, Sov. J. Nucl. Phys. **5** (1967) 937, [Yad. Fiz.5,1312(1967)] (cit. on p. 19).

[65] W. Glöckle, *The quantum mechanical few-body problem*, Texts and monographs in physics, Springer, 1983 (cit. on p. 19).

[66] G. Skorniakov and K. Ter-Martirosian, Sov. Phys. JETP **4** (1957) 648 (cit. on p. 19).

[67] P. F. Bedaque, H.-W. Hammer, and U. van Kolck, Nucl. Phys. **A646** (1999) 444, arXiv: nucl-th/9811046 [nucl-th] (cit. on pp. 19, 77).

[68] A. C. Phillips, Nucl. Phys. **A107** (1968) 209 (cit. on p. 19).

[69] V. Efimov, Phys. Lett. **33B** (1970) 563 (cit. on pp. 19, 77).

[70] A. Nogga, H. Kamada, and W. Glöckle, Phys. Rev. Lett. **85** (2000) 944, arXiv: nucl-th/0004023 [nucl-th] (cit. on pp. 19, 65).

[71] E. Epelbaum et al., Phys. Rev. **C66** (2002) 064001, arXiv: nucl-th/0208023 [nucl-th] (cit. on pp. 19, 20, 65).

[72] L. Platter, H.-W. Hammer, and U.-G. Meißner, Phys. Lett. **B607** (2005) 254, arXiv: nucl-th/0409040 [nucl-th] (cit. on pp. 20, 49, 65, 68, 69).

[73] J. Kirscher et al., Eur. Phys. J. **A44** (2010) 239, arXiv: 0903.5538 [nucl-th] (cit. on pp. 20, 65).

[74] D. R. Entem and R. Machleidt, Phys. Rev. **C68** (2003) 041001, arXiv: nucl-th/0304018 [nucl-th] (cit. on p. 22).

[75] L. Huth et al., Phys. Rev. **C96** (2017) 054003, arXiv: 1708.03194 [nucl-th] (cit. on p. 22).

[76] H. Yukawa, Proc. Phys. Math. Soc. Jap. **17** (1935) 48, [Prog. Theor. Phys. Suppl.1,1(1935)] (cit. on p. 22).

[77] J. L. Friar, B. F. Gibson, and G. L. Payne, Phys. Rev. **C30** (1984) 1084 (cit. on p. 22).

[78] P. Reinert, H. Krebs, and E. Epelbaum, Eur. Phys. J. **A54** (2018) 86, arXiv: 1711.08821 [nucl-th] (cit. on p. 22).

[79] R. C. Johnson, Phys. Lett. **114B** (1982) 147 (cit. on p. 24).

[80] T. Luu and M. J. Savage, Phys. Rev. **D83** (2011) 114508, arXiv: 1101.3347 [hep-lat] (cit. on pp. 24, 53).

[81] B.-N. Lu et al., Phys. Rev. **D92** (2015) 014506, arXiv: 1504.01685 [nucl-th] (cit. on p. 24).

[82] E. Epelbaum et al., Eur. Phys. J. **A45** (2010) 335, arXiv: 1003.5697 [nucl-th] (cit. on pp. 24, 50, 52, 53, 55).

[83] B.-N. Lu et al., Phys. Lett. **B760** (2016) 309, arXiv: 1506.05652 [nucl-th] (cit. on pp. 24, 27, 29, 53, 56).

[84] M. Lüscher, Commun. Math. Phys. **104** (1986) 177 (cit. on pp. 24, 42, 43).

[85] S. König, D. Lee, and H.-W. Hammer, Phys. Rev. Lett. **107** (2011) 112001, arXiv: 1103.4468 [hep-lat] (cit. on p. 26).

[86] S. König, D. Lee, and H.-W. Hammer, Annals Phys. **327** (2012) 1450, arXiv: 1109.4577 [hep-lat] (cit. on p. 26).

[87] U.-G. Meißner, G. Ríos, and A. Rusetsky, Phys. Rev. Lett. **114** (2015) 091602, [Erratum: Phys. Rev. Lett.117,no.6,069902(2016)], arXiv: 1412.4969 [hep-lat] (cit. on pp. 26, 62).

[88] H.-W. Hammer, J.-Y. Pang, and A. Rusetsky, JHEP **09** (2017) 109, arXiv: 1706.07700 [hep-lat] (cit. on pp. 26, 62).

[89] H.-W. Hammer, J.-Y. Pang, and A. Rusetsky, JHEP **10** (2017) 115, arXiv: 1707.02176 [hep-lat] (cit. on p. 26).

[90] S. König and D. Lee, Phys. Lett. **B779** (2018) 9, arXiv: 1701.00279 [hep-lat] (cit. on pp. 26, 62).

[91] R. A. Briceño and Z. Davoudi, Phys. Rev. **D87** (2013) 094507, arXiv: 1212.3398 [hep-lat] (cit. on p. 26).

[92] R. A. Briceño, M. T. Hansen, and A. Walker-Loud, Phys. Rev. **D91** (2015) 034501, arXiv: 1406.5965 [hep-lat] (cit. on p. 26).

[93] M. Lüscher, Commun. Math. Phys. **105** (1986) 153 (cit. on pp. 26, 42, 43, 74).

[94] M. Lüscher, Nucl. Phys. **B354** (1991) 531 (cit. on p. 26).

[95] C. Lanczos, J. Res. Natl. Bur. Stand. B **45** (1950) 255 (cit. on p. 30).

[96] W. E. Arnoldi, Quart. Appl. Math. **9** (1951) 17 (cit. on p. 30).

[97] E. Epelbaum et al., Eur. Phys. J. **A41** (2009) 125, arXiv: 0903.1666 [nucl-th] (cit. on p. 31).

[98] D. Lee, Lect. Notes Phys. **936** (2017) 237, arXiv: 1609.00421 [nucl-th] (cit. on p. 31).

[99] R. L. Stratonovich, Soviet Physics Doklady **2** (1957) 416 (cit. on p. 32).

[100] J. Hubbard, Phys. Rev. Lett. **3** (1959) 77 (cit. on p. 32).

[101] J. E. Hirsch, Phys. Rev. **B28** (1983) 4059 (cit. on p. 32).

[102] S. Duane et al., Phys. Lett. **B195** (1987) 216 (cit. on p. 33).

[103] E. Wigner, Phys. Rev. **51** (1937) 106 (cit. on p. 33).

[104] E. Epelbaum et al., Phys. Rev. **C65** (2002) 044001, arXiv: nucl-th/0106007 [nucl-th] (cit. on p. 33).

[105] S. Chandrasekharan and U.-J. Wiese, Phys. Rev. Lett. **83** (1999) 3116, arXiv: cond-mat/9902128 [cond-mat] (cit. on p. 36).

[106] N. Klein et al., Phys. Lett. **B747** (2015) 511, arXiv: 1505.07000 [nucl-th] (cit. on p. 39).

[107] U.-G. Meißner, Nucl. Phys. News. **24** (2014) 11, arXiv: 1505.06997 [nucl-th] (cit. on p. 39).

[108] T. A. Lähde et al., Phys. Lett. **B732** (2014) 110, arXiv: 1311.0477 [nucl-th] (cit. on pp. 39, 49, 50, 64, 66, 69).

[109] D. Lee and R. Thomson, Phys. Rev. **C75** (2007) 064003, arXiv: nucl-th/0701048 [nucl-th] (cit. on p. 40).

[110] B.-N. Lu et al., Phys. Rev. **D90** (2014) 034507, arXiv: 1403.8056 [nucl-th] (cit. on p. 40).

[111] A. Rokash et al., J. Phys. **G41** (2014) 015105, arXiv: 1308.3386 [nucl-th] (cit. on p. 44).

[112] D. R. Phillips, S. R. Beane, and T. D. Cohen, Annals Phys. **263** (1998) 255, arXiv: hep-th/9706070 [hep-th] (cit. on pp. 45, 93).

[113] P. F. Bedaque, H.-W. Hammer, and U. van Kolck, Phys. Rev. Lett. **82** (1999) 463, arXiv: nucl-th/9809025 [nucl-th] (cit. on p. 45).

[114] N. Klein et al., Eur. Phys. J. **A54** (2018) 121, arXiv: 1803.04231 [nucl-th] (cit. on p. 49).

[115] E. Epelbaum et al., Phys. Rev. Lett. **104** (2010) 142501, arXiv: 0912.4195 [nucl-th] (cit. on pp. 49, 53, 57, 59, 61, 66).

[116] J. M. Alarcón et al., Eur. Phys. J. **A53** (2017) 83, arXiv: 1702.05319 [nucl-th] (cit. on pp. 49, 50, 56, 69, 80, 87, 89).

[117] P. Navrátil et al., Phys. Rev. Lett. **99** (2007) 042501, arXiv: nucl-th/0701038 [nucl-th] (cit. on p. 49).

[118] G. Hagen et al., Phys. Rev. Lett. **101** (2008) 092502, arXiv: 0806.3478 [nucl-th] (cit. on p. 49).

[119] T. Otsuka et al., Phys. Rev. Lett. **105** (2010) 032501, arXiv: 0908.2607 [nucl-th] (cit. on p. 49).

[120] J. D. Holt, J. Menendez, and A. Schwenk, Eur. Phys. J. **A49** (2013) 39, arXiv: 1108.2680 [nucl-th] (cit. on p. 49).

[121] S. Binder et al., Phys. Rev. **C87** (2013) 021303, arXiv: 1211.4748 [nucl-th] (cit. on p. 49).

[122] V. Somà et al., Phys. Rev. **C89** (2014) 061301, arXiv: 1312.2068 [nucl-th] (cit. on p. 49).

[123] F. Wienholtz et al., Nature **498** (2013) 346 (cit. on p. 49).

[124] S. Binder et al., Phys. Rev. **C93** (2016) 044002, arXiv: 1505.07218 [nucl-th] (cit. on p. 49).

[125] A. Ekström et al., Phys. Rev. **C91** (2015) 051301, arXiv: 1502.04682 [nucl-th] (cit. on p. 49).

[126] J. E. Lynn et al., Phys. Rev. **C96** (2017) 054007, arXiv: 1706.07668 [nucl-th] (cit. on p. 49).

[127] S. Binder et al., Phys. Rev. **C98** (2018) 014002, arXiv: 1802.08584 [nucl-th] (cit. on p. 49).

[128] D. Lee, Phys. Rev. **A73** (2006) 063204, arXiv: physics/0512085 [physics] (cit. on pp. 49, 67, 69).

[129] S. Elhatisari et al., Phys. Rev. Lett. **119** (2017) 222505, arXiv: 1702.05177 [nucl-th] (cit. on pp. 50, 69).

[130] E. Epelbaum, Eur. Phys. J. **A34** (2007) 197, arXiv: 0710.4250 [nucl-th] (cit. on p. 50).

[131] A. Nogga, *private communication* (cit. on p. 50).

[132] J. E. Drut and A. N. Nicholson, J. Phys. **G40** (2013) 043101, arXiv: 1208.6556 [cond-mat.stat-mech] (cit. on p. 53).

[133] S. Elhatisari et al., Eur. Phys. J. **A52** (2016) 174, arXiv: 1603.02333 [nucl-th] (cit. on pp. 56, 69).

[134] V. G. J. Stoks et al., Phys. Rev. **C49** (1994) 2950, arXiv: nucl-th/9406039 [nucl-th] (cit. on p. 56).

[135] C. Körber and T. Luu, Phys. Rev. **C93** (2016) 054002, arXiv: 1511.06598 [nucl-th] (cit. on p. 62).

[136] A. Nogga, S. K. Bogner, and A. Schwenk, Phys. Rev. **C70** (2004) 061002, arXiv: nucl-th/0405016 [nucl-th] (cit. on p. 65).

[137] N. Klein, D. Lee, and U.-G. Meißner, (2018), arXiv: 1807.04234 [hep-lat] (cit. on p. 69).

[138] N. Li et al., Phys. Rev. **C98** (2018) 044002, arXiv: 1806.07994 [nucl-th] (cit. on p. 69).

[139] E. Epelbaum et al., Phys. Rev. Lett. **112** (2014) 102501, arXiv: 1312.7703 [nucl-th] (cit. on p. 69).

[140] S. Elhatisari et al., Phys. Rev. Lett. **117** (2016) 132501, arXiv: 1602.04539 [nucl-th] (cit. on p. 69).

[141] G. Rupak and D. Lee, Phys. Rev. Lett. **111** (2013) 032502, arXiv: 1302.4158 [nucl-th] (cit. on p. 69).

[142] S. Bour et al., Phys. Rev. **C86** (2012) 034003, arXiv: 1206.1765 [nucl-th] (cit. on p. 69).

[143] S. Elhatisari et al., Phys. Lett. **B768** (2017) 337, arXiv: 1610.09095 [nucl-th] (cit. on p. 69).

[144] A. Bulgac, J. E. Drut, and P. Magierski, Phys. Rev. Lett. **96** (2006) 090404, arXiv: cond-mat/0505374 [cond-mat.stat-mech] (cit. on p. 69).

[145] D. Lee, Phys. Rev. **C78** (2008) 024001, arXiv: 0803.1280 [nucl-th] (cit. on p. 69).

[146] J. Carlson et al., Phys. Rev. **A84** (2011) 061602, arXiv: 1107.5848 [cond-mat.quant-gas] (cit. on p. 69).

[147] M. G. Endres et al., Phys. Rev. **A87** (2013) 023615, arXiv: 1203.3169 [hep-lat] (cit. on p. 69).

[148] S. Bour et al., Phys. Rev. Lett. **115** (2015) 185301, arXiv: 1412.8175 [cond-mat.quant-gas] (cit. on p. 69).

[149] J. Braun, J. E. Drut, and D. Roscher, Phys. Rev. Lett. **114** (2015) 050404, arXiv: 1407.2924 [cond-mat.quant-gas] (cit. on p. 69).

[150] E. R. Anderson and J. E. Drut, Phys. Rev. Lett. **115** (2015) 115301, arXiv: 1505.01525 [cond-mat.quant-gas] (cit. on p. 69).

[151] M. Lüscher and P. Weisz, Commun. Math. Phys. **97** (1985) 59, [Erratum: Commun. Math. Phys.98,433(1985)] (cit. on p. 69).

[152] B. Sheikholeslami and R. Wohlert, Nucl. Phys. **B259** (1985) 572 (cit. on p. 69).

[153] M. Lüscher et al., Nucl. Phys. **B478** (1996) 365, arXiv: hep-lat/9605038 [hep-lat] (cit. on p. 69).

[154] M. Lüscher et al., Nucl. Phys. **B491** (1997) 323, arXiv: hep-lat/9609035 [hep-lat] (cit. on p. 69).

[155] H. Bethe, Z. Phys. **71** (1931) 205 (cit. on p. 70).

[156] N. P. Mehta and J. R. Shepard, Phys. Rev. **A72** (2005) 032728, arXiv: nucl-th/0504049 [nucl-th] (cit. on p. 71).

[157] E. Epelbaum et al., Eur. Phys. J. **A53** (2017) 98, arXiv: 1611.06040 [nucl-th] (cit. on p. 77).

[158] L. Platter, H.-W. Hammer, and U.-G. Meißner, Phys. Rev. **A70** (2004) 052101, arXiv: cond-mat/0404313 [cond-mat] (cit. on p. 78).

[159] L. Platter, H.-W. Hammer, and U.-G. Meißner, Few Body Syst. **35** (2004) 169, arXiv: cond-mat/0405660 [cond-mat.other] (cit. on p. 78).

[160] G. P. Lepage et al., Phys. Rev. **D46** (1992) 4052, arXiv: hep-lat/9205007 [hep-lat] (cit. on p. 78).

[161] C. T. H. Davies et al., Phys. Rev. **D56** (1997) 2755, arXiv: hep-lat/9703010 [hep-lat] (cit. on p. 78).

[162] A. Spitz et al., Phys. Rev. **D60** (1999) 074502, arXiv: hep-lat/9906009 [hep-lat] (cit. on p. 78).

[163] J. M. Alarcón, EPJ Web Conf. **81** (2014) 05002 (cit. on p. 80).

[164] B. Borasoy et al., Eur. Phys. J. **A35** (2008) 343, arXiv: 0712.2990 [nucl-th] (cit. on p. 87).

[165] R. T. Birge, Phys. Rev. **40** (2 1932) 319 (cit. on p. 89).

[166] R. Navarro Pérez, J. E. Amaro, and E. Ruiz Arriola, Phys. Rev. **C89** (2014) 064006, arXiv: 1404.0314 [nucl-th] (cit. on p. 89).

[167] S. R. Beane, T. D. Cohen, and D. R. Phillips, Nucl. Phys. **A632** (1998) 445, arXiv: nucl-th/9709062 [nucl-th] (cit. on p. 93).

Acknowledgements

Finally, I want to acknowledge several people for their support and encouragement over the last years.

First of all my gratitude goes to Professor Dr. Ulf-G. Meißner for the opportunity to do research on nuclear theory in his group. I want to thank him for his advise and support throughout the years, but also for his patience if things sometimes take longer than expected.

Secondly, I want to thank Professor Dr. Dean Lee for many valuable discussions and explanations on nuclear lattice effective field theory, from a physical but also from a technical perspective. He always took seemingly easy questions serious and has always been available at Bonn, at NC state or via Skype and email.

Additionally, I want to give my gratitude to Professor Dr. Tom Luu for being the second referee of my thesis as well as Professor Dr. Reinhard Beck and Professor Dr. Barbara Niethammer who complete the dissertation committee.

I also want to thank my collaborators Dr. Jose Manuel Alarcón, Dr. Timo A. Lähde and Dr. Serdar Elhatisari for many fruitful discussions, helpful comments, further ideas and careful proof-reading work.

For their administrative work and help I want to thank Barbara Kraus and Christa Börsch.

Last but not least, a particular thank goes to my colleagues and former colleagues Franz Niecknig, Johanna Niecknig, Shahin B. Bour, Matthias Frink, Christopher Helmes, Deborah Rönchen, Daniel Severt, Jan Lüdtke, Malwin Niehus and Christopher Körber for conversations on physics and beyond, the nice and supportive atmosphere as well as activities beside the university.